



Universidade do Estado do Rio de Janeiro

Centro de Tecnologia e Ciências

Faculdade de Engenharia

Fernando Rocha Sarquis

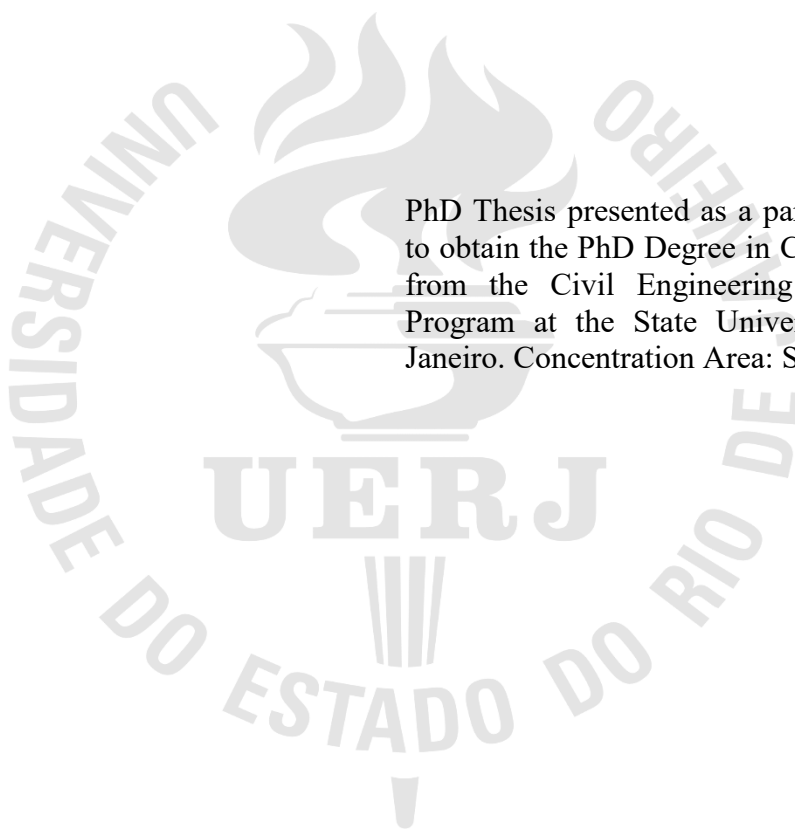
**Numerical assessment of fixed-ended short-to-intermediate stainless
steel starred hot-rolled equal-leg angle sections built-up columns**

Rio de Janeiro

2024

Fernando Rocha Sarquis

Numerical assessment of fixed-ended short-to-intermediate stainless steel starred hot-rolled equal-leg angle sections built-up columns



PhD Thesis presented as a partial requirement to obtain the PhD Degree in Civil Engineering from the Civil Engineering Post Graduate Program at the State University of Rio de Janeiro. Concentration Area: Structures.

Supervisor: Prof. Dr. Luciano Rodrigues Ornelas de Lima

Rio de Janeiro

2024

CATALOGAÇÃO NA FONTE
UERJ / REDE SIRIUS / BIBLIOTECA CTC/B

S246	<p>Sarquis, Fernando Rocha. Numerical assessment of fixed-ended short-to-intermediate stainless steel starred hot-rolled equal-leg angle sections built-up columns / Fernando Rocha Sarquis. – 2024. 168 f.</p> <p>Orientador: Luciano Rodrigues Ornelas de Lima. Tese (Doutorado) – Universidade do Estado do Rio de Janeiro, Faculdade de Engenharia.</p> <p>1. Engenharia civil - Teses. 2. Aço austenítico - Teses. 3. Colunas - Teses. 4. Método dos elementos finitos - Teses. 5. Análise estrutural (Engenharia) - Teses. I. Magalhães, Margareth da Silva. II. Pimenta, André Rocha. III. Universidade do Estado do Rio de Janeiro, Faculdade de Engenharia. IV. Título.</p> <p style="text-align: right;">CDU 624.072.44</p>
------	---

Bibliotecária: Júlia Vieira – CRB7/6022

Autorizo, apenas para fins acadêmicos e científicos, a reprodução total ou parcial desta tese,
desde que citada a fonte.

Assinatura

Data

Fernando Rocha Sarquis

Numerical assessment of fixed-ended short-to-intermediate stainless steel starred hot-rolled equal-leg angle sections built-up columns

PhD Thesis presented as a partial requirement to obtain the PhD Degree in Civil Engineering from the Civil Engineering Post Graduate Program at the State University of Rio de Janeiro. Concentration Area: Structures.

Approved on: 05th October 2024.

Examination board:

Prof. Luciano Rodrigues Ornelas de Lima (Supervisor), DSc
Structural Engineering Department, Faculty of Engineering – UERJ

Prof. André Tenchini da Silva, PhD
Structural Engineering Department, Faculty of Engineering – UERJ

Prof. Rodrigo Bird Burgos, DSc
Structural Engineering Department, Faculty of Engineering – UERJ

Prof. Eduardo de Miranda Batista, DSc
Federal University of Rio de Janeiro, COPPE – UFRJ

Profa. Arlene Maria Cunha Sarmanho, DSc
Federal University of Ouro Preto, PROPEC – UFOP

Rio de Janeiro

2024

DEDICATION

This work is dedicated to my family, especially my parents, Ana Cristina Rocha and Flavio Sarquis.

ACKNOWLEDMENTS

My deepest gratitude to my parents, Ana Cristina Rocha and Flavio Sarquis, for their tireless support and motivation throughout my academic journey. The love and values they have imparted and their commitment to my education have been fundamental to my personal and professional development. Their emotional and financial support has been pivotal, providing the foundation of confidence necessary to achieve my goals. Thank you very much.

My grandfather, Bento Marinheiro, my godmother, Ceci Borges, and my brother, Flavio Junior, thank you all for your love, guidance, and support, which have been instrumental in my development. This achievement would not have been possible without each of you.

My supervisor, Prof. Dr Luciano Rodrigues Ornelas de Lima, who has been an invaluable source of guidance, inspiration, and support throughout this challenging and inspiring journey. His teachings have significantly expanded my knowledge and shaped my approach to research and problem-solving. Our conversations have provided profound insights and motivation, while his friendship has offered the encouragement and confidence I needed to persevere through difficult times. I am deeply grateful for his mentorship, inspiration, and friendship.

My late master's supervisor, Prof. Dr Pedro Colmar Gonçalves da Silva Vellasco, whose guidance and wisdom have left an enduring impact on my academic journey. His teachings continue to inspire me.

To the master's student, Ada Kayser, for trusting and confiding in my ideas throughout her academic journey, from her undergraduate research and bachelor's degree to her master's work. Your dedication and hard work have been truly inspiring.

My friends Tatiane Capellani and Augusto Cezar, for their invaluable conversations, advice, and partnership from our undergraduate years through to the completion of my doctoral studies.

To the other many friends I made during this journey, I will not quote names to avoid being unfair. However, thank you all for making this journey lighter and more enjoyable.

The financial support from the Brazilian government is via CAPES during the doctoral degree program.

Two things awe me most, the starry sky above me and the moral law within me.

Immanuel Kant

RESUMO

SARQUIS, Fernando Rocha. *Investigação numérica de colunas engastadas compostas por seções cantoneiras de abas iguais laminadas a quente com seção cruciforme de aços inoxidáveis*. 2024. 168 f. Tese (Doutorado em Engenharia Civil) – Faculdade de Engenharia, Universidade do Estado do Rio de Janeiro, Rio de Janeiro, 2024.

Os aços inoxidáveis austenítico e duplex são escolhidos para uma vasta gama de construções devido às suas notáveis características como, por exemplo, elevada resistência à corrosão, durabilidade, resistência e apelo estético. Contudo, as diretrizes de projeto atuais do Eurocódigo 3: Parte 1.4, específico para estruturas de aços inoxidáveis, frequentemente baseiam-se em analogias com o comportamento do aço carbono, o que pode não ser adequado, devido às características específicas do material, como o seu comportamento não-linear. Adicionalmente, seções cantoneira de abas iguais são comumente empregadas em aplicações estruturais, particularmente para colunas de comprimentos curtos a intermediários, que exibem comportamentos estruturais distintos. A geometria de sua seção transversal, caracterizada pelo encontro das linhas média (baixa rigidez torcional) e centroide não alinhado com o centro de cisalhamento, afeta o comportamento pós-flambagem das colunas, devido à interação entre deslocamentos ao redor dos eixos de maior e menor inércia, influenciando diretamente a resistência final do elemento. Neste contexto, a utilização de uma seção cruciforme, formada pela união de duas seções cantoneira de abas iguais conectadas pelo canto – alinhando o centroide e o centro de cisalhamento, emerge como uma solução eficiente para mitigar o deslocamento nos eixos de maior e menor inércia durante o comportamento pós-flambagem, resultando em uma estrutura mais estável. Com o objetivo de abordar as lacunas relacionadas ao uso de aços inoxidáveis e à aplicação de colunas com seção cruciforme, este estudo realiza uma investigação numérica sobre colunas com apoios fixos constituídas de aços inoxidáveis austenítico e duplex com seções cruciforme (tanto soldadas quanto parafusadas) de comprimentos curtos a intermediários, portanto suscetíveis à flambagem torsional. Um modelo de elementos finitos sólido foi desenvolvido e validado com resultados experimentais para examinar: (i) o comportamento de flambagem elástica das colunas, (ii) os caminhos de equilíbrio no comportamento elástico pós-flambagem, (iii) a sensibilidade à imperfeição geométrica inicial, (iv) a influência das propriedades mecânicas dos aços inoxidáveis austenítico e duplex, e (v) obter a carga máxima das colunas. Uma análise paramétrica foi realizada, considerando seções transversais compactas típicas de cantoneiras de abas iguais (ou seja, $b/t < 20$) e selecionando comprimentos de colunas – com base no comportamento de flambagem elástica – propensas à falha por flambagem torsional. Por fim, (vi) a resistência última numérica obtida é usada para avaliar se as disposições de cálculo do Eurocódigo 3: Parte 1.4, especificamente a curva de flambagem “b”, prevê com precisão a carga última. As discrepâncias encontradas entre a carga última numérica e a resistência à flambagem por torção prevista pelo Eurocódigo indicaram um conservadorismo desnecessário. Consequentemente, propõe-se duas modificações ao código europeu, incluindo uma reclassificação da seção e uma modificação da curva de flambagem “b” usada atualmente para o dimensionamento desses elementos estruturais.

Palavras-chave: Aço inoxidável austenítico; Aço inoxidável duplex; Cantoneiras de abas iguais em compressão; Eurocode 3; Colunas biengastada; Elementos finitos; Investigação numérica; Seção estrelada; Flambagem torsional.

ABSTRACT

SARQUIS, Fernando Rocha. *Numerical assessment of fixed-ended short-to-intermediate stainless steel starred hot-rolled equal-leg angle sections built-up columns*. 2024. 168 p. Thesis (DSc. in Civil Engineering) – Faculty of Engineering, State University of Rio de Janeiro, Rio de Janeiro, 2024.

Austenitic and duplex stainless steels are chosen for many constructions due to their remarkable corrosion resistance, durability, strength, and aesthetic appeal. However, the current design guidelines of Eurocode 3: Part 1.4, specific to stainless steel structures, often rely on analogies with the behaviour of carbon steel, which may not be suitable due to the specific characteristics of the material, such as its nonlinear behaviour. Additionally, equal-leg angle sections are commonly employed in structural applications, particularly for short-to-intermediate columns exhibiting distinct structural behaviours. The cross-section geometry is characterized by the mid-lines intersecting at a common point (low torsional stiffness), and the centroid is not aligned with the shear centre, which affects these columns' post-buckling behaviour due to the interaction between displacements around the major and minor inertia axes, directly influencing the element's ultimate strength. In this context, the use of a starred section, formed by joining two equal-leg angle sections at the corner – aligning the centroid and shear centre, emerges as an efficient solution to mitigate displacement in the major and minor axes during post-buckling behaviour, resulting in a more stable structure. In order to address the gaps related to the use of stainless steel and the application of columns with starred sections, this study conducts a numerical investigation on short-to-intermediate length columns with fixed supports made of austenitic and duplex stainless steel starred sections (both welded and bolted), thus susceptible to torsional buckling. A solid finite element model was developed and validated against experimental results to assess (i) the columns' elastic buckling behaviour, (ii) elastic post-buckling behaviour equilibrium paths, (iii) initial geometrical imperfection sensitivity, (iv) influence of material mechanical properties of austenitic and duplex stainless steel, and (v) the columns' ultimate failure load. A parametric analysis was performed through typical compact equal-leg angle cross-sections (i.e., $b/t < 20$) and selecting column lengths susceptible to torsional buckling failure based on the elastic buckling behaviour. Finally, the numerical ultimate strengths obtained are used to assess whether the design provisions of Eurocode 3: Part 1.4 – column buckling curve “b” – can accurately forecast the ultimate load. Discrepancies between the numerical failure load and the predicted Eurocode buckling ultimate torsional load revealed unduly conservatism. Consequently, two proposed modifications to the European code are suggested, involving a cross-section classification and change of the current buckling curve “b” actually used to assess the design of these structural elements.

Keywords: Austenitic stainless steel; Duplex stainless steel; Equal-leg angles under compression; Eurocode 3; Fixed-ended columns; Finite element model; Numerical investigation; Starred sections; Torsional buckling.

FIGURES

Figure 1: a) Stress versus stress curve comparison for stainless steel and carbon steel ranging from 0 to 0.75% strain, and b) definition of the stainless steel's 0.2% proof strength.	24
Figure 2: a) Telecommunication angle steel tower [6] and b) structural reinforcement high-voltage tower [7].	25
Figure 3: Dual equal-leg angle starred built-up section with a) bolted plate and b) welds.	26
Figure 4: a) Cruciform geometry, b) column torsional buckling, and c) mid-span cross-section torsional rotation.	31
Figure 5: a) Equal-leg angle section geometry, b) column with equal-leg angle cross-section prone to failure by flexural-torsional buckling, and c) mid-span cross-section buckling deformation.	33
Figure 6: Short equal-leg angle columns' buckling mode according to Timoshenko and Gere [10].	34
Figure 7: Equal-leg angle columns comparison with a rectangular plate in end compression with one longitudinally supported edge and the other free.	36
Figure 8: Common cross-section deformation profiles and warping functions a) cross-section with five nodes, b) rigid-body modes ($k = 1 - 4$), and c) cross-section distortion mode ($k = 5$) [20].	39
Figure 9: Prismatic member a) geometry/axes displacements and b) cross-section discretisation [27].	41
Figure 10: Lipped channel a) cross-section discretisation and b) first eight deformation modes in-plane shapes (rigid-body, distortional and local-plate).	44
Figure 11: Lipped channel column buckling mode as a linear combination of GBT cross-section deformation modes 2 and 4 (known as flexural-torsional buckling).	46
Figure 12: Rectangular plate in end compression with a) longitudinal edge simply supported and other free (S-F) and b) longitudinal edge built-in and other free (B-F) [15]. ...	50
Figure 13: Elastically restrained outstanding flange and two GBT deformation modes included in the analysis [30];	51
Figure 14: Variation of buckling coefficient k_{cr} with the aspect ratio ϕ and α [30].	51
Figure 15: Finite element model elastic buckling analysis of simply supported (S) or built-in (B) longitudinally rectangular plate with other free.	53

Figure 16: Equal-leg angle cross-section GBT a) discretisation and b) in-plane deformation mode shapes (2-7) [30].	54
Figure 17: Equal-leg angle column buckling behaviour a) P_b vs. L curves, b) modal participations diagram, and c) critical buckling mode shapes of columns with different lengths [30].	56
Figure 18: (a) P_{cr} vs. L curves, (b) GBT modal participation diagrams for F, PC, and PS columns, and (c) in-plane shapes of 2 buckling modes and the first 5 GBT deformation modes for PC columns [31].	60
Figure 19: a) F_1 - F_{10} columns mid-span equilibrium paths P/P_{cr} vs. β and b) F_3 and F_9 columns cross-section deformed configuration evolutions [31].	63
Figure 20: Evolution of the F_3 and F_9 column mid-span normal stress distribution concerning three load levels [31].	63
Figure 21: F_3 , F_6 , and F_9 columns a) P/P_{cr} vs. d_m/t and b) P/P_{cr} vs. d_m/t equilibrium paths [31].	65
Figure 22: F_3 , F_6 , and F_9 columns a) P/P_{cr} vs. d_M/t and a) P/P_{cr} vs. d_m/t longitudinal profiles [31].	65
Figure 23: F_3 column elastic-plastic post-buckling behaviour a) P/P_{cr} vs. β equilibrium paths, for $\sigma_y/\sigma_{cr} \approx 1.3, 2.5, 5.0$ and b) plastic strain diagrams and failure mechanism, for $\sigma_y/\sigma_{cr} \approx 2.5$ [34].	67
Figure 24: F_9 column elastic-plastic post-buckling behaviour a) P/P_{cr} vs. β equilibrium paths, for $\sigma_y/\sigma_{cr} \approx 1.3, 2.5, 5.0$ and b) plastic strain diagrams and failure mechanism, for $\sigma_y/\sigma_{cr} \approx 2.5$ [34].	67
Figure 25: f_{cr} vs. L curves for F, PC, and PS columns with $b = 90$ mm and $b/t = 40$ or $b/t = 20$ [35].	68
Figure 26: Fixed-ended columns' elastic equilibrium paths P/P_{cr} vs. β and P/P_{cr} vs. d_m/t with $L/L_T \approx 0.25, 0.50, 0.75, 1.00$.	69
Figure 27: a) Equal-leg angle cross-section, b) flexural-torsional buckling, c) welded starred torsional buckling and d) bolted starred torsional buckling.	70
Figure 28: Pinned and fixed column a) P_{cr} vs. L curves, b) GBT modal participation diagrams, and c) 3 pinned column buckling modes and 8 GBT deformations mode shapes [36].	71
Figure 29: a) Fixed P/P_{cr} vs. β column equilibrium paths and L7 column mid-span cross-section deformed configurations and b) P/P_{cr} vs. β equilibrium paths for F plate, FR angle and L7 column [36].	72

Figure 30: F_3, F_5, F_9 column a) $P/P_{cr,Av}$ vs. β and b) $P/P_{cr,Av}$ vs. ε paths ($5 \sigma_y/\sigma_{cr}$), and c) deformed configuration and plastic strain evolution ($L5 + \sigma_y/\sigma_{cr} \approx 2.6$) [36].	73
Figure 31: Eurocode 3 categorizes cross-sections into four distinct behavioural classes.	79
Figure 32: The concept of the Effective Width Method for cross-section class 4 – transforming non-uniform stress distribution into a uniform one.	81
Figure 33: Eurocode 3: Part 1.1 a) multiple column buckling curves [5] and b) curve “b”.	83
Figure 34: Column’s layout procedure to create a welded starred cross-section [50].	86
Figure 35: Equal-leg angle bolted starred column, b) section cut from the equal-leg angle profile to produce the connection plates, and c) designed plate dimensions for experimental bolted connection.	86
Figure 36: Bolted starred columns experimental prototypes [50].	87
Figure 37: An overview of the experimental layout with a) displacement transducer position and b) mid-span cross-section ($L/2$) instrumentation.	88
Figure 38: Welded starred column (WSC) equilibrium path – load versus axial shortening curves (P vs Δ_y) – and five deformed shapes throughout test A.	90
Figure 39: a) Welded starred column (WSC-A) equilibrium path – mid-span ($L/2$) load versus transverse displacements (P vs Δ_x and P vs Δ_z) – and b) the cross-section torsional rotation.	91
Figure 40: Bolted starred column (BSC) equilibrium path – load versus axial shortening curves (P vs Δ_y) – and four deformed shapes throughout test A.	93
Figure 41: a) Bolted starred column (BSC-A) equilibrium path – mid-span ($L/2$) load versus transverse displacements (P vs Δ_x and P vs Δ_z) – and b) the cross-section torsional rotation.	93
Figure 42: Bolted starred columns experimental results column’s failure mode through two viewpoints.	94
Figure 43: a) Experimental assembly procedure used in Botelho <i>et al.</i> [50] and b) finite element model assembly procedure with continuous fillet weld.	98
Figure 44: Starred columns’ elastic buckling behaviour featuring two equal-leg angle sections 2L63.50×4.76 and varying length $L = 700, 1400$ and 2800 comparison between welding a) spaced at intervals of $L/3$, and b) applied continuously along the entire length of the column.	98
Figure 45: a) Welded starred column geometry with initial geometrical imperfection and b) mid-span ($L/2$) cross-section torsional rotation.	100

Figure 46: P_{cr} vs. L curves for columns with fixed ends created through two equal-leg angle b/t ratios of 13.34 and 18.64, respectively, and b) columns' mid-span ($L/2$) torsional buckling deformation.	102
Figure 47: Torsional buckling elastic buckling shape for columns with lengths from $0.30L_{TFS}$ up to $0.95L_{TFS}$ considering a) $b/t = 13$ and b) $b/t = 18$	102
Figure 48: Fixed-ended welded starred columns equilibrium paths P/P_{cr} vs. β created through equal-leg angle cross-section with a) $b/t = 13.34$ and b) $b/t = 18.64$	105
Figure 49: P/P_{cr} vs β equilibrium path for fixed-ended welded starred columns with length equal to $0.95L_{TFS}$ showing three columns deformed configuration as the cross-section torsional rotation increases from 0.1 to 0.5 rad featuring a) $b/t = 13.34$ and b) $b/t = 18.68$	105
Figure 50: a) Tensile coupon tests obtained by Botelho <i>et al.</i> [50] and b) average stress-strain curve adopted to validate the finite element model.	108
Figure 51: Finite element model validation comparing the column's equilibrium path concerning a) load versus axial shortening curves (P vs Δ_y) and b) load versus transverse displacements (P vs Δ_x and P vs Δ_z).	108
Figure 52: Finite element model comparing torsional failure mode.	108
Figure 53: Load vs axial shortening curves (P vs Δ_y) concerning each initial geometrical imperfection amplitude for fixed-ended welded starred columns with a length equal to a) 700 mm, b) 1600 mm, and c) 2400 mm.	111
Figure 54: a) Austenitic and b) Duplex stainless steel stress-strain curves adopted in the finite element model.	114
Figure 55: a) Adopted 3-point residual stress distribution on the welded starred cross-section and b) applied residual stress in the finite element model in ANSYS [29].	117
Figure 56: Equilibrium paths ($P_{u,FE}$ vs. Δ_v) and deformed configuration development of austenitic stainless steel welded starred column without and with residual stresses.	119
Figure 57: Equilibrium paths ($P_{u,FE}$ vs. Δ_v) and deformed configuration development of duplex stainless steel welded starred column without and with residual stresses.	120
Figure 58: a) Ultimate strength ratio ($P_{u,RS}/P_{u,WRS}$) and b) reduction factor (χ_{RS}) concerning non-dimensional L/L_{TFS} ratio.	120
Figure 59: Numerical results compared to buckling curves “a0” and “b” for torsional buckling failure mode.	123

Figure 60: Finite element model bolt connection overview, including connection plate dimensions and bolt geometry.	125
Figure 61: Three pairs of contact interactions: 1) the bolt head and the flange of the equal-leg angle column; 2) the plate and the equal-leg angle columns; 3) the bolt nut and the plate.	126
Figure 62: Numerical von Mises stresses at the bolt connection due to the bolt preload application.	127
Figure 63: a) Bolted starred equal-leg angle columns boundary conditions and b) mid-span ($L/2$) cross-section torsional rotation – initial geometrical imperfection.	129
Figure 64: a) P_{cr} vs. L curves for columns with fixed ends created through two equal-leg angle b/t ratios of 13.34 and 18.64, respectively, and b) columns' mid-span ($L/2$) torsional buckling deformation.	133
Figure 65: Torsional buckling failure mode shape for columns with lengths from $0.30L_{TFS}$ up to $0.95L_{TFS}$	134
Figure 66: Fixed-ended bolted starred columns equilibrium paths P/P_{cr} vs. β created through equal-leg angle cross-section with a) $b/t = 13.34$ and b) $b/t = 18.64$	135
Figure 67: P/P_{cr} vs β equilibrium path for fixed-ended bolted starred columns with length equal to $0.95L_{TFS}$ and three columns deformed configuration as the cross-section torsional rotation increases from 0.1 to 0.5 rad.	136
Figure 68: Finite element model validation comparing the column's equilibrium path: a) load versus axial shortening curves (P vs Δ_y) and b) load versus transverse displacements (P vs Δ_x and P vs Δ_z).	137
Figure 69: Finite element model validation comparing the column's failure mode through two viewpoints.	138
Figure 70: Load vs axial shortening curves (P vs Δ_y) concerning each initial geometrical imperfection amplitude for fixed-ended bolted starred columns with a length equal to a) 700 mm, b) 1400 mm, and c) 2100 mm.	140
Figure 71: Numerical results compared to buckling curves “ a_0 ”, “ a ”, and “ b ” for stainless steel columns torsional buckling failure mode.	143
Figure 72: Continuous normalised ultimate strength pattern as non-dimensional torsional slenderness increases considering the austenitic and duplex stainless steel for a) S4, b) S9, and S12 cross-sections.	144

Figure 73: Welded starred columns comparison of numerical results with Eurocode 3: Part 1.4 [4] a) column buckling curve “b”, b) column buckling curve “a ₀ ”, and) column buckling curve “a ₀ ” using A_g	147
Figure 74: Bolted starred columns comparison of numerical results with Eurocode 3: Part 1.4 [4] a) column buckling curve “b” using $A = A_g$ or A_{eff} and) column buckling curve “b” using A_g	150
Figure 75: Bolted starred columns comparison of numerical results with Eurocode 3: Part 1.4 [4] a) column buckling curve “a” using A_g and) column buckling curve “a ₀ ” using A_g	152
Figure 76: Austenitic stainless steel welded starred columns experimental/numerical (r_e) x theoretical (r_t) results plot a) EC3 approach curve “b”, b) modified EC3 approach curve “a ₀ ” and c) modified EC3 approach curve “a ₀ ” using A_g	153
Figure 77: Duplex stainless steel welded starred columns experimental/numerical (r_e) x theoretical (r_t) results plot a) EC3 approach curve “b”, b) modified EC3 approach curve “a ₀ ” and c) modified EC3 approach curve “a ₀ ” using A_g	153
Figure 78: Austenitic stainless steel bolted starred columns experimental/numerical (r_e) x theoretical (r_t) results plot a) EC3 approach curve “b”, b) modified EC3 approach curve “b” using A_g and c) modified EC3 approach curve “a” using A_g	154
Figure 79: Duplex stainless steel bolted starred columns experimental/numerical (r_e) x theoretical (r_t) results plot a) EC3 approach curve “b”, b) modified EC3 approach curve “b” using A_g and c) modified EC3 approach curve “a” using A_g	154

TABLES

Table 1: Cross-section properties in Conventional Notations and GBT [20].	40
Table 2: Comparison of longitudinal free edge sinusoidal half-wave plate deformation patterns between S-F and B-F varying the aspect ratio ϕ .	53
Table 3: Angle section maximum width-to-thickness ratio for compression parts [4].	80
Table 4: Effective width of outstand compression elements [51].	81
Table 5: WSC and BSC experimental ultimate load and failure mode.	89
Table 6: Initial geometrical imperfection sensitivity study for fixed-ended stainless steel welded starred columns ranging from $0.24L/L_{TFS}$ to $0.83L/L_{TFS}$.	110
Table 7: Summary of essential material properties used in the finite element model.	114
Table 8: Equal-leg angle cross-section selection to create a welded starred section.	115
Table 9: Comparison between welded starred and cruciform geometrical sections' properties.	116
Table 10: Cross-section dimensions, ratio b/t , geometrical section's properties, and chosen lengths for numerical parametric investigation.	123
Table 11: Initial geometrical imperfection sensitivity study for fixed-ended stainless steel bolted starred columns ranging from $0.30L/L_{TFS}$ to $0.92L/L_{TFS}$.	140
Table 12: Typical compact cross-section dimensions and lengths selection for parametric analysis.	141
Table 13: Classification of cross-section, gross area (A_g) and effective area (A_{eff}).	147
Table 14: Welded starred columns strengths comparison summary ($P_{u,FE}/P_{u,EC3}$).	148
Table 15: Eurocode 3: Part 1-4 [4] – cross-section classification, gross area (A_g) and effective area (A_{eff}).	148
Table 16: Bolted starred columns strengths comparison summary ($P_{u,FE}/P_{u,EC3}$).	152
Table 17: Reliability analysis results assessed according to EN 1990 [61] for welded starred columns.	157
Table 18: Reliability analysis results assessed according to EN 1990 [61] for bolted starred columns.	157

ABBREVIATION AND ACRONYMS

BSC	Bolted Starred Columns
CoV	Coefficient of Variation
DSM	Direct Strength Method
EC3	Eurocode 3
GBT	Generalized Beam Theory
IST	Instituto Técnico Superior
LEC	Civil Engineering Laboratory
LVDT	Linear Variable Differential Transducer
UERJ	State University of Rio de Janeiro
WSC	Welded Starred Columns

NOTATIONS

A	Cross-section area
A_g	Gross cross-section area
A_{eff}	Effective cross-section area
b	Equal-leg angle width
b_{eff}	Effective equal-leg angle width
C	Cross-section centroid
d_m	Major-axis displacement – minor-axis flexural buckling
d_M	Minor-axis displacement – major-axis flexural buckling
d_b	Connection bolt diameter
d_p	Bolted connection plates' hole diameter
E	Young's Modulus
F	Fixed-ended columns
$f_{u,b}$	Connection bolt ultimate tensile strength
G	Shear modulus
h_p	Connection plate's height
i_0	Polar gyration radius relative to the shear centre
I_0	Polar moment inertia
I_u	Second moment of area about the u-axis
I_v	Second moment of area about the v-axis
I_T	Welded torsional constant
I_x	Second moment of area about the x-axis
I_y	Second moment of area about the y-axis
I_w	Warping constant
I_{ws}	Secondary warping constant
J	Literature torsional constant
k	Plate buckling coefficient
L	Column length
L_{TFS}	Fixed-ended welded starred column transition length
m	Number of longitudinally sinusoidal half-wave
$P_{cr,FT}$	Elastic critical flexural-torsional buckling load

$P_{cr,L}$	Elastic critical plate buckling load
$P_{cr,T}$	Elastic critical torsional buckling load
$P_{cr,u}$	Elastic critical major-axis flexural buckling load
$P_{cr,v}$	Elastic critical minor-axis flexural buckling load
$P_{u,EC3}$	Eurocode 3 design torsional buckling resistance
$P_{u,FE}$	Numerical ultimate load
$P_{u,RS}$	Numerical ultimate load with residual stress
$P_{u,WRS}$	Numerical ultimate load without residual stress
t	Equal-leg angle thickness
t_p	Bolted connection plates' thickness
u	Equal-leg angle cross-section first principal axis
u_0	Equal-leg angle cross-section distance between the shear centre and the centroid
v	Equal-leg angle cross-section second principal axis
w_p	Bolted connection plates' width
α	Eurocode 3 imperfection factor
β	Column mid-span cross-section torsional rotation
β_0	Initial geometrical imperfection column mid-span cross-section torsional rotation
β_{RS}	Welded starred section residual stress maximum and minimum value
γ_{MI}	Eurocode 3 partial safety factor
Δ	Displacement
ε	Eurocode 3 non-dimensional parameter relating to material's mechanical properties
ε_u	Stainless steel failure strain
λ_0	Eurocode 3 curve non-dimensional slenderness limit
λ_p	Eurocode 3 plate's non-dimensional slenderness limit
λ_T	Non-dimensional torsional slenderness
ν	Poisson's coefficient
ρ	Eurocode 3 plate's reduction factor
$\sigma_{0,2\%}$	Stainless steel 0.2% proof strength
σ_y	Carbon steel yield strength
σ_u	Stainless steel's ultimate strength
χ	Eurocode 3 column reduction factor
χ_{RS}	Residual stress reduction factor

ψ

Eurocode 3 parameter, which correlates the plate's internal normal stress ratio

CONTENTS

INTRODUCTION	23
1 LITERATURE REVIEW	29
1.1 Introduction	29
1.2 Torsional and flexural-torsional buckling.....	30
1.2.1 Introduction	30
1.2.2 Torsional buckling.....	30
1.2.3 Flexural-torsional buckling	32
1.3 Structural behaviour of short-to-intermediate equal-leg angle columns	33
1.3.1 Local/torsional mixed deformations mode	34
1.3.2 Brief overview of Generalised Beam Theory (GBT) principles	37
1.3.3 Rectangular plates with loaded edges simply supported elastic stability	47
1.3.4 Equal-leg angle columns elastic buckling behaviour	53
1.3.5 Fixed-ended equal-leg angle column's elastic post-buckling behaviour	61
1.3.6 Fixed-ended equal-leg angle columns elastic-plastic post-buckling behaviour and strength	66
1.3.7 Equal-leg angle columns with hot-rolled steel equal-leg angle sections.....	67
1.4 Structural behaviour of short-to-intermediate cruciform columns.....	69
1.4.1 Introduction	69
1.4.2 Elastic buckling behaviour	70
1.4.3 Fixed-ended elastic post-buckling behaviour	71
1.4.4 Fixed-ended elastic-plastic post-buckling behaviour and strength.....	72
1.5 Fixed-ended equal-leg angle and starred columns' ultimate strength and design	73
1.5.1 Carbon steel material	73
1.5.2 Stainless steel material.....	74
2 STAINLESS STEEL COLUMNS' DESIGN – EUROCODE 3: PART 1.4 (EC3).....	78
2.1 Introduction	78
2.2 Cross-section classification and resistance	78
2.3 Columns buckling design curves	82
3 STAINLESS STEEL FIXED-ENDED STARRED COLUMNS EXPERIMENTAL RESULTS.....	84
3.1 Introduction	84

3.2 Welded and bolted starred columns' assembly procedure.....	84
3.3 Experimental setup and instrumentation.....	87
3.4 Experimental results	88
3.4.1 Welded starred columns	89
3.4.2 Bolted starred columns	91
3.4.3 Conclusions	94
4 WELDED STARRED COLUMNS ELASTIC BUCKLING BEHAVIOUR AND FINITE ELEMENT MODEL VALIDATION	96
4.1 Introduction	96
4.2 Solid finite element model development	97
4.3 Column buckling behaviour	100
4.4 Column elastic post-buckling behaviour	103
4.5 Numerical model validation – stainless steel material behaviour	106
4.6 Initial geometrical imperfection sensitivity	108
5 WELDED STARRED COLUMNS NUMERICAL PARAMETRIC INVESTIGATION	112
5.1 Introduction	112
5.2 Austenitic and duplex stainless steel material behaviour	112
5.3 Equal-leg angle cross-section selection	114
5.4 Welded starred section properties	115
5.5 Residual stresses effects.....	117
5.6 Numerical results.....	121
6 BOLTED STARRED COLUMNS FINITE ELEMENT MODEL DEVELOPMENT	124
6.1 Element type and bolted starred column geometry	124
6.2 Contact modelling at the bolt connection	125
6.3 Bolt preload	126
6.4 Boundary conditions	128
6.5 Initial geometrical imperfection and residual stress	128
6.6 Analysis methodology and solution.....	129
7 BOLTED STARRED COLUMNS ELASTIC BUCKLING BEHAVIOUR, FINITE ELEMENT MODEL VALIDATION, AND PARAMETRIC INVESTIGATION	131
7.1 Introduction	131
7.2 Column buckling behaviour	131

7.3 Column elastic post-buckling behaviour	134
7.4 Numerical model validation – stainless steel material behaviour	136
7.5 Initial geometrical imperfection sensitivity	138
7.6 Numerical parametric investigation	140
8 EUROCODE 3: PART 1.4 COLUMNS’ DESIGN ASSESSMENT	145
8.1 Introduction	145
8.2 Fixed-ended short-to-intermediate stainless steel welded starred columns	145
8.3 Fixed-ended short-to-intermediate stainless steel bolted starred columns	148
8.4 Reliability analysis	152
9 FINAL CONSIDERATIONS	158
REFERENCES	160
APPENDIX A.....	166

INTRODUCTION

Generalities

Stainless steel offers several advantages in civil engineering structural applications, as elucidated by Badoo [1]. According to the Design Manual for Structural Stainless Steel [2], two prevalent types of stainless steel are commonly used in structural applications: (i) austenitic grade 1.4301 (widely known as 304) and (ii) duplex grade 1.4462. Austenitic stainless steels are typically chosen for structural members that demand good strength, corrosion resistance, and excellent elongation before fracture. Duplex stainless steels are suitable in situations where high strength and corrosion resistance are required. In recent years, the increasing need for durable and enduring structures with minimal maintenance has increased the demand for stainless steel in the construction sector. The ease of fabrication into several structural components, appearance, and corrosion qualities of stainless steel make it a preferred material for functional and visually appealing components in modern structural projects.

However, this material presents particular stress-strain curve behaviour. Unlike carbon steel, which typically displays linear elastic behaviour with a clearly defined yield stress, σ_y , stainless steel exhibits a non-linear elastic response without a well-defined yielding plateau strength, conventionally identified as a 0.2% proof strength ($\sigma_{0.2\%}$), as illustrated in Figure 1. Afshan and Gardner [3] highlighted a critical aspect concerning the European code design guidelines for structural members made of austenitic and duplex stainless steel – Eurocode 3: Part 1.4 [4]. Its formulation relies on limit state design provisions derived from the behaviour of carbon steel established in Eurocode 3: Part 1.1 [5]. This methodology reveals insufficient information concerning the stainless steel members' experimental and numerical structural response data.

Additionally, in structural engineering, selecting cross-section shapes for columns (i.e., axial compressive loads) is a critical decision which significantly dictates the overall structural response and efficiency of the constructions. This decision is achieved by in-depth knowledge concerning the columns' mechanical behaviour of different cross-sections, i.e., (i) elastic buckling, (ii) elastic and elastic-plastic post-buckling behaviour, and (iii) ultimate strength, to obtain a safe and proper columns buckling design curve equations for these structural members.

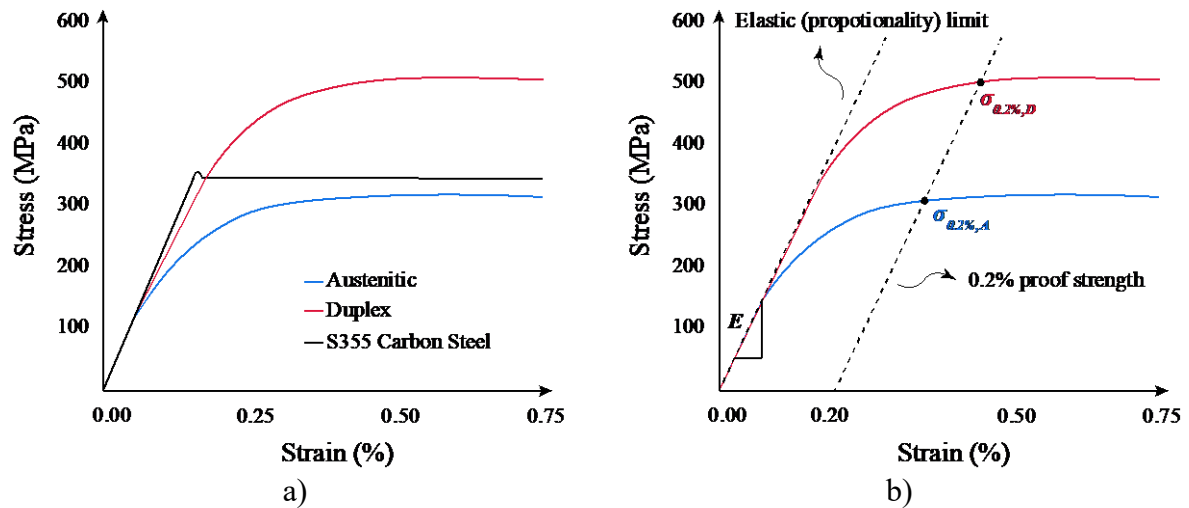


Figure 1: a) Stress versus strain curve comparison for stainless steel and carbon steel ranging from 0 to 0.75% strain, and b) definition of the stainless steel's 0.2% proof strength.

Equal angle sections, also known as L-shaped, are widely employed in various structural applications due to their geometry simplicity, cost-effectiveness, and ease of connection. As crucial supports, they contribute significantly to the strength and stability of buildings, bridges, towers, and various other structures. A notable application of these sections is in high-voltage transmission or telecommunication towers, as shown in Figure 2(a). Particularly, these equal-leg angle columns are designed with short to intermediate lengths to accommodate the essential connections within the structure.

Nevertheless, the inherent geometrical properties of this section (monosymmetric open section) cause low torsional stiffness and the non-coincidence of the centroid and shear centre, predisposing the short-to-intermediate equal-leg angle columns' to failure by flexural-torsional buckling. This phenomenon involves (i) bending about the first principal axis (major-axis flexural buckling) and (ii) cross-section torsional rotation (torsional buckling). It is well-known that the major-axis bending participation influences the equal-leg angle columns' elastic and elastic-plastic post-buckling behaviour and, consequently, directly impacts the load-bearing capacity of these structural members.

As the need for power and telecommunications services grows, existing transmission towers must increasingly accommodate additional loads that surpass their initial design capacities. In response, a prevalent retrofitting strategy in civil engineering involves adding L-shaped profiles, using two equal-leg angles to form a built-up "starred" cross-section, which serves as a reinforcement for the lattice structures of these towers, as shown in Figure 2(b) highlighted in red.

This reinforcement can be constructed by connecting a pair of equal-leg angles using bolted plates or welding at sections' corners, as depicted in Figure 3. A notable characteristic of this geometrical configuration assembly is that the centroid and shear centre are now coincident, influencing the overall structural behaviour. As a result of this geometry, columns with these types of starred sections are expected to be free from major-axis flexural buckling corner displacement. However, due to the inherent low torsional stiffness, the short-to-intermediate columns remain vulnerable to pure torsional buckling failure modes.

It is within this context of ensuring fixed-ended starred columns' integrity that it becomes crucial to emphasize that columns susceptible to failure by flexural-torsional and torsional buckling are assessed under European standard codes (i.e., for carbon [5] and stainless steel [4]) using the same buckling design curve, identified as curve “*b*”, to predict their ultimate strength. This methodology underscores the existing experimental and numerical data gap necessary to distinguish these starred columns' resistance, which presents distinct post-buckling behaviour compared to a single equal-leg column. Therefore, the mechanical behaviour of these starred columns requires a different design approach to ensure a rational and adequate/accurate load-bearing capacity.

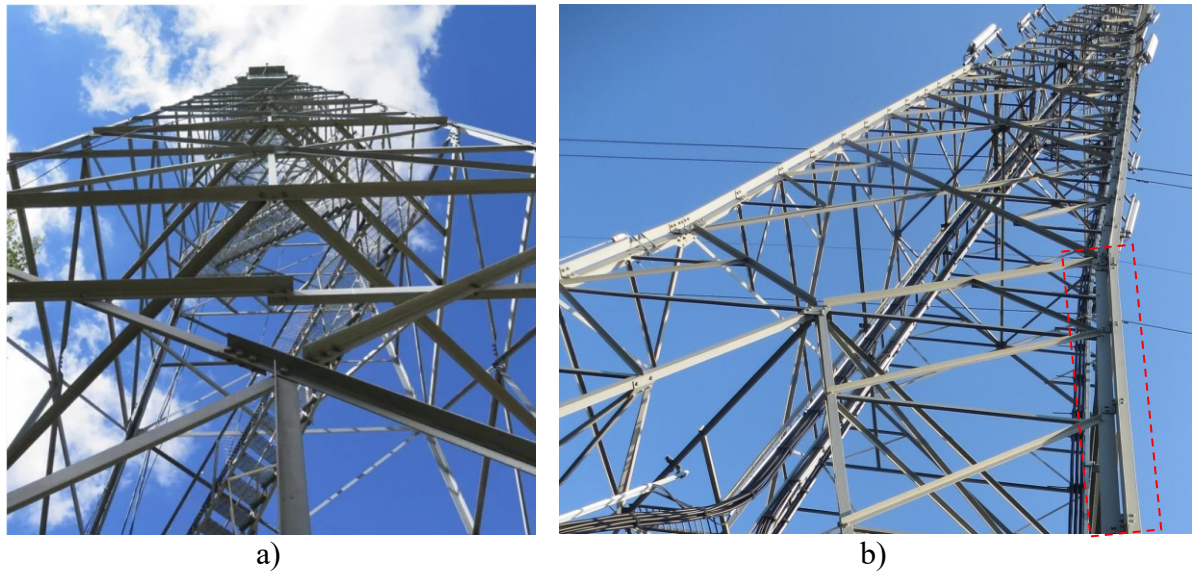


Figure 2: a) Telecommunication angle steel tower [6] and b) structural reinforcement high-voltage tower [7].

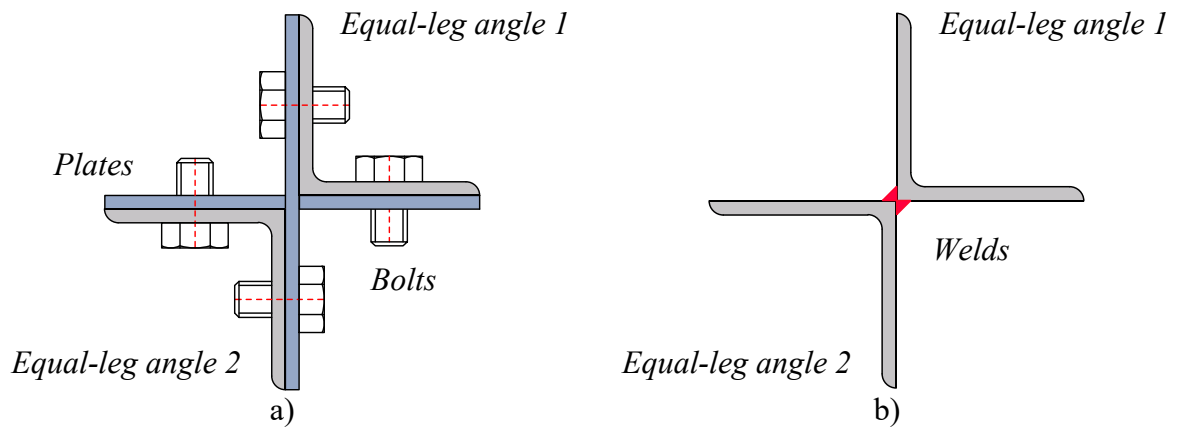


Figure 3: Dual equal-leg angle starred built-up section with a) bolted plate and b) welds.

Objectives

The main objectives of this thesis are to assess the (i) elastic buckling and (ii) elastic post-buckling behaviour of fixed-ended short-to-intermediate starred built-up columns (including bolted plate and welds) to gain insight into the mechanical behaviour of these structural members, focusing exclusively on geometrical nonlinearity. Subsequently, austenitic and duplex stainless steel materials behaviour are introduced into the analysis, aiming (iii) to validate the finite element model against experimental results documented in the existing literature. With this validation, it is possible (iv) to conduct a parametric analysis covering a wider range of equal-leg angle cross-sections and short-to-intermediate columns' lengths that fail due to torsional buckling, i.e., verify the influence of the stainless steel material's nonlinearity on these columns' strength. Finally, (v) the obtained numerical ultimate strengths are used to assess the accuracy of Eurocode 3: Part 1.4 column buckling curve “b” in predicting the ultimate load capacity.

Outline of the thesis

This doctoral thesis is structured into an introduction followed by seven chapters. The introductory section offers insights into the stainless steel material employed in this study, along

with an exploration of the structural uses of equal-leg angle sections and built-up sections composed of two equal-leg angle sections.

Chapter one is dedicated to the literature review, initially discussing the reasons why many studies have misinterpreted local and torsional deformations in short-to-intermediate equal-leg angle columns. It elucidates the distinctions in post-buckling behaviour between columns with equal-leg angles and cruciform sections and summarizes pivotal studies on the structural aspects of these stainless steel columns.

Chapter two delves into the European normative framework (Eurocode 3: Part 1.4) and describes its design methodology for stainless steel structural members. This methodology traditionally relies on the behavioural insights gained from carbon steel structures.

Chapter three compiles significant experimental data from the literature on short-to-intermediate length stainless steel fixed-ended columns, both welded and bolted cross-sections, highlighting their failure modes, displacements, equilibrium paths, and ultimate strengths.

Chapter four details the finite element modelling approach used in this study, discussing the chosen finite element, meshing techniques, geometry, boundary conditions, and the inclusion of initial geometrical imperfection in the numerical models. This chapter further explores the welded starred columns' buckling and elastic post-buckling behaviours, validation against experimental data, and sensitivity to initial geometrical imperfections.

Chapter five presents a parametric analysis aiming to extend the results previously achieved experimentally. It takes into account austenitic and duplex stainless steel materials, equal-leg angle compact sections, and column lengths that are prone to failure by torsional buckling.

Chapter six provides a detailed description of the finite element model development for bolted starred columns, emphasising the key parameters and assumptions made during the numerical analysis. This section covers the assumptions of the developed finite element model, including column geometry, element types, mesh size, boundary conditions, contact modelling, bolt preload, the implementation of initial geometrical imperfections, and the solution technique employed.

Chapter 7 presents the elastic buckling behaviour of bolted starred columns, followed by elastic post-buckling behaviour. It includes the validation of the numerical model, a sensitivity study on geometrical imperfections, and a comprehensive parametric analysis.

Chapter 8 exposes the current design procedures outlined by Eurocode 3 for their excessive conservatism. In response, it proposes two adjustments consistent with Eurocode 3's methodology to refine the design process.

Chapter 9 summarizes the principal conclusions obtained from this research and outlines a schedule for future work. It mainly focuses on extending the analysis to columns with bolted sections to ensure a comprehensive understanding of their structural behaviour.

1 LITERATURE REVIEW

1.1 Introduction

This section presents a comprehensive literature review on the structural behaviour of short-to-intermediate fixed-ended equal-leg angle and cruciform columns. It focuses on the columns' elastic buckling and post-buckling behaviour, elastic-plastic behaviour, and ultimate strength. Thus, an initial investigation into the atypical short-to-intermediate equal-leg angle columns' elastic buckling behaviour is necessary, highlighting the challenge of distinguishing between local and torsional deformations over the years.

However, applying Generalized Beam Theory (GBT) analysis has uncovered significant new insights into these columns' elastic mechanical buckling behaviour, enhancing understanding of their natural mechanical behaviour. Due to these two cross-section geometries, it is demonstrated that columns with equal-leg angles and cruciform profiles of short to intermediate lengths are respectively susceptible to failure by flexural-torsional buckling and pure torsional buckling without the occurrence of local buckling. Based on these results, it is possible to highlight the significant differences between these two phenomena (flexural-torsional and torsional) post-buckling behaviour, which are critical to the columns' stability and ultimate strength.

It is essential to underscore that the analysis extends to the structural behaviour of cruciform columns to draw parallels to built-up double equal-leg angle starred sections. This evolution of understanding from basic column types to more complex configurations, including columns with starred cross-sections, combines the benefits of equal-leg angle (a standard steel profile) and cruciform sections (known for stable post-buckling behaviour).

Therefore, this comprehensive review aims (i) to elucidate the short-to-intermediate fixed-ended equal-leg angle and cruciform columns' buckling behaviours and (ii) provide a solid foundation for understanding and improving the structural behaviour of fixed-ended short-to-intermediate starred columns by integrating these insights.

1.2 Torsional and flexural-torsional buckling

1.2.1 Introduction

Cross-sections composed of thin plates with mid-lines intersecting at a single point (e.g., equal-leg angles and cruciform sections) exhibit no primary warping resistance ($I_w = 0$). This characteristic inherently leads to a significantly low torsional stiffness. Furthermore, the alignment of the centroid and the shear centre in these cross-sections plays a crucial role in influencing the stability of the columns. As a result, (i) columns with cruciform sections are distinctly vulnerable to buckling phenomena associated with pure torsion (torsional buckling). In contrast, (ii) columns with equal-leg angle sections are prone to failure through a combination of major-axis flexural buckling and torsion (flexural-torsional buckling).

1.2.2 Torsional buckling

Pioneering studies carried out by Wagner [8], followed by reviews from Timoshenko [9], Timoshenko and Gere [10], and the detailed investigation by Gaylord and Gaylord [11], significantly contributed to understanding the torsional buckling theory. It is known that if the cross-section geometry consists of thin elements intersecting at a common point and if the axis of rotation (z) is assumed to pass through the shear centre (S), then the primary warping constant is zero ($I_w = 0$).

Figure 4(a) depicts a cruciform section with four identical legs, each defined by a width b and thickness t , which presents the centroid coincident with the shear centre due to the double symmetry (x and y axes). This characteristic naturally means a very low torsional stiffness, making these sections particularly susceptible to torsional buckling, i.e., buckling that involves the cross-section torsion rotation. Thus, if the structural member is submitted to concentrically axial compression (columns), torsional buckling may occur – depending on the length (L) – under a smaller load than the minor-axis flexural buckling.

Figure 4(b) shows cruciform columns subject to failure by torsional buckling under compression. It is essential to highlight two phenomenon's mechanical behaviour

characteristics: (i) each leg behaves identically, showing rigid-body rotation (β) about the shear centre z -axis, and (ii) the column's axis (z) remaining straight, i.e., there are no (major or minor axes) flexural displacements, as depicted in Figure 4(c). Consequently, the columns' elastic critical torsional buckling load ($P_{cr,T}$) – well-established in the literature – can be expressed by Eq. (1).

$$P_{cr,T} = \frac{1}{i_0^2} \left(GJ + \frac{\pi^2 EI_w}{L_{eff}^2} \right) \quad (1)$$

$$i_0^2 = \frac{I_x + I_y}{A} \quad (2)$$

Where i_0^2 is the polar radius of gyration relative to the shear centre, I_x and I_y are the principal second moment of area, A is the gross cross-section area, G is the shear modulus, J is the torsion constant, E is the Young's Modulus, I_w is the primary warping constant, L_{eff} is the effective length for torsion failure mode, GJ is the St. Venant torsional stiffness, and EI_w is the warping torsion stiffness.

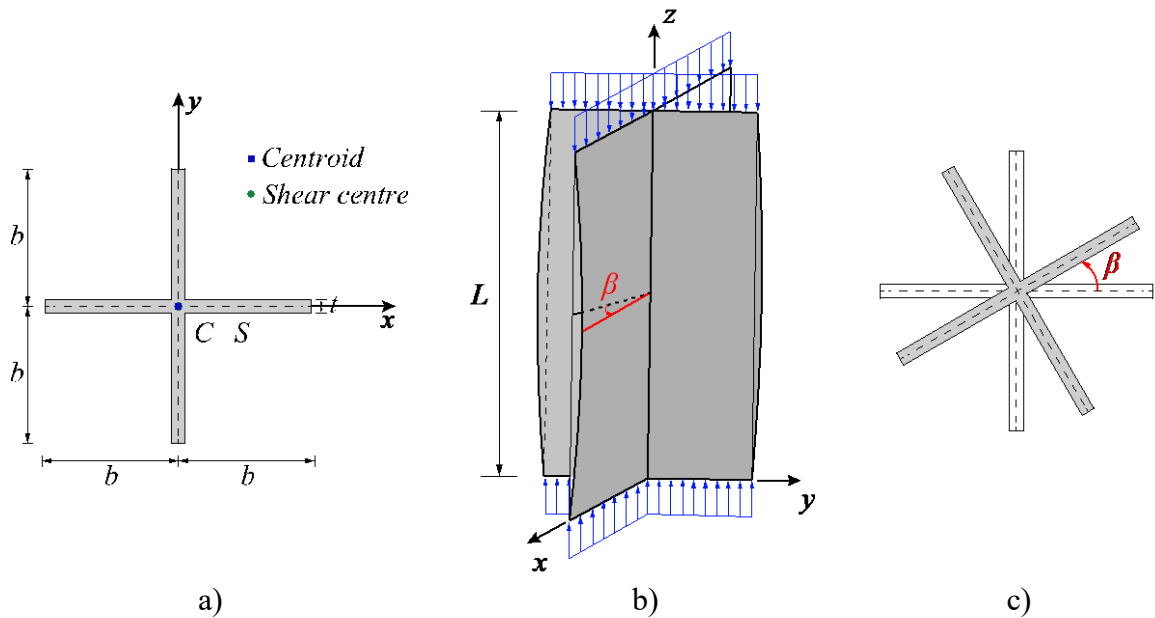


Figure 4: a) Cruciform geometry, b) column torsional buckling, and c) mid-span cross-section torsional rotation.

1.2.3 Flexural-torsional buckling

Despite the simplicity, equal-leg angle sections exhibit two essential geometrical characteristics: monosymmetric open section, i.e., the centroid does not coincide with the shear centre, and their wall mid-lines intersect at a single point. Figure 5(a) depicts the equal-leg angle section geometry, showing the leg width (b) and thickness (t), the centroid (C), and the shear centre (S). Also, it depicts the section's principal axes, which are rotated by 45° relative to the geometrical axes (x and y), thus defining the major and minor axes (u and v), respectively.

As aforementioned, columns with monosymmetric open sections are marked by low torsional stiffness because the primary warping constant is null ($I_w = 0$). This characteristic, combined with the misalignment between the centroid and the shear centre, results in a unique mechanical behaviour in terms of elastic stability analysis. The particular geometry and cross-section properties provoke a structural response encompassing both (i) flexural bending about the major-axis and (ii) torsional movements around the shear centre.

This susceptibility arises from how columns with monosymmetric sections buckle under axial compression. The process begins with rotation about the shear centre due to the low torsional stiffness, referred to as the z_I -axis, which occurs along an axis parallel to the longitudinal z -axis. This cross-section torsional rotation movement inherently couples with bending along one of the column's principal planes, identified as u - z and v - z . Notably, the v - z principal plane does not align with the shear centre, so the bending around the major-axis (u) becomes evident.

Figure 5(b) illustrates an equal-leg angle column that is susceptible to flexural-torsional buckling, showcasing the two significant mechanical behaviour characteristics: (i) the cross-section undergoes a rigid-body rotation around the longitudinal shear centre z_I -axis, and (ii) the z_I -axis does not remain straight, showing bending displacements about the major-axis, (major-axis flexural buckling).

Additionally, Figure 5(c) illustrates these two types of rigid-body motions at the column's mid-span, where d_M means the corner's displacements due to the major-axis flexural buckling, and β represents the cross-section's shear centre torsional rotation, providing a clear visualisation of the column's behaviour. Furthermore, the equation for calculating the columns' elastic critical flexural-torsional buckling ($P_{cr,FT}$) is outlined in Eq. (3):

$$P_{cr,FT} = \frac{P_{cr,u}}{2\eta} \left[1 + \frac{P_{cr,T}}{P_{cr,u}} - \sqrt{\left(1 - \frac{P_{cr,T}}{P_{cr,u}} \right)^2 + 4 \left(\frac{u_0}{i_0} \right)^2 \frac{P_{cr,T}}{P_{cr,u}}} \right] \quad (3)$$

$$P_{cr,u} = \frac{\pi^2 EI_u}{L_{eff}^2} \quad (4)$$

$$\eta = 1 - \left(\frac{u_0}{i_0} \right)^2 \quad (5)$$

where $P_{cr,u}$ is the elastic critical major-axis flexural buckling load, I_u is the major-axis second moment of area, u_0 is the shear centre coordinates with respect to the centroid of gross cross-section, and η is a dimensionless parameter.

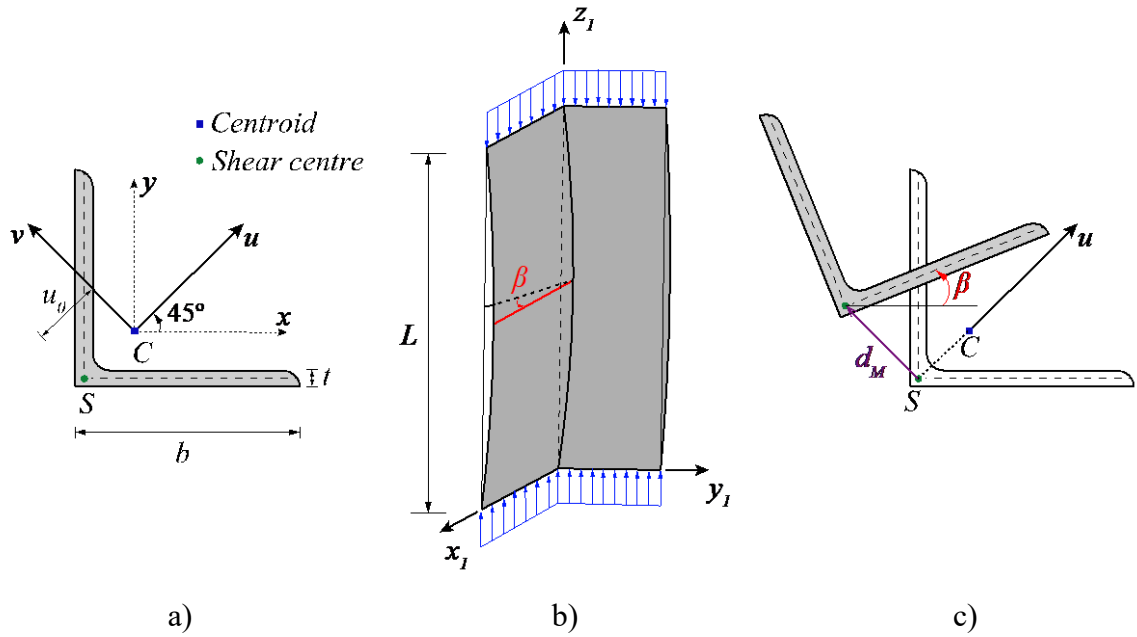


Figure 5: a) Equal-leg angle section geometry, b) column with equal-leg angle cross-section prone to failure by flexural-torsional buckling, and c) mid-span cross-section buckling deformation.

1.3 Structural behaviour of short-to-intermediate equal-leg angle columns

1.3.1 Local/torsional mixed deformations mode

In 1963, Timoshenko and Gere [10] highlighted the peculiarities of equal-leg angle sections. The authors showed that when the section's leg is subjected to uniformly distributed compression in short-to-intermediate lengths, the local buckling mode of the legs displays a local deformed configuration akin to global pure torsional buckling, as depicted in Figure 6. Considering that the mechanical deformation response varies between local and global (torsional) buckling modes, this discrepancy significantly impacts these columns' ultimate strength.

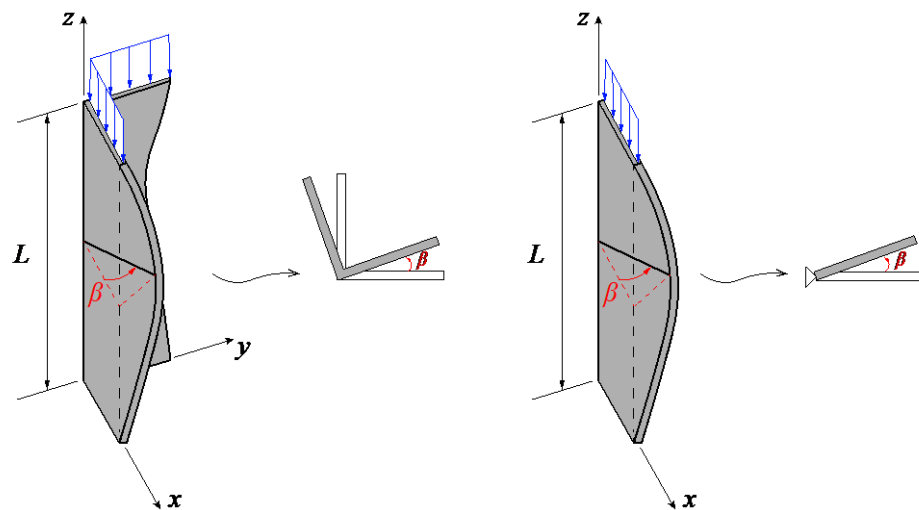


Figure 6: Short equal-leg angle columns' buckling mode according to Timoshenko and Gere [10].

For this reason, investigations into the local and torsional elastic critical buckling behaviour – often described as a virtually identical phenomenon – were carried out in equal-leg angle columns due to the difficulty distinguishing between these two deformations [12]-[14]. In 2005, Rasmussen [12] demonstrated the coincidence between local and torsional elastic critical buckling load grounded in the theory that monosymmetric cross-sections, in which the mid-lines intersect at a common point, exhibiting a null primary warping constant ($I_w = 0$). Consequently, the elastic critical torsional buckling load – Eq. (1) – is simplified to Eq. (6).

$$P_{cr,T} = \frac{GJ}{i_0^2} \quad (6)$$

In Eq. (6), all the terms can be expressed solely in terms of the equal-leg angle cross-section geometry (leg width b and thickness t) and the elastic steel material's properties (Young's Modulus and Poisson's ratio), as shown in Eq. (7) and Eq. (8), respectively.

$$G = \frac{E}{2(1+\nu)} \quad J = \frac{2}{3}bt^3 \quad i_0 = \frac{b^2}{3} \quad (7)$$

$$P_{cr,T} = \frac{E}{(1+\nu)} \frac{t^3}{b} \quad (8)$$

The author also showed the well-established concept of elastic critical plate buckling stress ($\sigma_{cr,L}$), which is derived from the elastic critical plate buckling load ($P_{cr,L}$), as shown in Eq. (9). Additionally, this equation can further be adapted to incorporate the equal-leg angle cross-sections' geometry (b and t), with $A = 2bt$, leading to the derivation of Eq. (10).

$$\sigma_{cr,L} = k \frac{\pi^2 E}{12(1-\nu^2)} \left(\frac{t}{b}\right)^2 \rightarrow P_{cr,L} = Ak \frac{\pi^2 E}{12(1-\nu^2)} \left(\frac{t}{b}\right)^2 \quad (9)$$

$$P_{cr,L} = k \frac{\pi^2}{6(1-\nu)} \frac{E}{(1+\nu)} \frac{t^3}{b} \quad (10)$$

In Eq. (10), the only different term is related to the plates' buckling coefficient k . However, according to Rasmussen [12], each leg of an equal-leg angle behaves like a rectangular plate in end compression with one longitudinally supported edge and the other free, as depicted in the frontal perspective presented in Figure 7. Following this, the plates' buckling coefficient k can be obtained according to Bulson [15] and expressed in Eq. (13) for typical column lengths (rectangular plates' elastic stability is assessed in detail in Section 1.3.3).

$$k = \frac{6(1-\nu)}{\pi^2} \quad (11)$$

Cross-section geometry

Equal-leg angle column

Rectangular plate

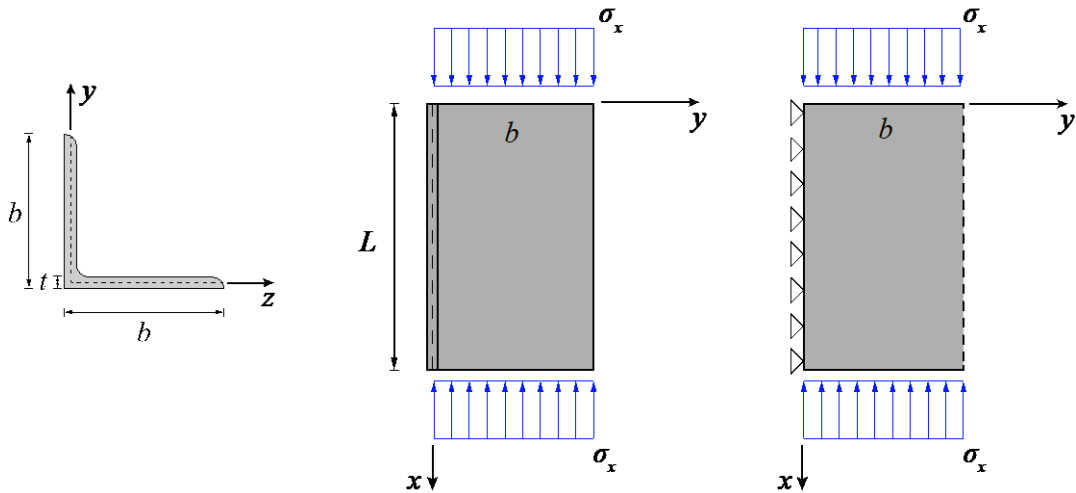


Figure 7: Equal-leg angle columns comparison with a rectangular plate in end compression with one longitudinally simply supported edge and the other free.

Therefore, substituting Eq. (11) into Eq. (10) reveals that an identical formula is arrived at for both the elastic critical torsional and local buckling loads, as demonstrated in Eq. (12). From this observation, the author concluded that the elastic critical loads are equivalent and coincident for conventional lengths of equal-leg angle columns.

$$P_{cr,T} = P_{cr,L} = \frac{E}{(1+\nu)} \frac{t^3}{b} \quad (12)$$

However, this approach does not provide any details on the deformations and mechanical behaviour of the structural elements. Moreover, to understand the distinction behaviours of local and torsional deformations in equal-leg angles columns, it is crucial to underscore two fundamental concepts that hold relevance to understanding the structural behaviour of short-to-intermediate equal-leg angle columns for this work, i.e., (i) the concepts of the Generalized Beam Theory (GBT) and (ii) the study carried out by Bulson in 1970 [15] focusing on flat rectangular plates.

1.3.2 Brief overview of Generalised Beam Theory (GBT) principles

This section briefly reviews the Generalised Beam Theory (GBT) principles considering a cold-formed steel member composed of an open thin-walled unbranched cross-section that aims to distinguish between the mechanical behaviour of local and torsional deformations in equal-leg angle columns. The Generalised Beam Theory (GBT), pioneered by Schardt [16]-[17], represents an extension of Vlasov's [18] classical bar theory by incorporating folded-plate concepts. It serves as a sophisticated framework for analysing the structural behaviour of cold-formed steel thin-walled members.

Davies, Leach and colleagues ([19]-[24]) have extensively employed GBT to investigate the buckling behaviour of cold-formed steel thin-walled members. Their research has significantly validated GBT as a viable and often preferred alternative to numerical finite element or finite strip analyses. GBT integrates both cross-section and global (member) modes of deformation, facilitating the execution of geometrically linear analyses (first-order GBT) or linear stability analyses (second-order GBT).

This second approach offers a unified methodology for obtaining precise and insightful solutions to diverse structural problems. Indeed, the distinctive decomposition of the member's buckling mode shape into a linear combination of cross-section deformation modes is accountable for the clarity of the GBT solutions. In this context, the GBT buckling analysis approach involves two primary tasks: (i) conducting a cross-section analysis, i.e., aimed at obtaining the so-called "cross-section deformation modes", and (ii) performing a member linear stability analysis to assess the participation of each deformation mode in the longitudinal axis.

1.3.2.1 Elementary warping functions and cross-section modal properties introduction

According to Davies and Leach [19], the theory's core involves "warping elementary functions"¹, where each cross-section deformation mode k is associated with axial strain

¹ Initially, it is essential to highlight that the term "warping" is frequently encountered in the context of Generalised Beam Theory (GBT). Its use may be confused as it is often linked with non-uniform torsion. However, in this context, "warping" encompasses axial deformation and is not solely related to the torsion deformation mode.

distribution ${}^k\tilde{t}$. In this context, the first mode exhibits a uniform distribution of axial strain across the cross-section, represented by the warping function ${}^1\tilde{t}$ for all points s of the cross-section. The second and third modes correspond to bending, featuring warping functions that depict linear strain distributions about the two principal axes. Lastly, the fourth mode, i.e., torsion about the shear centre, retains its traditional definition of warping, wherein the warping function represents the sectorial coordinate reflecting the distribution of axial strain induced by the bi-moment. These four modes are often called the “rigid-body” modes because they do not entail cross-section distortion, i.e., the cross-section geometry remains unchanged, and the elements remain straight.

Figure 8(a) presents a cross-section with five natural nodes to illustrate these concepts. Figure 8(b) illustrates the four rigid-body modes, and Figure 8(c) the cross-section distortion mode 5. According to GBT principles, each of these five nodes can independently “warp”, with the warping functions exhibiting linearity between the nodes. Consequently, each warping function possesses five degrees of freedom, resulting in the section having five orthogonal deformation modes and their respective associated warping functions. Additional distortion modes can be incorporated into the analysis by introducing intermediate nodes between the natural ones. Therefore, each mode k is defined by (i) a warping function, (ii) a specific pattern of cross-section displacements, and (iii) cross-section properties denoted as kC , kD and kB .

Additionally, the authors [19] provided an equivalence between the conventional theory of structural mechanics and GBT section properties to establish an evident mechanical meaning behaviour concerning the deformation modes – presented in Table 1. In this table, A is the cross-section area, I_{xx} is the second moment of area about the first principal axis, I_{yy} is the second moment of area about the second principal axis, I_w is the warping constant, and J is the Saint Venant torsional constant.

This comparison shows that C represents the stiffness associated with direct stress in the respective mode, D indicates the stiffness related to shear stresses resulting from torsion, and B signifies the stiffness of transverse bending stress. For instance, focusing solely on mode 3 (minor-axis bending), it becomes evident that its resistance is directly linked to the second moment of area about the second principal axis (I_{yy}). Now, shifting focus to mode 4, it becomes clear that it pertains to the warping constant (I_w) and the St. Venant torsional constant (J).

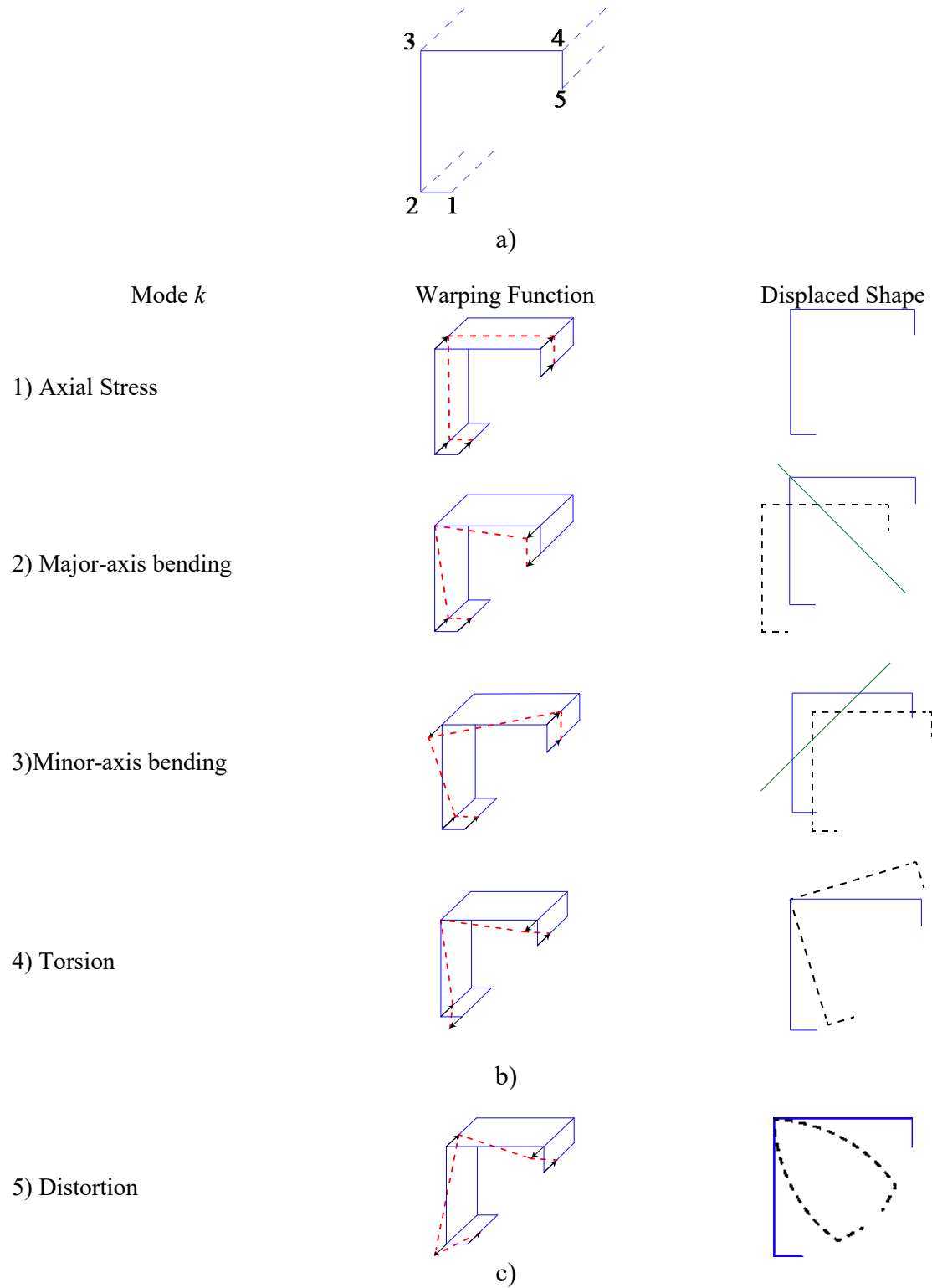


Figure 8: Common cross-section deformation profiles and warping functions a) cross-section with five nodes, b) rigid-body modes ($k = 1 - 4$), and c) cross-section distortion mode ($k = 5$) [20].

Table 1: Cross-section properties in Conventional Notations and GBT [20].

<i>Deformation mode</i>	<i>Conventional theory</i>			<i>Generalised beam theory</i>		
1	A			1C		
2	I_{xx}			2C		
3	I_{yy}			3C		
4	I_w	J		4C	4D	
k	$?$	$?$	$?$	kC	kD	kB

1.3.2.2 Cross-section analysis – displacement field

The derivation presented pertains to a prismatic member featuring an arbitrary unbranched² open thin-walled cross-section comprised of rectangular plate elements with uniform thickness (t). It is essential to highlight that fundamental assumptions used in GBT cross-section deformation modes are extensively elucidated by Silvestre and Camotim [25]-[26] and briefly presented in this section – aiming to present the most crucial theory concepts to understand the study of short-to-intermediate equal-leg angle columns.

In order to initiate this derivation, it is imperative to establish initial definitions. A right-handed orthogonal local coordinate system is introduced, denoted as x, s, z . In this arrangement, the x -coordinate aligns parallel to the member axis. At the same time, the s -coordinate runs along the cross-sectional midline, and the z -coordinate is perpendicular to the cross-sectional mid-plane. This local coordinate system defines the local displacements u, v , and w , as illustrated in Figure 9(a).

Gonçalves *et al.* [28] describe that the cross-section is divided into multiple plate elements determined by nodes, i.e., cross-section discretisation. Within this analysis, two node types are distinguished: natural nodes and intermediate nodes. Natural nodes are positioned at the intersection of two plate elements or free edges. On the other hand, intermediate nodes are situated within a plate element, positioned between two plate's natural nodes. This arrangement is illustrated in Figure 9(b).

² This definition applies in cases where a maximum of two walls exclusively share each cross-section node.

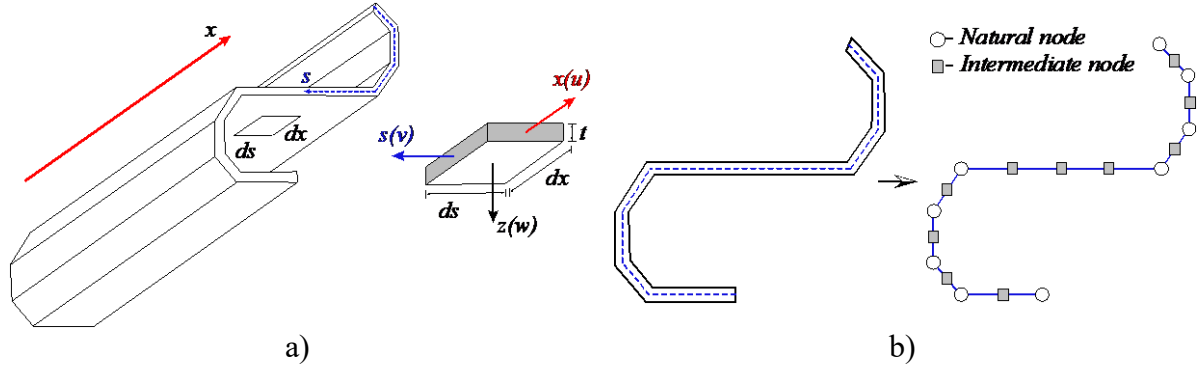


Figure 9: Prismatic member a) geometry/axes displacements and b) cross-section discretisation [27].

The mid-line displacement field representation is adopted following Vlasov's classical thin-walled beam theory [18], expressing each local displacement component as a product of two single-variable functions – $u(x, s)$, $v(x, s)$, and $w(x, s)$ – a technique commonly employed in rectangular plate analysis. In other words, one variable depends on the longitudinal axis coordinate (x), while the other is dependent on the cross-section mid-line abscissa (s), as presented in Eq. (13).

$$u(x, s) = u(s) \cdot \psi_{k,x}(x) \quad v(x, s) = v(s) \cdot \psi_k(x) \quad w(x, s) = w(s) \cdot \psi_k(x) \quad (13)$$

Where (i) the comma subscripts denote partial derivatives, (ii) the mid-line “displacements profiles” are represented by $u(s)$, $v(s)$ and $w(s)$ (iii) $\psi(x)$ is a dimensionless “displacement amplitude function” along the member length ($0 \leq x \leq L$).

According to Silvestre and Camotim [25], GBT's most distinctive feature lies in expressing the transverse mid-line displacement profiles $v(s)$ and $w(s)$ in terms of the longitudinal displacement $u(s)$, which are geometrical. This approach enables a comprehensive definition of the member's behaviour, encompassing displacements, strains, stresses, and internal forces, based solely on the knowledge of the longitudinal displacement $u(x, s)$. Additionally, the authors assume that $u(s)$ varies linearly within each plate element, implying that a linear function is employed across the entire cross-section. This assumption signifies that $u(s)$ can be fully determined by its nodal values based on the cross-section discretisation. In other words, the process involves sequentially introducing (i) elementary

warping functions at natural nodes and (ii) elementary flexural functions at intermediate nodes. Further elucidation on this procedural aspect is available in the referenced literature [25]-[32].

Thus, the displacement $u(s)$ along the coordinate s in a member can be expressed as shown in Eq. (14). It is calculated as the product of the displacement $u(s_k)$ at node k multiplied by the interpolation function $u_k(s)$, which is a linear function of s that has a unit value at node k and zero value at all other nodes. This equation means that the displacement along the element is calculated by multiplying the displacement at the node by the value of the interpolation function associated with the node.

$$u(s) = u(s_k)u_k(s) \quad (14)$$

This process effectively entails “discretising” the deformed configuration of the cross-section into a set of modes equivalent to the number of nodes. The nodal warping values serve as the degrees of freedom, i.e., the number of degrees of freedom depends on whether intermediate nodes are included. If intermediate nodes are excluded, the number of degrees of freedom equals the number of natural nodes. However, if intermediate nodes are included, the number of degrees of freedom equals the total number of nodes plus two additional degrees of freedom associated with the two boundary nodes. Therefore, the displacement field for a member formed by k nodes is expressed as shown in Eq. (15).

$$u(x, s) = u_k(s) \cdot \phi_{k,x}(x) \quad v(x, s) = v_k(s) \cdot \phi_k(x) \quad w(x, s) = w_k(s) \cdot \phi_k(x) \quad (15)$$

Where the $u_k(s)$, $v_k(s)$ and $w_k(s)$ are the shape functions to approximate the cross-section displacement field, i.e., cross-section deformation modes, and $\phi_k(x)$ quantifies the magnitude of these deformation modes along the length of the member – the common displacement amplitude function and defined in Eq. (16). Finally, the member’s behaviour is determined by summing over the cross-section deformation modes k . This approach allows users to select which modes to consider and assess the influence of different deformation modes on the overall behaviour of the member.

$$\phi_k(x) = u(s_k) \cdot \psi_k(x) \quad (16)$$

1.3.2.3 Assumptions and kinematic relations

The formulation of the GBT is based on two simplifying approximations rooted in thin plate theory. Firstly, Kirchhoff's hypothesis is valid for each plate forming the member. Consequently, fibres normal to the mid-plane are expected to remain straight, inextensional, and perpendicular to the deformed mid-plane throughout deformation, as presented in Eq. (17). Secondly, only longitudinal extensions are considered in terms of membrane strains, while shear strains and transverse extensions are neglected – as shown in Eq. (18).

$$\gamma_{xz} = \gamma_{sz} = \varepsilon_{zz} = 0 \quad (17)$$

$$\varepsilon_{xx}^M \neq 0 \text{ and } \gamma_{xs}^M = \varepsilon_{ss}^M = 0 \quad (18)$$

These simplifications lead to the kinematic strain-displacement relations for the mid-plane displacement, as expressed in Eq. (19), for membrane strains (M) and strains corresponding to the bending of the plate element (F). Finally, incorporating Eq. (15) into the kinematic relations results in Eq. (20), where membrane and flexural axial extensions are grouped.

$$\varepsilon_{xx}^M = u_{,x}; \quad \varepsilon_{xx}^F = -z \cdot w_{,xx}; \quad \varepsilon_{ss}^F = -z \cdot w_{,ss} \quad \text{and} \quad \gamma_{xs}^F = -2z \cdot w_{,xs} \quad (19)$$

$$\varepsilon_{xx} = (u_k - z w_k) \phi_{k,xx}; \quad \varepsilon_{ss} = -z w_{k,ss} \phi_k \quad \text{and} \quad \gamma_{xs} = -2z w_{k,s} \phi_{k,x} \quad (20)$$

1.3.2.4 Linear stability analysis

A typical GBT elastic buckling analysis comprises two main steps: (i) cross-section analysis, where the GBT deformation modes and their associated modal mechanical properties

are determined, and (ii) member linear stability analysis, focused on computing the member's stability for each deformation mode. For the arbitrary q -walled member illustrated in Figure 9(a), and considering the cross-section discretisation in Figure 9(b) with $q+1$ natural nodes and m intermediate nodes, a total of $q+m+1$ GBT deformation modes are obtained.

For an illustration purpose, a lipped channel cross-section discretisation is presented in Figure 10(a) – composed of five walls ($q = 5$), resulting in six natural nodes ($q + 1 = 6$) and nine intermediate nodes added ($m = 9$). Figure 10(b) shows the first eight most relevant in-plane shapes (excluding mode 1, which represents axial extension) of deformation modes to illustrate the cross-section deformed configurations. It is worth highlighting that modes 2, 3, and 4 are considered global modes, while modes 5 and 6 are categorised as distortional modes³, and modes 7 and 8 are classified as local-plate modes.

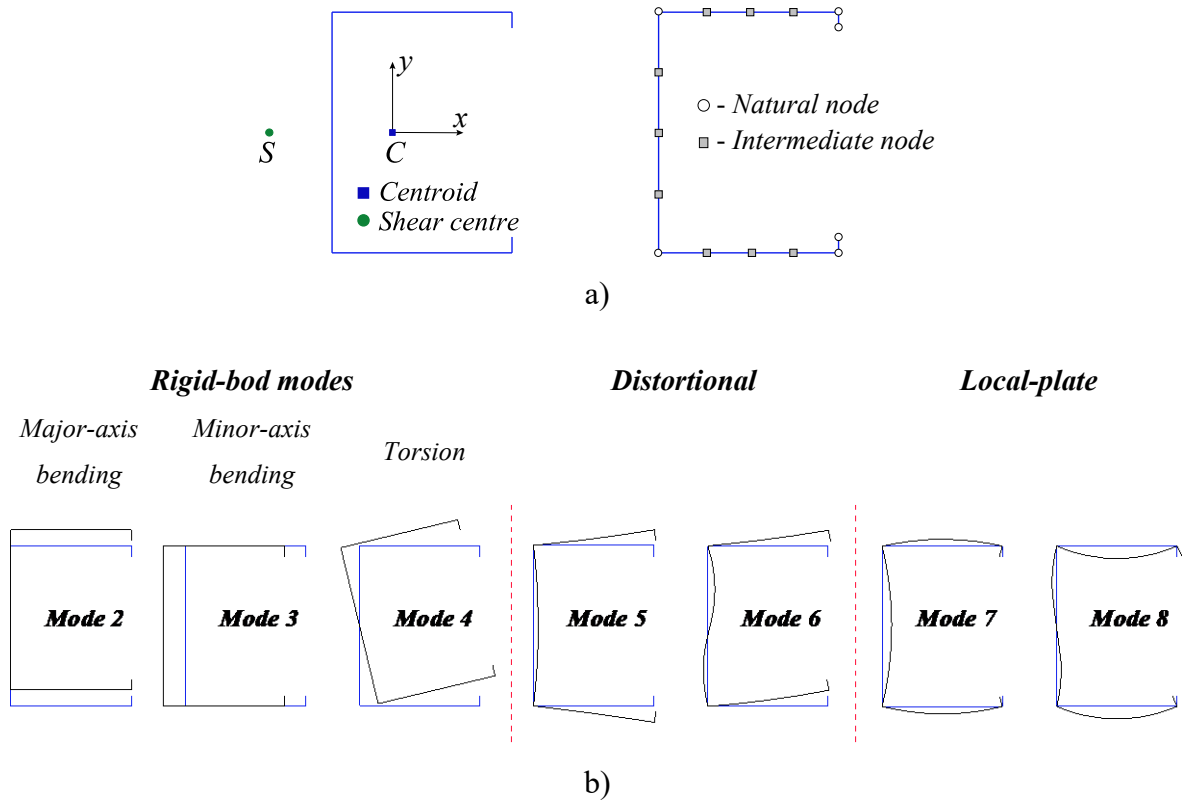


Figure 10: Lipped channel a) cross-section discretisation and b) first eight deformation modes in-plane shapes (rigid-body, distortional and local-plate).

³ It is essential to highlight that equal-leg angle or cruciform sections do not present distortional modes. Thus, modes 5 and 6 become local plate in GBT notation.

Upon following (i) the adoption of Vlasov's assumptions concerning null membrane shear strains and transverse extensions, (ii) consideration of the material constants (Young's modulus E , shear modulus G , and Poisson's ratio ν), and (iii) application of either the principle of virtual work or the principle of stationary potential energy, the GBT system equilibrium equations are derived in Eq. (21), with one equation corresponding to each deformation mode k .

$$EC_{ik}\phi_{k,xxxx} - GD_{ik}\phi_{k,xx} + EB_{ik}\phi_k + \lambda W_{j,0}^\sigma X_{jik}\phi_{k,xx} = 0 \quad (21)$$

$$W_{j,0}^\sigma \delta\phi_{i,x} \Big|_0^L = 0 \quad \left(W_i^\tau + X_{jik} \lambda W_{j,0}^\sigma \delta\phi_{k,x} \right) \delta\phi_i \Big|_0^L = 0 \quad (22)$$

$$W_i^\sigma = EC_{ik}\phi_{k,xx} + GD_{ik}^2\phi_k \quad (23)$$

$$W_i^\tau = -W_{i,x}^\sigma + GD_{ik}\phi_{k,x} \quad (24)$$

Where $W_{j,0}^\sigma$ are the pre-buckling uniform internal force/moment members; λ is the load parameter; C_{ik} , D_{ik} , B_{ik} are the linear stiffness matrices; X_{jik} geometrical stiffness matrix; W_i^σ and W_i^τ are the generalised normal and shear stress resultant arising from the cross-section integration of the displacements and their derivatives.

It is essential to note that once the initial shape functions ($u_k(s)$, $v_k(s)$ and $w_k(s)$) are established, the computation of basic matrices $[C_{ik}]$, $[B_{ik}]$, $[D_{ik}]$, and $[X_{jik}]$ are calculated according to Eqs. (25)-(28), respectively. The initial three terms in Eq. (21) pertain to the first-order member's behaviour, i.e., the linear stiffness matrices C_{ik} , D_{ik} and B_{ik} . Conversely, the last term addresses second-order effects related to the interaction between pre-buckling normal stresses and cross-section out-of-plane deformations, represented by the geometrical effects X_{jik} .

$$C_{ik} = \int_S t u_i u_k ds + \frac{1}{12(1-\nu^2)} \int_S t^3 w_i w_k ds \quad (25)$$

$$B_{ik} = \frac{1}{12(1-\nu^2)} \int_S t^3 w_{i,ss} w_{k,ss} ds \quad (26)$$

$$D_{ik} = \frac{1}{3} \int_S t^3 w_{i,s} w_{k,s} ds - \frac{\nu E}{12G(1-\nu^2)} \int_S t^3 (w_i w_{k,ss} + w_k w_{i,ss}) ds \quad (27)$$

$$X_{jik} = \int_S \frac{tu_j}{C_{jj}} (\nu_i \nu_k + w_i w_k) ds \quad (28)$$

Finally, Eq. (21), together with the specified boundary conditions, yields a standard eigenvalue problem, which provides the member's bifurcation stress resultants and buckling modes, i.e., combinations of the GBT deformation modes along the member length. For instance, Figure 11 depicts a common flexural-torsional critical buckling mode observed in lipped channel columns. This buckling mode is identified in GBT notation by the simultaneous occurrence of cross-section deformation modes 2+4, indicating major-axis flexural buckling and cross-section torsional rotation deformations.

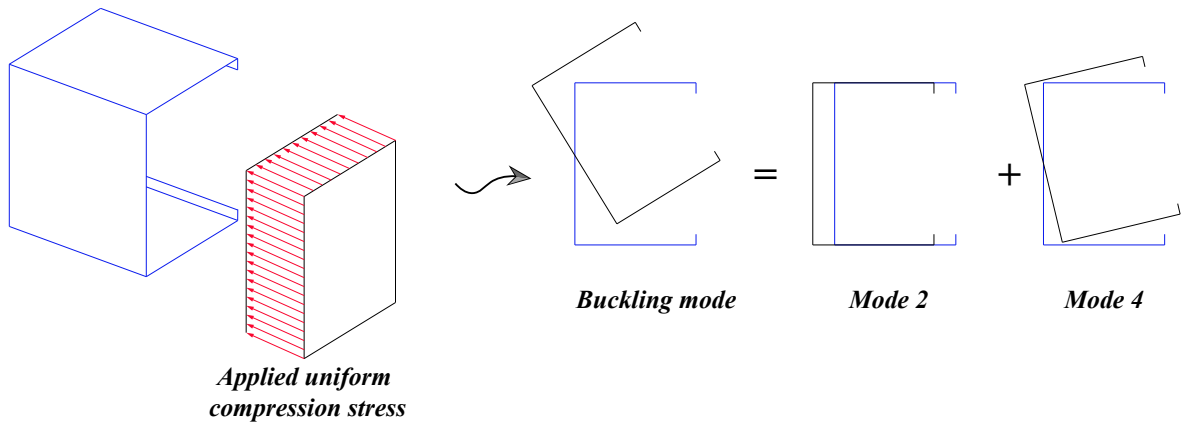


Figure 11: Lipped channel column buckling mode as a linear combination of GBT cross-section deformation modes 2 and 4 (known as flexural-torsional buckling).

Therefore, based on the mechanical properties obtained and by GBT terminology, cross-section deformation modes are classified into four distinct categories based on their mechanical characteristics: (i) flexural, (ii) torsional, (iii) local-plate, and (iv) distortional. A mode is deemed:

- i) Flexural if it exhibits non-zero values for the parameters C_{kk} , while D_{kk} and B_{kk} remain null ($C_{kk} \neq 0, D_{kk} = 0, B_{kk} = 0$);
- ii) Torsional modes, on the other hand, are identified by non-zero values for both C_{kk} and D_{kk} , with B_{kk} being zero ($C_{kk} \neq 0, D_{kk} \neq 0, B_{kk} = 0$);

- iii) Local-plate modes are defined by non-zero values for all three parameters: C_{kk} , D_{kk} , and B_{kk} , coupled with a condition of zero displacement u_k ($C_{kk} \neq 0$, $D_{kk} \neq 0$, $B_{kk} \neq 0$, $u_k = 0$);
- iv) In contrast, distortional modes possess non-zero values for C_{kk} , D_{kk} , and B_{kk} , but with a non-zero displacement u_k ($C_{kk} \neq 0$, $D_{kk} \neq 0$, $B_{kk} \neq 0$, $u_k \neq 0$);

It is worth noting a fundamental distinction between torsional and local modes in the GBT approach: while torsional modes feature straight cross-section walls and rigid-body motions with no transverse curvatures ($w_{k,ss} = 0$) and zero $B_{kk} = 0$, local modes involve transverse bending of the cross-section walls, resulting in non-zero transverse curvatures ($w_{k,ss}$) and non-zero $B_{kk} \neq 0$ values.

1.3.3 Rectangular plates with loaded edges simply supported elastic stability

1.3.3.1 Analytical and energy method solution – Bulson 1970 [15]

Compressive end loads amplify the lateral deflections when a plate is subjected to edge loads only. With a gradual increment in edge loading, a critical point is reached where deflection undergoes a significant increase, eventually leading to infinite deflection, indicative of instability. This critical point marks the onset of elastic plate instability, defined by the minimum compression stress value required to induce this phenomenon, i.e., elastic critical buckling stress (σ_{cr}).

Bulson [15] investigated the elastic stability of rectangular flat plates subjected to uniform compression in one direction (σ_x), with supported loaded edges, characterized by a longitudinal length L and width b . Considering this simplest loading condition, the plates' equilibrium equation is well-known and presented in Eq. (29).

$$\frac{\partial^4 w}{\partial x^4} + \frac{2\partial^4 w}{\partial x^2 \partial y^2} + \frac{\partial^4 w}{\partial y^4} = -\frac{\sigma_x t}{D} \frac{\partial^2 w}{\partial x^2} \quad (29)$$

Where $D = \frac{Et^3}{12(1-\nu^2)}$ is the flexural rigidity of the plate.

Assuming that the plate buckles into m sinusoidal half-waves in the direction of compression (longitudinal). The general solution for displacement w can thus be formulated as presented in Eq. (30). Where $f(y)$ describes the leg transverse deflection (displacement) functions.

$$w = f(y) \sin \frac{m\pi x}{L} \quad (30)$$

Therefore, the fundamental investigation – for this work – carried out by Bulson [15] considers plate boundary conditions where one longitudinal edge is simply supported (S). In contrast, the opposite edge is entirely free (F), as shown in Figure 12(a). In this case, the author demonstrates that the deflected form w_I presented in Eq. (31) can satisfy the specified boundary conditions using energy solutions. Consequently, it is possible to obtain the value of the elastic critical buckling stress (σ_{cr}) and the plate buckling coefficient (k) delineated in Eq. (32) and Eq. (33), respectively. It can be noted that the plate buckling curve $k(\phi)$ does not exhibit a “garland” form, where each “garland” corresponds to a buckling mode characterized by a specific number of sinusoidal half-waves in the load direction (m). Notably, the plate buckling coefficient k tends towards a constant value as the plate's length and leg width (L/b) increases, denoted as ϕ .

This structural behaviour implies two essential observations: (i) the minimum value of k consistently corresponds to the free edge (F) buckling always into a single half-wave number ($m = 1$) regardless of the plate length; (ii) during buckling, there is no plate transverse bending, and the element's deflection forms a flat plane (rigid body rotation) as can be seen in the deflection transverse function employed $f(y) = y/b$. Additionally, (iii) for a Poisson's ratio (ν) of 0.3, the value of k approaches 0.425 as ϕ tends to infinity (∞), i.e., for very long plates.

$$w_I = A_n \frac{y}{b} \sin \frac{m\pi x}{L} \quad (31)$$

$$\sigma_{cr} = \left[\frac{1}{\phi^2} + \frac{6(1-\nu)}{\pi^2} \right] \frac{\pi^2 E}{12(1-\nu^2)} \left(\frac{t}{b} \right)^2 \quad (32)$$

$$k = \left[\frac{1}{\phi^2} + \frac{6(1-\nu)}{\pi^2} \right] \quad (33)$$

These findings are better clarified when contrasting a plate with one edge built-in (B) and the opposite free (F), as illustrated in Figure 12(c). In this second scenario, the deflected

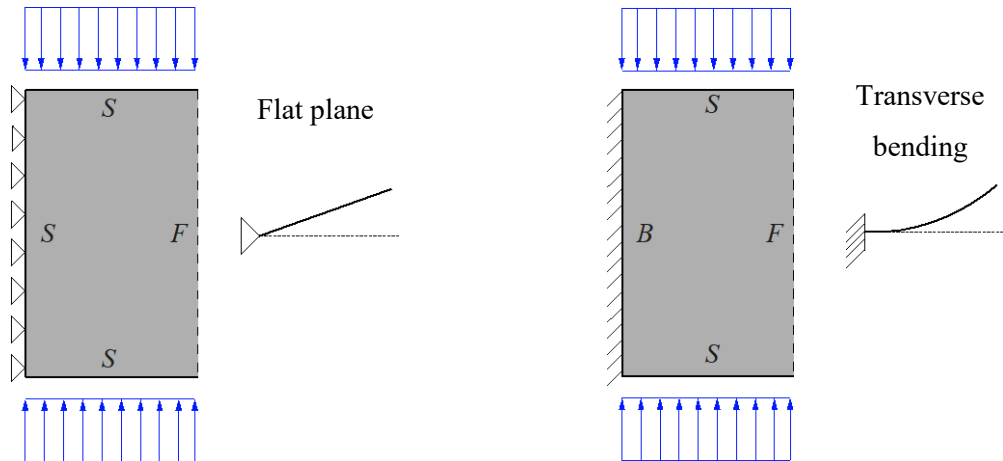
form w_2 presented in Eq. (34) is assumed to satisfy the specified boundary conditions. Hence, by employing the energy method solution specifically for a singular buckling mode $m = 1$ (i.e., one half-wave in the direction of loading regardless of the plate's length), the critical elastic buckling stress (σ_{cr}) and the plate buckling coefficient (k) are derived, as outlined in Eq. (35) and Eq. (36), respectively.

It is noted that the shape of a “garland” curve becomes apparent, reaching a minimum value of k , denoted as k_{min} , and this behaviour signifies (i) a notable increase in wavelengths ($m > 1$) in the longitudinal direction with increasing plate length. Additionally, (ii) plate transverse bending occurs during the buckling, as seen in the deflection transverse function employed $f(y) = [1 - \cos(\pi y/2b)]$. Finally, taking Poisson's ratio (ν) of 0.3, the minimum value of k is observed at 1.424 when $\phi = 1.636$.

$$w_2 = A_n \left(1 - \cos \frac{\pi y}{2b} \right) \sin \frac{m\pi x}{L} \quad (34)$$

$$\sigma_{cr} = \left[\frac{1}{\phi^2} + \frac{\pi\phi^2}{16(3\pi-8)} + \frac{\pi-4\nu}{2(3\pi-8)} \right] \frac{\pi^2 E}{12(1-\nu^2)} \left(\frac{t}{b} \right)^2 \quad (35)$$

$$k = \left[\frac{1}{\phi^2} + \frac{\pi\phi^2}{16(3\pi-8)} + \frac{\pi-4\nu}{2(3\pi-8)} \right] \quad (36)$$



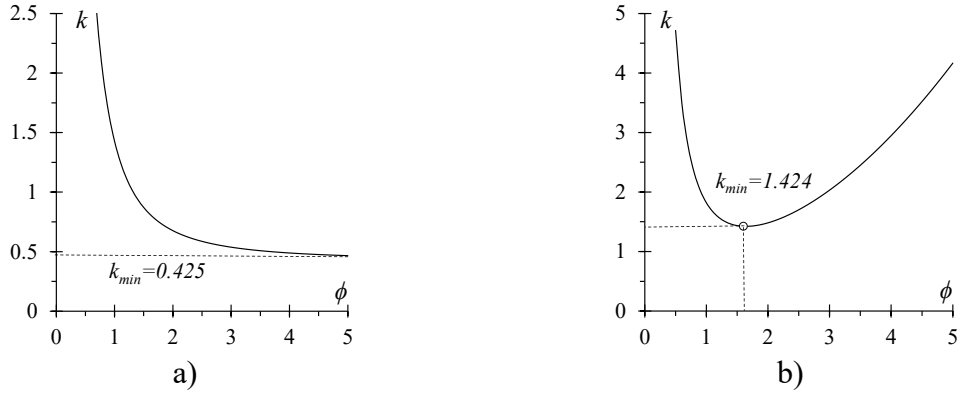


Figure 12: Rectangular plate in end compression with a) longitudinal edge simply supported and other free (S-F) and b) longitudinal edge built-in and other free (B-F) [15].

1.3.3.2 Generalized Beam Theory (GBT) approach

Similarly, in 2010, Dinis *et al.* [30] expanded the investigation conducted by Bulson [15], presenting the results of an outstand flange stability analysis using Generalized Beam Theory (GBT). It is important to highlight the significant distinction between torsional and local modes, as described in 1.3.2. Recalling in GBT notation, (i) torsional modes are characterized by straight cross-section walls undergoing rigid-body motions. On the other hand, (ii) local modes involve transverse bending of the cross-section walls, resulting in non-null transverse curvatures.

Therefore, this study assessed an outstand flange with length L and width b uniformly compressed along the simply supported transverse edges ($x = 0$ and $x = L$). In contrast, the longitudinal edges are load-free, i.e., plates with identical dimensions and loading conditions studied by Bulson [15]. However, the authors extended the boundary conditions, with the longitudinal supported edge at $s = 0$ being elastically restrained by a rotational spring with stiffness S , and the edge $s = b$ is maintained free.

The investigation included two GBT deformation mode analyses, as shown in Figure 13: (i) mode 1, which exhibits a rigid-body rotation of the plate about the elastically restrained edge $s = 0$, and (ii) mode 2, which has a null rotation at the elastically restrained edge $s = 0$ but exhibits transverse bending. The local plate buckling coefficient (k_{cr}) was evaluated as a function of the plate aspect ratio ($\phi = L/b$), for several values of the dimensionless rotational stiffness parameter (α) – Eq. (37), as presented in Figure 14.

$$\alpha = \frac{12Sb}{Et^3}(1-\nu^2) \quad (37)$$

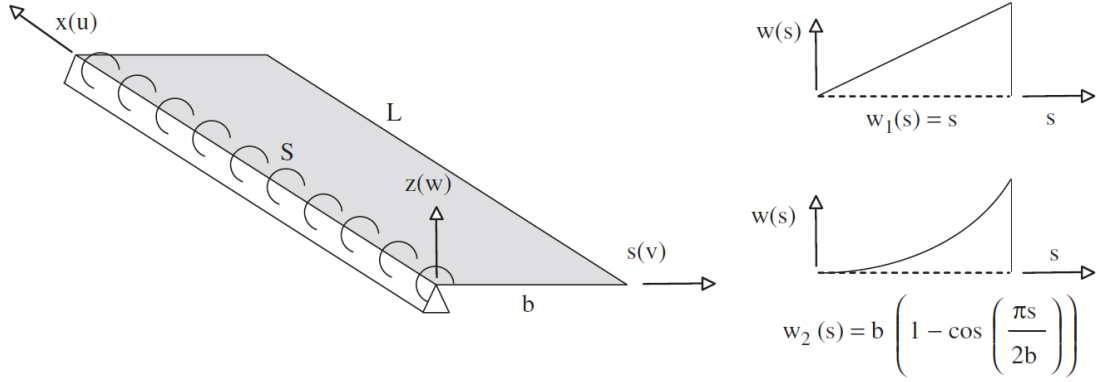


Figure 13: Elastically restrained outstanding flange and two GBT deformation modes included in the analysis [30];

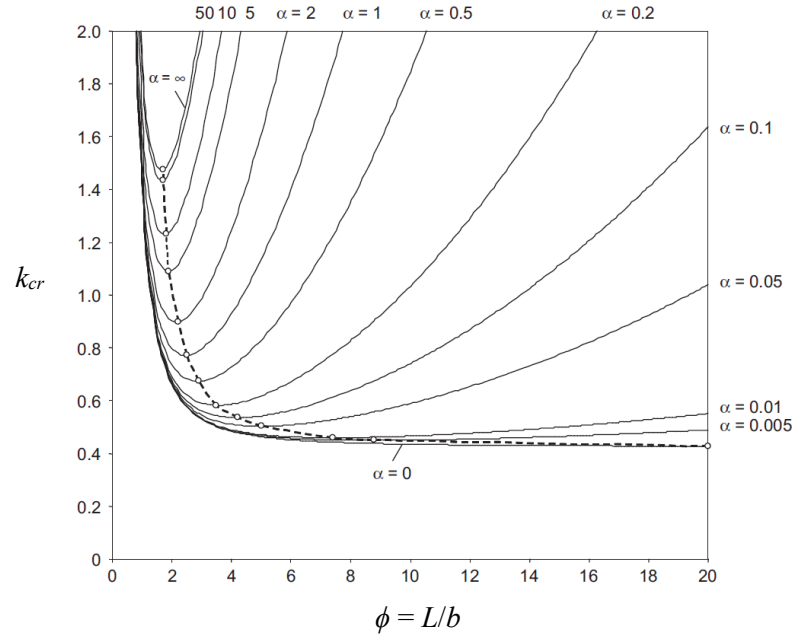


Figure 14: Variation of buckling coefficient k_{cr} with the aspect ratio ϕ and α [30].

The authors concluded that for $\alpha = 0$, i.e., no rotational stiffness, the curve $k_{cr}(\phi)$ is monotonically descendent (no local minimum exists) and tends to $k_{cr} = 0.425$ – same conclusion obtained in Bulson [15]. The flange buckles in a single half-wave mode regardless of its length L (or ϕ). This means that a simply supported flange with a length larger than four times its width

($L > 4b$) always buckles in a single half-wave mode without transverse bending. Mechanically speaking, the buckling mode involves pure torsion about the simply supported edge, which is designated as global mode 4 (torsion) in GBT. However, in all curves where $\alpha > 0$, a local minimum is observed in $k_{cr}(\phi)$. This pattern signifies that even a slight spring rotational stiffness results in flange buckling with multiple half-waves ($m > 1$). Moreover, with increasing values of α , the corresponding minimum k_{cr} increases as the corresponding ϕ values decrease. This trend occurs due to the changing contributions of modes 1 and 2: as the contribution of mode 1 decreases, the contribution of mode 2 increases. Therefore, in accordance with GBT, the presence of rotational stiffness along the longitudinal supported edge is imperative for local plate buckling.

1.3.3.3 Finite element numerical analysis

This work employed a shell finite element model in ANSYS 17.0 [29] software to illustrate the elastic buckling behaviour of plates under uniform compressive loading, considering the two cases examined by Bulson (S-F and B-F), as depicted in Figure 15. The numerical model incorporates (i) a 5 mm x 5 mm element size, (ii) an elastic plate material with properties $E = 210000$ MPa and $\nu = 0.3$, and (iii) three different geometries defined by dimensionless ratios ϕ of 4, 6, and 8 (i.e., L/b).

The results obtained are presented in Table 2, indicating the dimensionless aspect ratio (ϕ), the elastic critical buckling mode, and the number of half-waves in the longitudinal direction (m) for the two specified boundary conditions. The following comments can be made:

In the scenario designated as S-F, where one longitudinal edge is simply supported, and the opposite edge remains free, it was consistently noted that, regardless of the plate length (L), a singular half-wave ($m = 1$) alongside rotation of the transverse section were invariably manifested, in alignment with findings reported by Bulson [15] and Dinis *et al.* [30]. This pattern intimates a predominately global torsional buckling mode, distinctly marked by torsional phenomena around the simply supported edge.

In contrast, under the B-F condition – where one longitudinal edge is rigidly fixed, and the opposite edge is free – a local plate buckling behaviour emerged. With increasing plate length, a proliferation of half-waves was observed along the longitudinal axis. Additionally, unlike the S-F condition, the B-F condition was associated with transverse section bending,

further highlighting the influence of boundary conditions on the buckling behaviour of the plates.

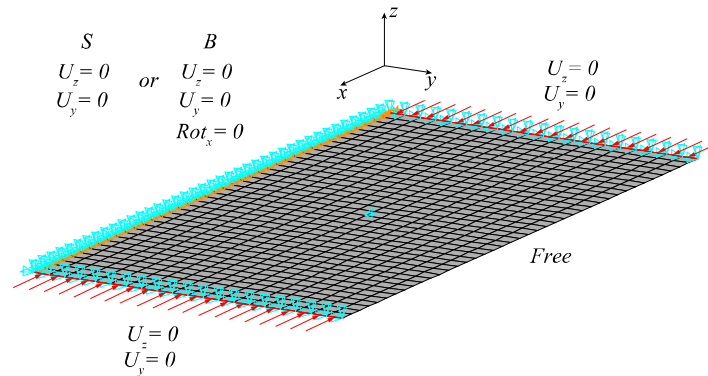
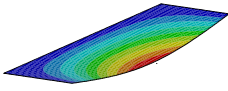
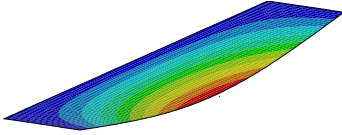
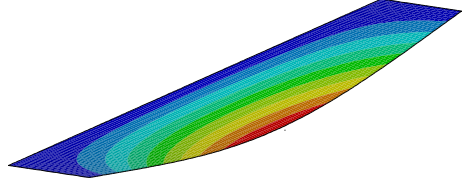
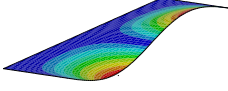
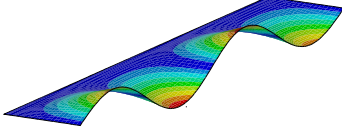
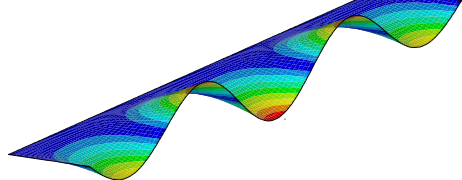


Figure 15: Finite element model elastic buckling analysis of simply supported (S) or built-in (B) longitudinally rectangular plate with other free.

Table 2: Comparison of longitudinal free edge sinusoidal half-wave plate deformation patterns between S-F and B-F varying the aspect ratio ϕ .

	$\phi (L/b)$		
	4	6	8
S-F	 $m = 1$	 $m = 1$	 $m = 1$
B-F	 $m = 2$	 $m = 4$	 $m = 5$

1.3.4 Equal-leg angle columns' elastic buckling behaviour

1.3.4.1 Simply supported steel equal-leg angle columns

In 2010, Dinis *et al.* [30] presented an analytical approach based on Generalized Beam Theory (GBT) – cross-section deformation modes – to investigate the buckling behaviour of simply supported steel slender equal-leg angle columns. This work was essential in effectively distinguishing the mechanical characteristics between local and torsional deformations in these members.

As discussed in Section 1.3.3.2, according to the GBT principles, the global torsional buckling mode is characterised by rigid-body movement, meaning there is no deformation in the cross-section. Consequently, the cross-section geometry remains unchanged, and the elements remain straight. Conversely, the local buckling mode is identified by longitudinal half-waves, indicating transverse bending within the element. This distinction between torsional and local buckling mode along the member length is elucidated and illustrated in Figure 12 and Table 2, respectively.

Therefore, Figure 16(a) presents the mid-lines equal-leg cross-section discretisation applied, identifying three GBT global modes (2-4) and $2q-1$ local deformation modes – where “ q ” signifies the number of cross-section walls. These modes comprise three rigid-body deformations, precisely bending about the major-axis (mode 2), bending about the minor-axis (mode 3), and pure torsion (mode 4), alongside three local modes 5, 6, and 7, as depicted in Figure 16(b).

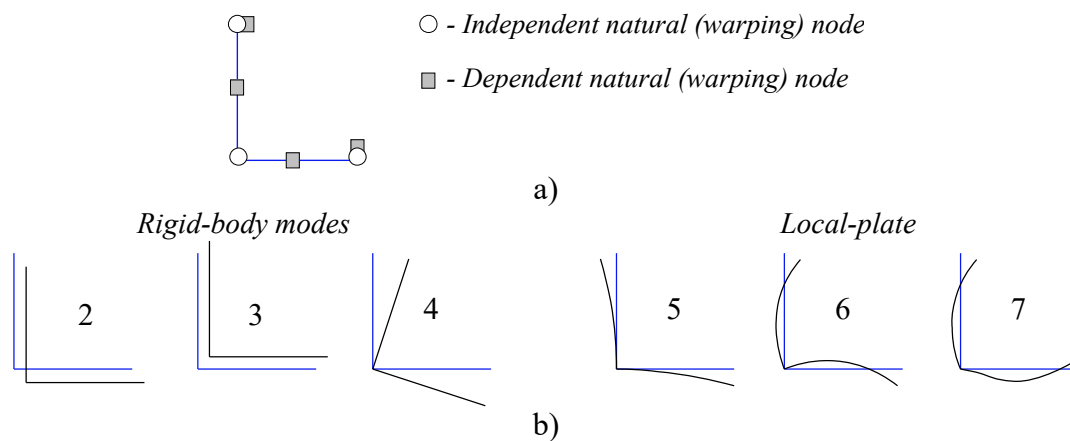


Figure 16: Equal-leg angle cross-section GBT a) discretisation and b) in-plane deformation mode shapes (2-7) [30].

Figure 17(a) and (b) present the results obtained from the GBT analysis, elucidating the elastic buckling behaviour of simply supported columns featuring equal-leg angle cross-section $L70 \times 70 \times 1.2$ mm, i.e., high width-to-thickness ratio (b/t) equal to 58.33. It depicts the elastic

critical buckling load as the column length increases on a logarithmic scale – the so-called “signature” curve P_b vs. L – and the column lengths modal participation diagram. This diagram quantifies each GBT deformation mode’s contribution to the column’s critical buckling modes, offering new insights into their mechanical characteristics.

From these findings, the following primary observations must be highlighted:

- i) Across the entire length range ($L = 4$ cm to 2000 cm), the critical buckling behaviour of angle columns can be characterized by just four cross-section deformation modes (2, 3, 4, 6);
- ii) For very short columns ($L < 30$ cm) – highlighted in red – buckling occurs in a combination of torsional and local modes (i.e., 4+6). Figure 17(c) illustrates the deformed shape of the cross-section at the mid-span for a column length $L = 5$ cm. As the length increases, ranging from very short to short lengths ($30 < L < 80$ cm) – highlighted in blue – columns buckle in pure torsional mode, i.e., mode 4;
- iii) Columns with intermediate lengths ($80 < L < 400$ cm), highlighted in green, demonstrate buckling behaviour characterized by a combination of major-axis flexural and torsional modes (2+4), commonly referred to as flexural-torsional buckling. These behaviours are illustrated in Figure 17(c) for column lengths of 100 cm and 300 cm, respectively. For a column length of 100 cm, the buckling is predominantly in the pure torsional mode (mode 4). Whereas as the column length increases ($L = 300$ cm), major-axis flexural buckling participation becomes more evident, characterized by cross-section corner displacement;
- iv) For longer columns ($L > 400$ cm) – highlighted in yellow – buckling occurs in a pure minor-axis flexural mode (mode 3), as illustrated in Figure 17(c) for column lengths of 1000 cm;
- v) In general, the critical load (P_b) consistently decreases monotonically with the length, corresponding to a single half-wave buckling mode ($m = n_w = 1$). The torsion mode 4 almost always plays a key role. Therefore, the authors concluded that for columns categorized as short to intermediate, i.e., in a practical range ($30 < L < 400$ cm), the global torsional buckling (mode 4) predominates.

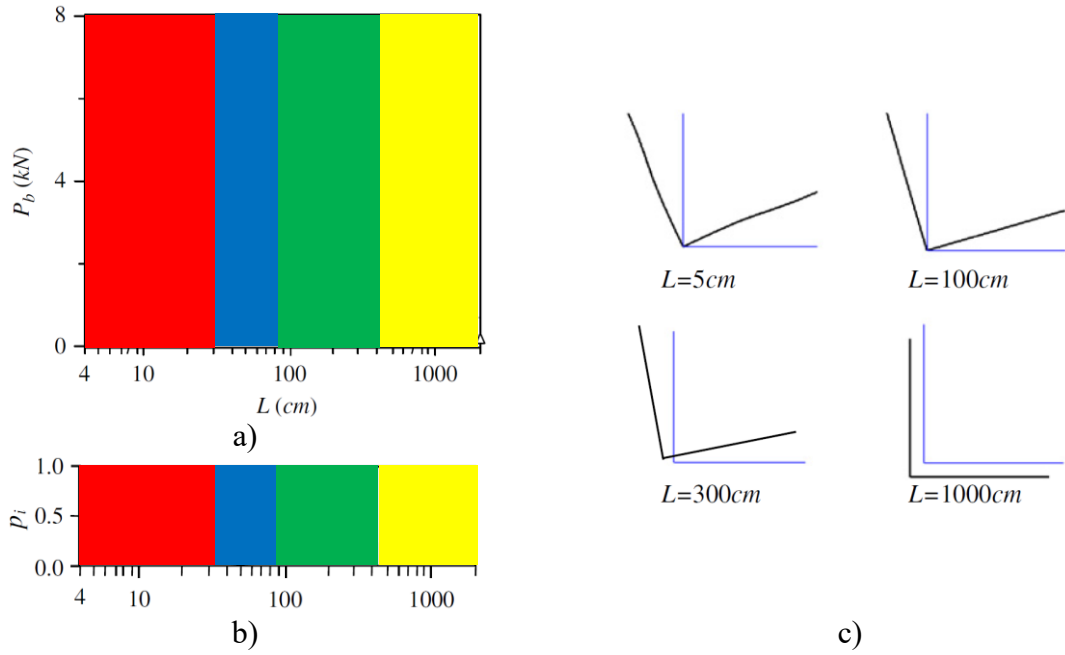


Figure 17: Equal-leg angle column buckling behaviour a) P_b vs. L curves, b) modal participations diagram, and c) critical buckling mode shapes of columns with different lengths [30].

1.3.4.2 Secondary warping constant (I_{ws})

Dinis *et al.* [30] show that despite the equal-leg angle sections exhibiting no primary warping resistance ($I_w = 0$), the warping cross-section resistance is derived solely from the secondary warping constant ($I_{ws} \neq 0$). The authors demonstrate this mechanical behaviour considering only mode 4 (torsional) in the GBT buckling analysis. In other words, this statement can be demonstrated considering the displacement in each wall equal to Eq. (38), i.e., the flexural displacement in each wall is equal to s (a linear function, as illustrated in Figure 13).

$$w_4 = s \quad (38)$$

Based on this displacement field and introducing Eq. (38) in Eqs. (25)-(28), it is possible to calculate the modal geometrical properties referring to mode 4 as expressed in Eqs. (39)-(42).

$$C_{44} = \frac{1}{12(1-\nu^2)} \int_S t^3 w_4^2 ds = \frac{1}{12(1-\nu^2)} \int_S t^3 s^2 ds = \frac{1}{12(1-\nu^2)} \sum_{wall\ i} \frac{1}{3} t_i^3 b_i^3 = \frac{I_{ws}}{12(1-\nu^2)} \quad (39)$$

$$B_{44} = \frac{1}{12(1-\nu^2)} \int_S t^3 w_{4,ss} w_{4,ss} ds = 0 \quad (40)$$

$$D_{44} = \frac{1}{3} \int_S t^3 w_{4,s}^2 ds = \frac{1}{3} \int_S t^3 ds = \frac{1}{3} \sum_{wall\ i} t_i^3 b_i^3 \equiv J \quad (41)$$

$$X_{144} = \frac{1}{A} \int_S t w_4^2 ds = \frac{1}{A} \int_S t s^2 ds = \frac{1}{A} \sum_{wall\ i} \frac{1}{3} t_i^3 b_i^3 = \frac{I_0}{A} \quad (42)$$

Where I_{ws} is the secondary warping constant and I_0 is the polar moment inertia with respect to the shear centre. It is worth mentioning that modal property B_{44} is null due to its dependency on the second derivative of the displacement field – for this cross-section deformation mode, there is no transverse bending. This mechanical behaviour illustrates that the equal-leg angle cross-sections' resistance relies solely on properties C_{44} and D_{44} .

Subsequently, the GBT system equilibrium equation for mode 4 – Eq.(21) – is solved according to columns' boundary condition to derive the critical elastic load, identified as P_4 and expressed in Eq. (43). Furthermore, incorporating Eqs. (39), (41), and (42) into Eq. (43) yields the familiar torsional buckling formula ($P_{cr,T}$) outlined in Eq. (44).

$$P_4 = \frac{1}{X_{144}} \left[EC_{44} \left(\frac{\pi}{L} \right)^2 + GD_{44} \right] \quad (43)$$

$$P_4 = P_{cr,T} = \frac{A}{I_0} \left[\frac{EI_{ws}}{12(1-\nu^2)} \left(\frac{\pi}{L} \right)^2 + GJ \right] \quad (44)$$

By expressing the geometrical properties, i.e., the polar moment inertia (I_0), the secondary warping constant (I_{ws}), and the torsional constant (J), in terms of the cross-section's geometry formed by two plates ($i = 2$) sharing the same width and thickness (b and t), and following some algebraic manipulations – as detailed in Eqs. (45)-(47) – the elastic critical torsional buckling load derives into Eq. (48).

$$P_{cr,T} = \frac{A}{\sum_{wall\ i} \frac{1}{3} t_i b_i^3} \left[\frac{E \sum_{wall\ i} \frac{1}{3} t_i^3 b_i^3}{12(1-\nu^2)} \left(\frac{\pi}{L} \right)^2 + G \sum_{wall\ i} \frac{1}{3} t_i^3 b_i \right] \quad (45)$$

$$P_{cr,T} = \frac{A}{\frac{2}{3} t b^3} \left[\frac{E \frac{2}{3} t^3 b^3}{12(1-\nu^2)} \left(\frac{\pi}{L} \right)^2 + G \frac{2}{3} t^3 b \right] \quad (46)$$

$$P_{cr,T} = A \left[\frac{3}{2 t b^3} \frac{2 t^3 b^3}{3} \frac{E}{12(1-\nu^2)} \left(\frac{\pi}{L} \right)^2 + G \frac{2 t^3 b}{3} \frac{3}{t b^3} \right] \quad (47)$$

$$P_{cr,T} = A \left[\frac{E t^2}{12(1-\nu^2)} \left(\frac{\pi}{L} \right)^2 + G \left(\frac{t}{b} \right)^2 \right] \quad (48)$$

Moreover, the critical torsional stress ($\sigma_{cr,T}$) can be calculated by dividing the critical load and the cross-section area (A), as shown in Eq. (49). In order to establish a correlation with plate behaviour, it is possible to derive an equation for the critical stress based on the inverse of the plates' aspect ratio ($\phi = L/b$) that composed the cross-section, considering that $G = E/2(1+\nu)$, as expressed in Eq. (50).

$$\sigma_{cr,T} = \frac{P_{cr,T}}{A} = \frac{E t^2}{12(1-\nu^2)} \left(\frac{\pi}{L} \right)^2 + G \left(\frac{t}{b} \right)^2 \quad (49)$$

$$\sigma_{cr,T} = \underbrace{\left[\left(\frac{b}{L} \right)^2 + \frac{6(1-\nu)}{\pi^2} \right]}_k \frac{E \pi^2}{12(1-\nu^2)} \left(\frac{t}{b} \right)^2 \quad (50)$$

Therefore, the authors [30] show that (i) the initial bracketed term represents the equal-leg angle cross-sections' secondary warping stiffness (I_{ws}) and (ii) it is crucial to be maintained in buckling analysis to accurately capture the initial downward trend of the equal-leg angle columns buckling signature curves – shown in Figure 17. Additionally, considering Poisson's ratio ($\nu = 0.3$), this initial term gradually diminishes for longer columns ($L \rightarrow \infty$), resulting in a plate buckling coefficient ($k = 0.425$) identical to that obtained by Bulson for plates S-F as

shown in Eq. (33). Thus, it is evident that, in equal-leg angle columns elastic buckling behaviour, torsional deformations prevails as the predominant mode. Moreover, accurate prediction of the elastic buckling behaviour necessitates the consideration of secondary warping effects in analysis to capture the actual structural behaviour.

1.3.4.3 Boundary conditions employed in experimental investigations (F, PC and PS)

In 2012, Dinis *et al.* [31] extended research on carbon steel cold-formed equal-leg angle columns. They conducted a numerical study using the computational code based on Generalised Beam Theory – GBTul [32] – and the finite element software ABAQUS [33] to investigate equal-leg angle columns' elastic buckling behaviour under boundary conditions employed in experimental tests.

The authors adopted the same cross-section of $L70 \times 70 \times 1.2$ mm investigated in the previous work [30], where rounded corners were disregarded, resulting in negligible primary warping ($I_w = 0$). In order to ensure experimental boundary conditions, secondary warping and local/displacement rotations at the supports are restrained (i.e., rigid end plates). Consequently, global torsional rotations were always consistently prevented. As for global flexural rotations, the analysis addresses three distinct conditions: (i) both major and minor-axis bending are constrained (fixed end sections – F condition), (ii) only major-axis bending is restricted (“cylindrically pinned” end sections – PC condition), and (iii) both major and minor-axis bending are unrestricted (“spherically pinned” end sections – PS condition).

The results for each boundary (F, PC and PS) are depicted in Figure 18(a) in terms of the critical elastic buckling load versus column length (on a logarithmic scale) – P_{cr} vs. L – where each curve represents a boundary condition. Figure 18(b) presents the modal participation diagrams, and Figure 18(c) depicts the cross-section deformation at mid-span ($L/2$) for two column lengths ($L = 100$ and 364 cm) with cylindrically pinned end (PC). These buckling findings lead to the following remarks:

- i) Throughout the entire range of lengths, the primary buckling modes of all columns exclusively involve deformation modes 2, 3, 4, and 6, notably excluding the symmetric local mode 5;
- ii) Equal-leg angle short-to-intermediate columns exhibit flexural-torsional buckling, i.e., a combination of GBT modes 2 (major-axis bending) and 4

- (torsion), due to the cross-section's symmetry concerning the major-axis. However, it is essential to note in Figure 18(b) that the mode 2 increases as the length increases, being almost imperceptible at short length (but not zero);
- iii) The three support conditions (F, PC and PS) exhibit similar characteristics regarding elastic buckling behaviour. The critical load (P_{cr}) decreases with length (L) and corresponds always to a single sinusoidal half-wave ($m = 1$). Results obtained via GBT and ABAQUS (FEM) are coincident, and mode 4 (torsion) is extremely important as it manifests in all lengths (except in cases where buckling occurs about the minor-axis – mode 3);
- iv) Regarding the support conditions F and PC for short-to-intermediate columns, the difference lies in the transition length (L_T) between flexural-torsional buckling and minor-axis bending. For PC columns, the transition occurs at a length of $L = 420$ cm, while for F columns, it occurs at $L = 890$ cm. In other words, for columns with $L < 420$ cm, flexural-torsional mode occurs with identical critical loads for both boundary conditions;
- v) Concerning the PC support conditions for short to intermediate columns, the difference lies at the end of the plateau due to the participation of mode 2, representing a transition critical load for PS columns 7.4% lower than PC columns.

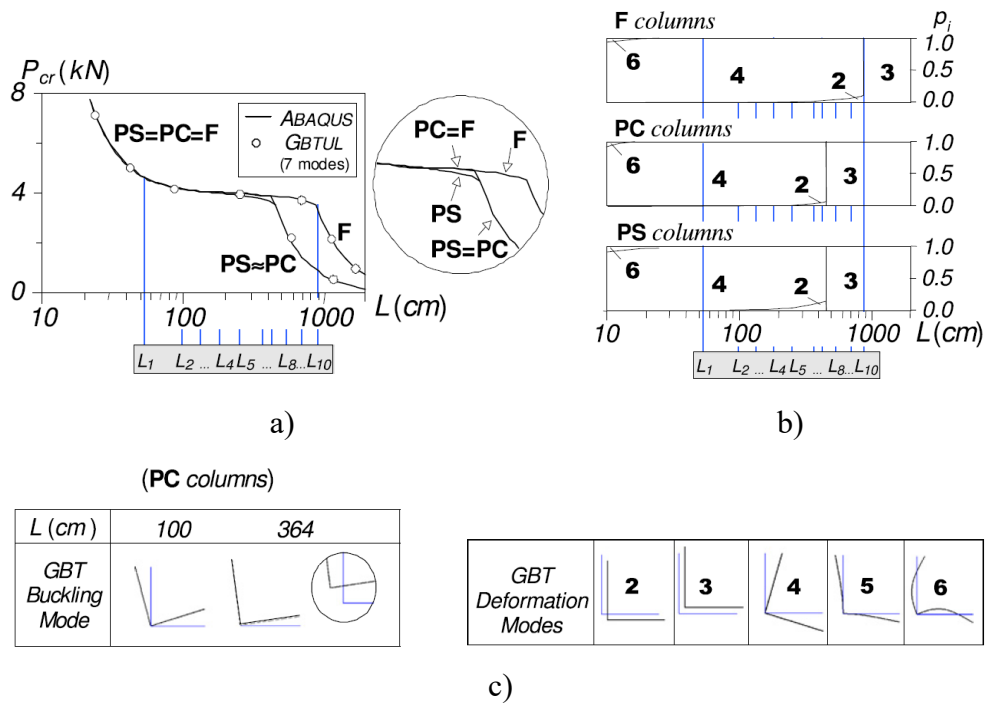


Figure 18: (a) P_{cr} vs. L curves, (b) GBT modal participation diagrams for F, PC, and PS columns, and (c) in-plane shapes of 2 buckling modes and the first 5 GBT deformation modes for PC columns [31].

1.3.5 Fixed-ended equal-leg angle column's elastic post-buckling behaviour

Dinis *et al.* [31] extended the numerical study using shell finite element analyses through ABAQUS [33] to investigate the elastic post-buckling behaviour of short-to-intermediate fixed-ended equal-leg angle columns, i.e., featuring flexural-torsional critical modes with initial geometrical imperfections having an amplitude equal to 10% of the thickness (i.e., $0.1t$). This approach corresponds to mid-span torsional rotations of approximately $\beta_0 = 0.098$ rad (recall that the equal-leg angle cross-section is $L70 \times 70 \times 1.2$ mm).

The short-to-intermediate columns investigated length varying are equal to: $F_1 = 53$ cm, $F_2 = 98$ cm, $F_3 = 133$ cm, $F_4 = 182$ cm, $F_5 = 252$ cm, $F_6 = 364$ cm, $F_7 = 420$ cm, $F_8 = 532$ cm, $F_9 = 700$ cm, and $F_{10} = 890$ cm – as illustrated in Figure 18. It is essential to highlight that the F_{10} corresponds to the column transition length (L_T), i.e., the transition between flexural-torsional and minor-axis flexural buckling critical mode.

Figure 19(a) shows the upper parts of the elastic post-buckling equilibrium paths (P/P_{cr} vs. β) for columns $F_1 - F_{10}$, where P/P_{cr} is the ratio between the applied load and elastic torsional critical load, and β denotes the mid-span clockwise rigid-body rotation. These post-buckling results prompt the following remarks:

- i) As the length (L) increases, the equilibrium paths (P/P_{cr} vs. β) become progressively more flexible. Additionally, columns from F_1 to F_{10} demonstrate qualitatively different post-buckling behaviours. While (i₁) the shorter columns (F_1 to F_7) exhibit evident stability, (i₂) the longer ones (F_8 to F_{10}) display well-defined limit points. These limit points manifest as abrupt changes followed by significant torsional rotation reversals (F_8 to F_9) or smooth transitions without torsional rotation reversals (F_{10}). Moreover, noticeable corner displacements are observed in the longer columns, as depicted in detail in Figure 19(a) for the F_9 column;
- ii) In columns, F_8 and F_9 , the flexural-torsional deformation pattern transitions from a single half-wave to three half-waves upon reaching the peak load (i.e., the limit point), and this transition occurs for progressively smaller values of β as the length L increases (F_8 to F_9). This configuration transition is evident in Figure 19(b), where a comparison of the mid-span ($L/2$) and quarter-span ($L/4$) cross-section deformation of the F_9 column reveals opposite rotations, corresponding to the post-peak equilibrium state 3;

- iii) This behaviour can be explained by the significant occurrence of flexure, primarily along the minor axis, within the column, resulting in tensile stress within the corner regions of the cross-section. It is important to highlight that the flexural displacements along both the major and minor axes play a role in the torsional rotations observed along the descending branch of the equilibrium path of the F_9 column, which is linked to significant reversals in torsional rotation;
- iv) Figure 20 shows that the mid-line cross-sections' normal stress distribution remains uniform for all columns until practically $P/P_{cr} \approx 0.8$. However, as the load increases, the stress distribution becomes progressively non-uniform, i.e., the stresses are practically linear in both legs and gradually “shift” from the leg edges towards the corner. However, their distributions exhibit differences between shorter and longer columns. Specifically, the stresses are practically symmetric for the shorter columns (F_3), while they are clearly asymmetric for the longer columns (F_9);
- v) Furthermore, it is worth noting that neither of the stress distributions aligns with the widespread belief proposed by Rasmussen [12] that short-to-intermediate equal-leg angle columns exhibit a parabolic normal stress distribution with a higher value at the corner. In other words, each leg does not behave like a pinned-free longitudinally long plate (S-F).

The results obtained unveiled some unexpected behavioural characteristics concerning fixed-ended short-to-intermediate equal-leg angle columns. Despite their critical stresses or loads remaining relatively consistent across different lengths, as shown by an almost horizontal plateau in the P_{cr} vs. L curve – Figure 18(a), these fixed-ended columns demonstrate notably diverse elastic post-buckling behaviours. They display a broad spectrum of post-critical strength reserve levels, varying from relatively high (for smaller lengths – F_1) to rather low (for larger lengths – F_{10}), indicative of post-buckling behaviours ranging from stable to unstable.

The magnitude of corner flexural displacements emerged as a significant factor in distinguishing between these various short-to-intermediate columns' post-buckling behaviours. Therefore, the observed disparity between the post-buckling behaviours of fixed-ended equal-leg angle columns arises from the occurrence of corner flexural displacements (i.e., major and minor axis flexural), evident in the longer columns (F_8 - F_{10}).

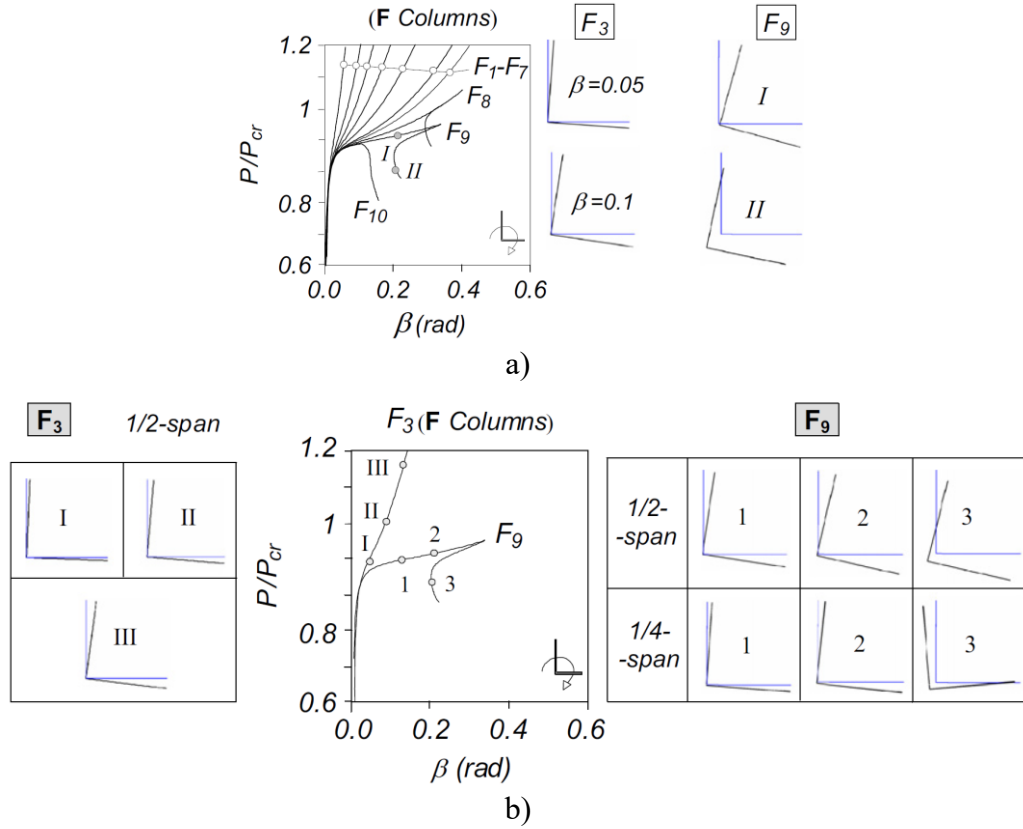


Figure 19: a) F_1 - F_{10} columns mid-span equilibrium paths P/P_{cr} vs. β and b) F_3 and F_9 columns cross-section deformed configuration evolutions [31].

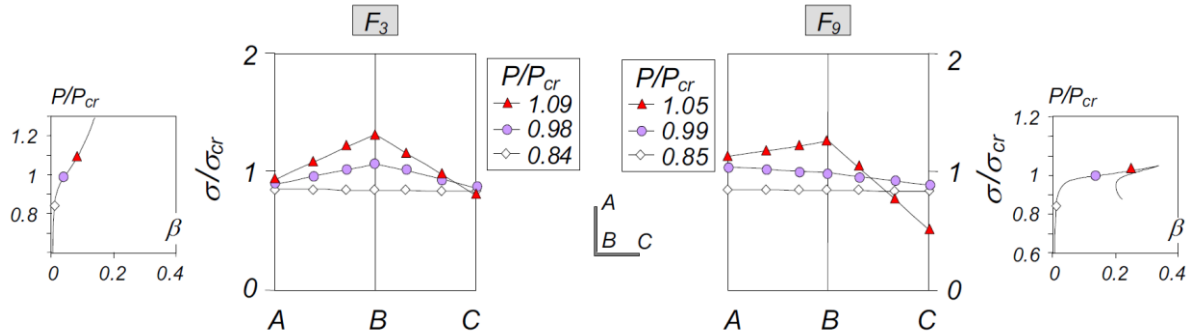


Figure 20: Evolution of the F_3 and F_9 column mid-span normal stress distribution concerning three load levels [31].

In order to gain insight into how flexural displacements influence the post-buckling behaviour of fixed-ended angle columns, the evolution of corner section displacements in columns F_3 , F_6 , and F_9 columns are investigated. Thus, Figure 21(a) and (b) illustrate the upper portions of the corresponding post-buckling equilibrium paths (P/P_{cr} vs. d_M/t and P/P_{cr} vs. d_m/t), where d_M and d_m represent the mid-span ($L/2$) corner displacements resulting from major-axis

and minor-axis flexure, respectively (i.e., minor-axis displacement and major-axis displacement). Additionally, Figure 22(a) and (b) show the longitudinal profile displacement along the normalised columns' length (x_3/L) and different scales for d_M/t and d_m/t for each column. For instance, the values for the F_9 column are 80 times larger than those for the F_3 column. Among several conclusions obtained by the authors, the main ones deserve to be highlighted:

- i) Major-axis flexural displacements (d_M) are observed in the critical buckling mode, as indicated by the mode 2 participation diagram in Figure 18(a). Consequently, these displacements are integrated into the columns' initial geometrical imperfections. Therefore, it is expected that the d_M value will progressively increase with the applied load. Moreover, their longitudinal displacement profiles exhibit the typical mode shape seen in fixed-ended column critical buckling, which includes one inner half-wave and two outer “quarter-waves” with zero end slopes. This pattern is depicted in Figure 22(a);
- ii) For the shorter (F_3) and intermediate (F_6) columns, the equilibrium paths of P/P_{cr} vs. d_M/t progress steadily, with the d_M values consistently remaining relatively small, showing an increase with L . This trend is not observed in the longer (F_9) column's equilibrium path, which progresses steadily until approximately $P/P_{cr} = 1.05$. Subsequently, it undergoes a sudden “ d_M reversal” coinciding with a similarly abrupt increase in minor-axis flexural displacements (d_m);
- iii) As the column lengths increase, the critical buckling load for minor-axis flexural buckling (P_{cre}) approaches the flexural-torsional buckling load (P_{crft}). In other words, the relationship between these critical loads for columns F_3 , F_6 , and F_9 are 27.1, 5.5 and 1.6, respectively. Thus, it is explained the increase in minor-axis flexural displacements (d_m) for the longer column (F_9);
- iv) Consequently, in longer columns ($F_7 - F_9$), this influence means “buckling mode interaction”, i.e., a significant interaction between flexural-torsional buckling and minor-axis flexural buckling displacements. Specifically, the flexural-torsional and flexural buckling loads for these columns are initially relatively close and become even closer due to the reduction in axial stiffness associated with the flexural-torsional post-buckling behaviour;
- v) Finally, the occurrence of displacements in both the major and minor axes, along with the fully restrained end condition (fixed-ended), accounts for the linear distribution of normal stresses in the cross-sectional area (see Figure 20).

Furthermore, the asymmetry in the normal stress distribution, minimal for column F_3 and pronounced for column F_9 , reflects the combination of moments about both major and minor axes.

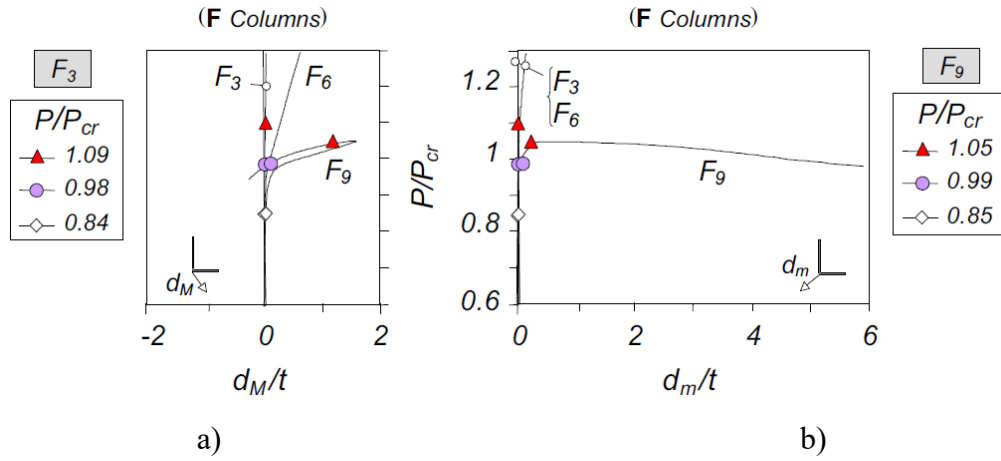


Figure 21: F_3 , F_6 , and F_9 columns a) P/P_{cr} vs. d_m/t and b) P/P_{cr} vs. d_m/t equilibrium paths [31].

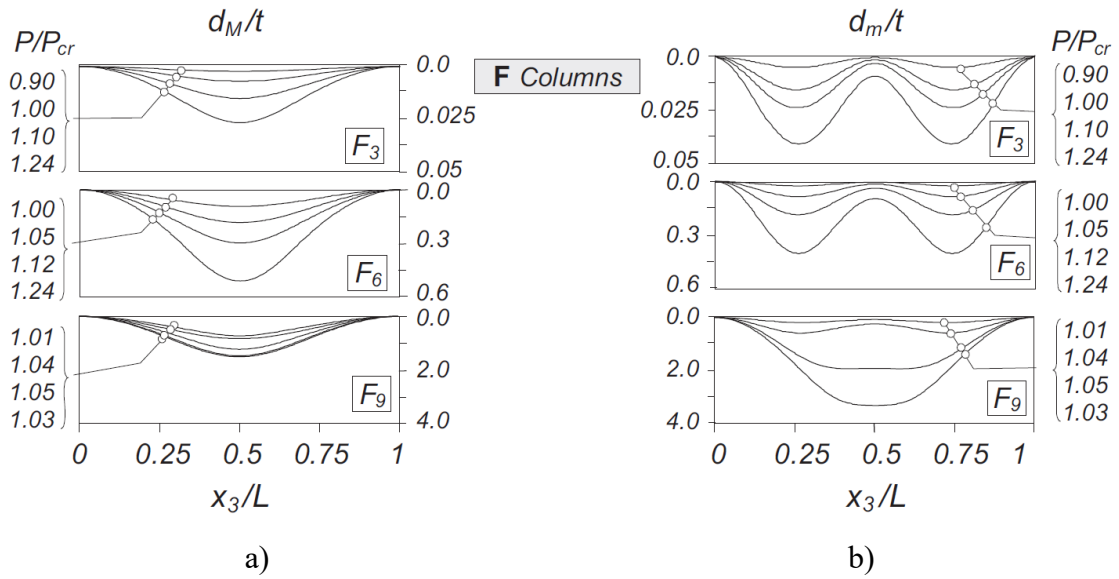


Figure 22: F_3 , F_6 , and F_9 columns a) P/P_{cr} vs. d_M/t and a) P/P_{cr} vs. d_m/t longitudinal profiles [31].

1.3.6 Fixed-ended equal-leg angle columns elastic-plastic post-buckling behaviour and strength

Dinis *et al.* [34] also investigated the elastic-plastic behaviour and strength characteristics of fixed-ended short-to-intermediate angle columns. Their findings include two columns, F_3 and F_9 , with four different yield-to-critical stress ratios ($\sigma_y/\sigma_{cr} \approx 1.3, 2.5, 5.0$, where $\sigma_y = 30, 60, 120 \text{ N/mm}^2$ and $\sigma_{cr} = 24 \text{ N/mm}^2$). It is essential to highlight that $\sigma_y/\sigma_{cr} \approx \infty$ corresponds to the elastic post-buckling behaviour (Section 1.3.5).

Figure 23(a) and Figure 24(a) show the upper portions of the elastic-plastic equilibrium paths (P/P_{cr} vs. β) for the shorter and longer fixed-ended columns (F_3), respectively, where ($P/P_{cr} > 0.5$). Additionally, in Figure 23(b) and Figure 24(b), there are three plastic strain diagrams, each corresponding to equilibrium states along the $\sigma_y/\sigma_{cr} = 2.5$ equilibrium path, illustrating the collapse mechanism of the columns. Considering the results, the following comments deserve to be highlighted:

- i) The shorter column (F_3) reveals that $\sigma_y/\sigma_{cr} \approx 1.3$ and 2.5 fail at the point of yielding, while the one with $\sigma_y/\sigma_{cr} \approx 5.0$ shows a minimal elastic-plastic strength reserve. Additionally, the column's ultimate load increases with σ_y . Considering $\sigma_y = 30$ to 120 N/mm^2 approximately doubles the load-carrying capacity. The plastic strain diagram I in Figure 23(b) shows yielding initiates in the quarter and three-quarter-span regions of the corner's longitudinal edge, where the shear and longitudinal normal stresses are elevated due to variations in torsional rotation;
- ii) The longer column (F_9) reveals that the ultimate strength is nearly unaffected by σ_y because geometrically nonlinear factors mainly drive collapse. Specifically, for $\sigma_y/\sigma_{cr} \approx 2.5$ and 5.0 , the column remains elastic until failure, with yielding starting well into the descending branch of the equilibrium path. This onset of yielding occurs in the middle of the vertical leg mid-span region, as depicted in Figure 24(b) (diagram II).

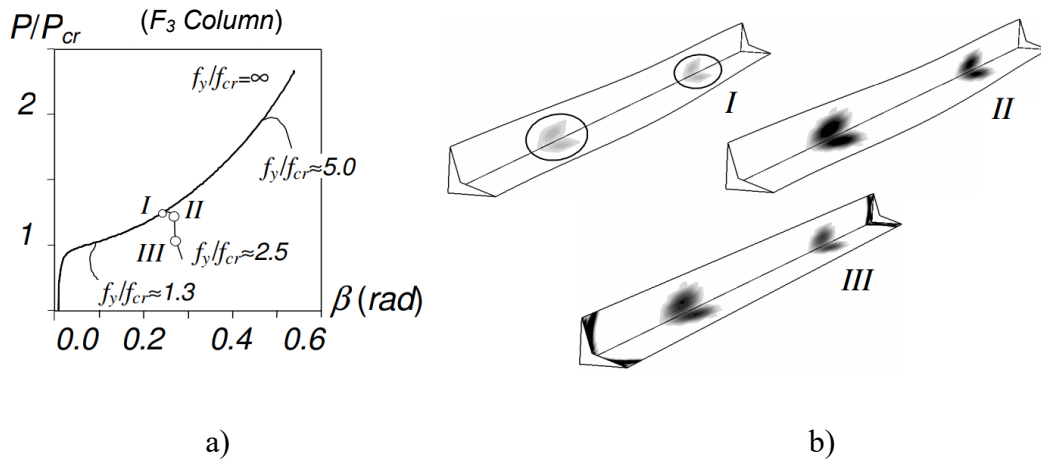


Figure 23: F_3 column elastic-plastic post-buckling behaviour a) P/P_{cr} vs. β equilibrium paths, for $\sigma_y/\sigma_{cr} \approx 1.3, 2.5, 5.0$ and b) plastic strain diagrams and failure mechanism, for $\sigma_y/\sigma_{cr} \approx 2.5$ [34].

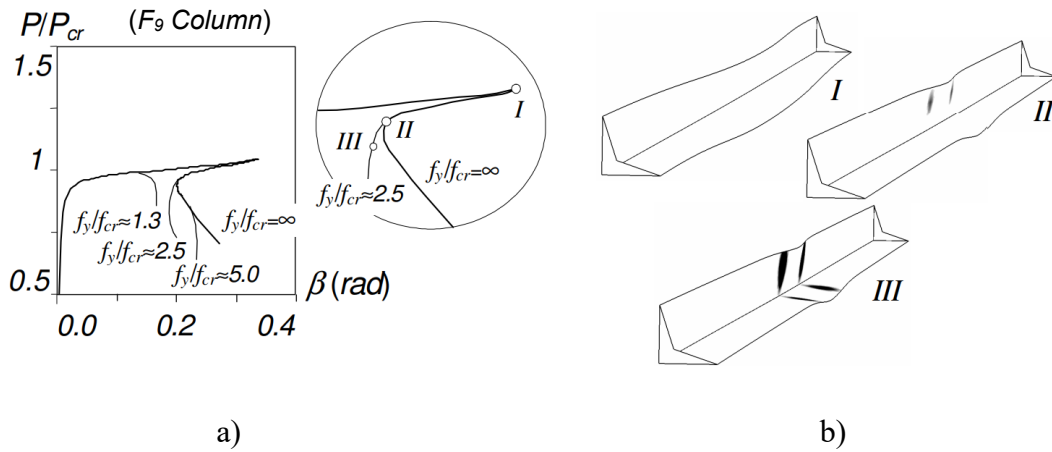


Figure 24: F_9 column elastic-plastic post-buckling behaviour a) P/P_{cr} vs. β equilibrium paths, for $\sigma_y/\sigma_{cr} \approx 1.3, 2.5, 5.0$ and b) plastic strain diagrams and failure mechanism, for $\sigma_y/\sigma_{cr} \approx 2.5$ [34].

1.3.7 Equal-leg angle columns with hot-rolled steel equal-leg angle sections

In 2017, Dinis *et al.* [35] conducted a numerical investigation into the (i) buckling, (ii) elastic post-buckling behaviour, and (iii) elastic-plastic and strength of short-to-intermediate columns featuring equal-leg angle hot-rolled compact sections, i.e., $b/t < 20$. Their findings revealed a behaviour closely resembling that of columns with cold-formed (slender) cross-sections.

Initially, the authors compare the columns' elastic buckling behaviour using both the compact angle section ($b/t \leq 20$) and the slender section ($b/t > 20$) concerning three boundary conditions employed in the investigation (F, PC and PS) as illustrated in Figure 25. The authors concluded that the columns' elastic buckling behaviour with compact cross-sections resembles that of slender sections. However, they noted a reduction in the flexural-torsional plateau, indicating that the transition from flexural-torsional (FT) to minor-axis flexural buckling (F_m) occurs at shorter lengths. In fixed-ended columns, the critical buckling mode switches abruptly from flexural-torsional to minor-axis flexural at the transition length ($L_{T,F}$) calculated according to Eq. (51).

$$L_{T,F} = b \sqrt{\frac{\pi^2 K_F}{6}} \quad \text{with} \quad K_F = (1 + \nu) \left[2.25 \left(\frac{b}{t} \right)^2 - 4.0 \right] \quad (51)$$

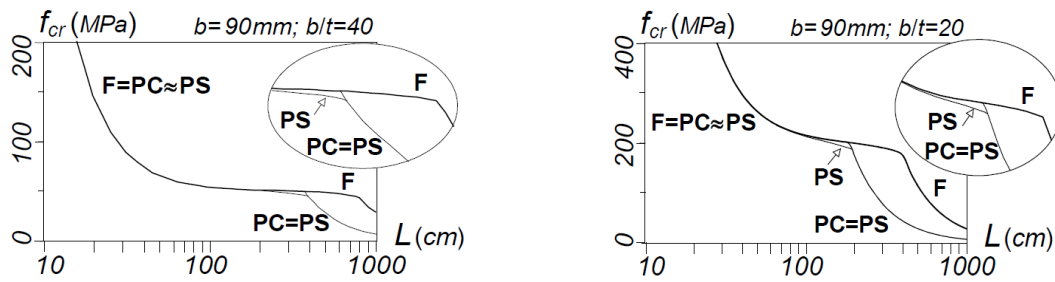


Figure 25: f_{cr} vs. L curves for F, PC, and PS columns with $b = 90$ mm and $b/t = 40$ or $b/t = 20$ [35].

Posteriorly, in Figure 26, the results concerning fixed-ended (F) short-to-intermediate columns' elastic post-buckling behaviour with $b/t = 10, 15, 20$, and 58 and lengths $L \approx 0.25L_T$, $0.50L_T$, $0.75L_T$, and $1.00L_{T,F}$, are presented in terms of the columns' mid-span equilibrium paths P/P_{cr} vs. β and P/P_{cr} vs. d_m . With these results, the following observations deserve to be highlighted:

- i) Columns with identical b/t and $L/L_{T,F}$ values demonstrate nearly identical equilibrium paths, indicating similar post-buckling behaviours. Furthermore, these behaviours are primarily unaffected by b/t and show a pronounced length-dependent interaction between major-axis flexural-torsional and minor-axis flexural buckling;
- ii) The length-dependent interaction between flexural-torsional and flexural buckling can be observed by observing the simultaneous occurrence of cross-

section torsional rotations and translations and the noticeable effect of minor-axis flexural displacements on the post-buckling strength of the column;

- iii) Two distinct behavioural patterns are identifiable: one observed in the shortest columns ($L \approx 0.25L_T$), characterized by minimal translations and associated with relatively small post-critical strength changes, and the other observed in the remaining columns ($L/L_{T,F} = 0.5$ to 1.0), involving significant translations and associated with clearly defined limit points. Notably, in F columns, such limit points are only evident for $L/L_{T,F} \geq 0.75$.

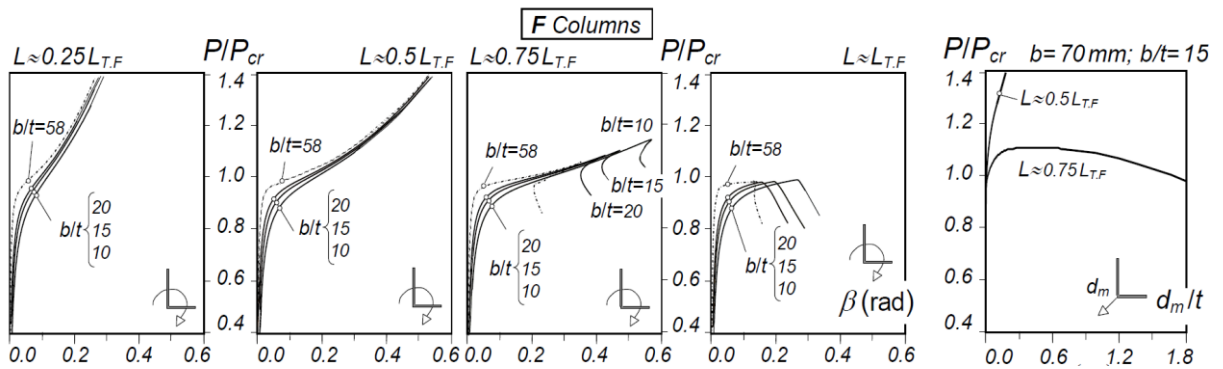


Figure 26: Fixed-ended columns' elastic equilibrium paths P/P_{cr} vs. β and P/P_{cr} vs. d_m/t with $L/L_T \approx 0.25, 0.50, 0.75, 1.00$.

1.4 Structural behaviour of short-to-intermediate cruciform columns

1.4.1 Introduction

Unlike equal-leg angle sections, the cruciform section benefits from cross-section double symmetry, featuring a coincident centroid and shear centre. This characteristic ensures the absence of corner flexural displacements, resulting in each of the four legs behaving identically. Hence, understanding the buckling, post-buckling behaviour, and resistance of columns with cruciform cross-sections is essential to extrapolating knowledge to the equal-leg angle starred columns', as illustrated in Figure 27.

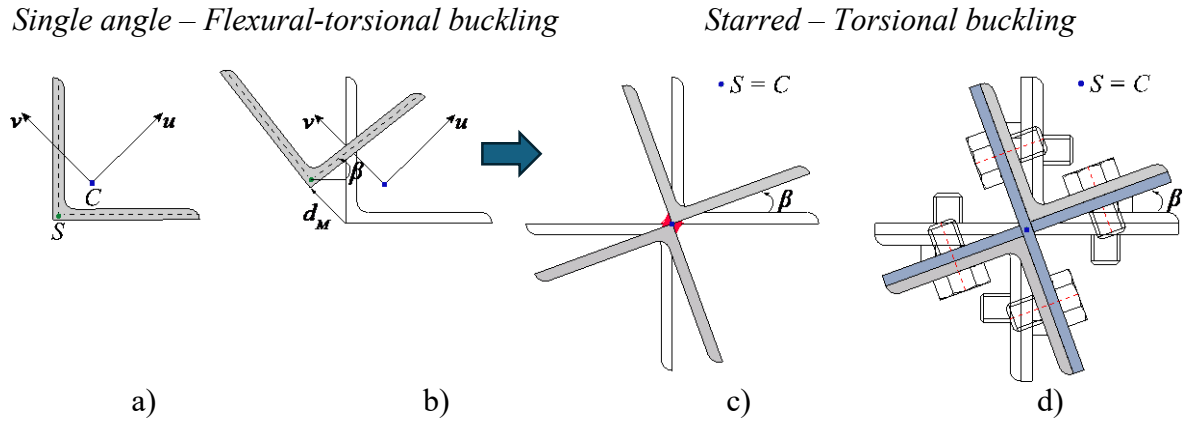


Figure 27: a) Equal-leg angle cross-section, b) flexural-torsional buckling, c) welded starred torsional buckling and d) bolted starred torsional buckling.

1.4.2 Elastic buckling behaviour

Dinis *et al.* [30] and Dinis and Camotim [36] also conducted a numerical investigation using GBT and shell finite element analyses (through ABAQUS [33]) to investigate the elastic buckling behaviour of steel fixed and pinned short-to-intermediate cruciform columns. The authors adopted a cruciform section with typical dimensions ($b = 80$ mm and $t = 4$ mm) and steel material behaviour ($E = 210000$ MPa and $\nu = 0.3$).

Figure 28(a) shows the “signature” curve in a logarithmic scale – P_{cr} vs. L – obtained from GBT analyses for both fixed (F) and pinned (P) cruciform columns. These analyses encompass eight deformation modes, comprising three global modes (2, 3, and 4) and five local modes (5-9). In Figure 28(b), the GBT modal participation diagram is depicted, while Figure 28 (c) showcases the buckling mode shapes of the pinned (P) columns with lengths of 20 cm, 200 cm, and 1000 cm. Based on these results, it is possible to conclude that:

- i) The GBT and ABAQUS results show almost perfect agreement for pinned and fixed columns. These consistencies entail (i₁) the critical load P_{cr} decreasing with increasing L , always indicating single half-wave buckling ($m=1$), (i₂) they exhibit the typical approximately “horizontal plateaus”, and (i₃) the pivotal role of the torsion mode 4, contributing to the critical buckling modes of all columns except the very long ones;
- ii) Across the entire length spectrum, the critical buckling modes of all pinned and fixed columns encompass just three deformation modes (2/3, 4, and 6). For very

short lengths, the buckling mode combines local-torsional modes (4+6), with mode 4 contributing dominantly. Short-to-intermediate columns buckle primarily in pure torsional modes (4), while the longer ones buckle in pure minor-axis flexural mode (3);

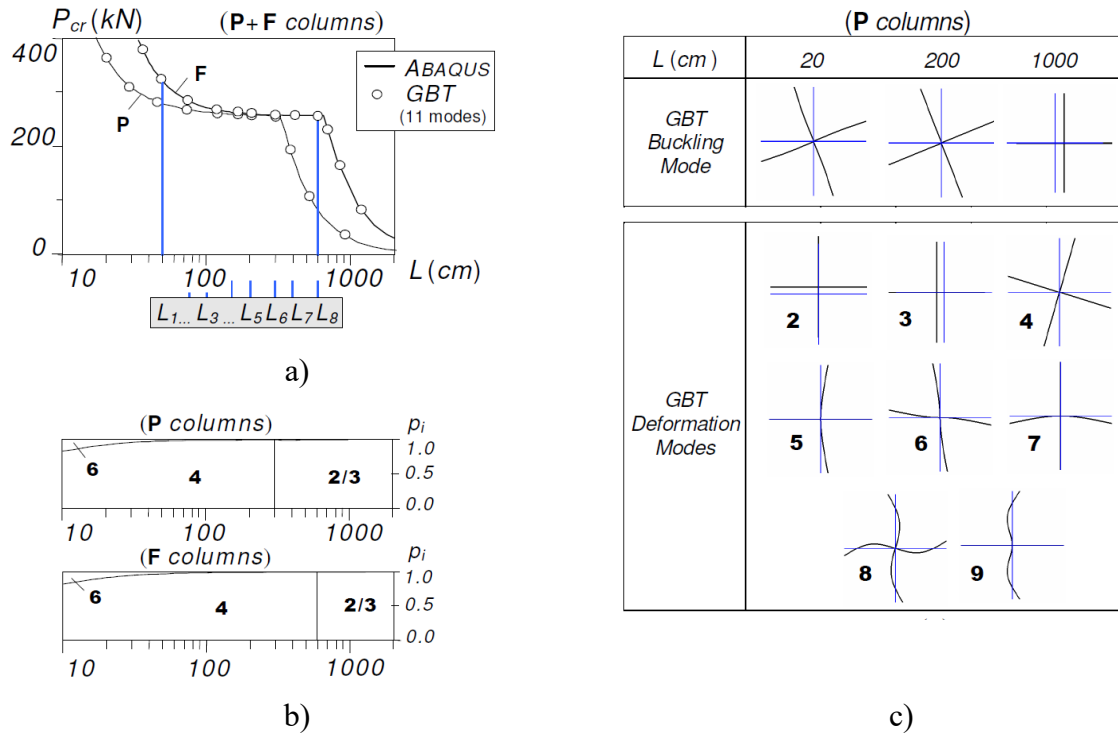


Figure 28: Pinned and fixed column a) P_{cr} vs. L curves, b) GBT modal participation diagrams, and c) 3 pinned column buckling modes and 8 GBT deformations mode shapes [36].

1.4.3 Fixed-ended elastic post-buckling behaviour

The authors [36] also employed a numerical finite element analysis in ABAQUS [33] to investigate the elastic post-buckling response of fixed-ended columns of short to intermediate lengths, i.e., L_3 – L_8 , as illustrated in Figure 28(a). This investigation included the incorporation of initial geometrical imperfections in the critical mode, set at an amplitude of $0.1t$, which specifically involves torsional deformations at the mid-span cross-section, quantified by $\beta_0 = 0.005$ rad. Figure 29(a) shows the upper portion of the post-buckling equilibrium paths for fixed-ended columns, covering lengths L_3 – L_8 , and displays the deformed mid-span cross-

section configuration at $\beta = 0.4$ rad the column L_7 . Based on these results, it is possible to conclude that:

- i) The post-buckling behaviour of short-to-intermediate fixed-ended cruciform columns is evidently stable, revealing high post-critical strength. However, post-critical stiffness reduces as the column's length increases. Additionally, these behaviours are characterized exclusively by rigid-body rotations of the cross-section, without any displacements of the cross-section's shear centre, as illustrated by the deformed configurations of the mid-span cross-sections in column L_7 .
- ii) Moreover, the authors demonstrated that the fixed-ended cruciform columns behave precisely as (ii₁) fixed-ended equal-leg angle columns with the corners' displacements (major and minor axes) constrained or (ii₂) a plate of identical dimensions, as shown in Figure 29(b). This underscores that the characteristic behaviour of angle sections with equal-leg angles is attributed to displacements (bending) occurring at the section's corners, a phenomenon extensively discussed in their studies [31][34][35].

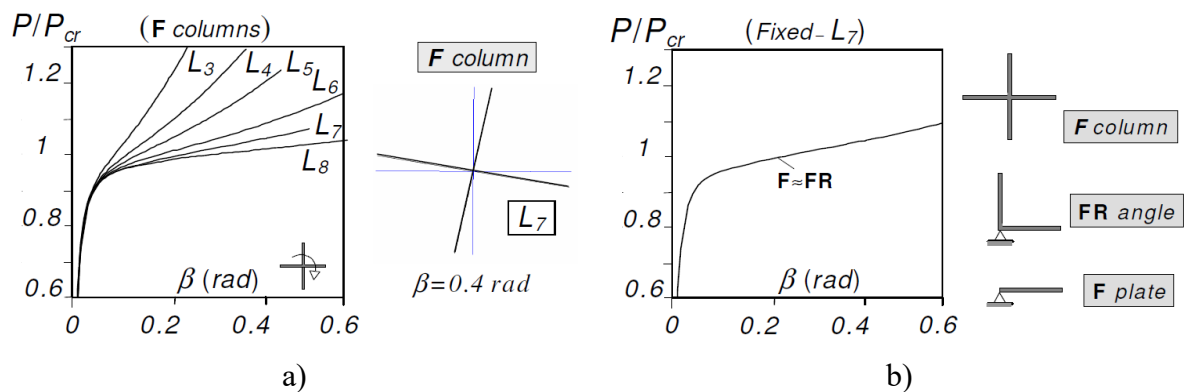


Figure 29: a) Fixed P/P_{cr} vs. β column equilibrium paths and L_7 column mid-span cross-section deformed configurations and b) P/P_{cr} vs. β equilibrium paths for F plate, FR angle and L_7 column [36].

1.4.4 Fixed-ended elastic-plastic post-buckling behaviour and strength

In the continuation of their study, the authors investigated the elastic-plastic post-buckling behaviour and strength concerning six different yield-to-critical stress ratios ($\sigma_y/\sigma_{cr} \approx$

1.2, 1.8, 2.6, 4.0, 6.0, and 9.0. These ratios correspond to yield strengths $\sigma_y = 235, 355, 520, 800, 1200, \text{ and } 1800 \text{ MPa}$ and critical stress $\sigma_{cr} = 201 \text{ MPa}$. The main observations can be made:

- i) Initially, it is observed that the majority of fixed columns, with the exception of those having notably low yield stress, demonstrate (i₁) a significant reserve of elastic-plastic strength (evidenced by load increase post-yielding), (i₂) a substantial level of ductility before failure;
- ii) As illustrated in Figure 30(c) in diagram I, the yield occurs primarily near the quarter and three-quarter span zones along the central longitudinal edge of the column. This behaviour is explained by the longitudinal normal and shear stresses reaching their peak due to the derivative of torsional rotation;
- iii) The collapse is characterized by the extensive yielding across most of the column's volume, as depicted in diagram II of Figure 30(c), with only the areas immediately adjacent to the end and mid-span cross-sections maintaining their elasticity upon failure.

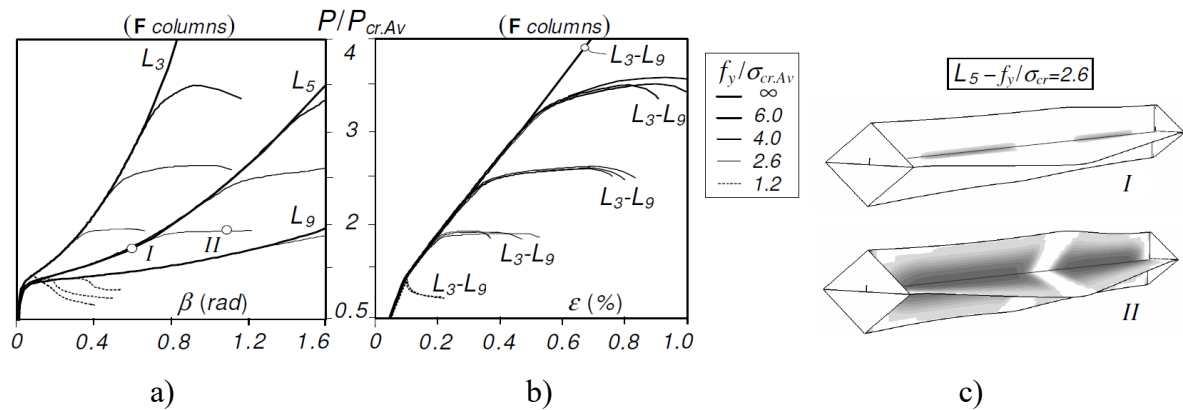


Figure 30: F_3, F_5, F_9 column a) $P/P_{cr,Av}$ vs. β and b) $P/P_{cr,Av}$ vs. ϵ paths ($5 \sigma_y/\sigma_{cr}$), and c) deformed configuration and plastic strain evolution ($L_5 + \sigma_y/\sigma_{cr} \approx 2.6$) [36].

1.5 Fixed-ended equal-leg angle and starred columns' ultimate strength and design

1.5.1 Carbon steel material

In 2013, Silvestre et al. [37], followed by Dinis and Camotim [38] in 2015, undertook a comprehensive evaluation of the design curves for fixed-ended short-to-intermediate carbon

steel cold-formed equal-leg angle columns through experimental tests and numerical analyses, focused on the flexural-torsional buckling plateau. Considering the unique columns' structural behaviour, the objective was to improve the accuracy and reliability of failure load predictions.

This significant contribution introduced new design approaches for equal-leg angle columns based on the Direct Strength Method (DSM) [39]. This method provides more accurate predictions by directly considering the columns' elastic buckling modes. The authors proposed to change the single local buckling curve to a comprehensive set of columns' buckling curves, meticulously derived from their observations concerning post-buckling behaviour involving the simultaneous occurrence of cross-section torsional rotations and flexural (corner) displacements, which significantly influence the post-critical strength reserve.

This approach leads to more accurate predictions of ultimate strength, ensuring safer and more efficient design practices for such structural elements. This advancement in the field offered a more rational basis for the design of equal-leg angle columns. It paved the way for future research to refine the design and analysis of structural components subjected to buckling. It is essential to highlight that the same process was carried out for hot-rolled equal-leg angle columns [35].

Sirqueira *et al.* [40] conducted an experimental and numerical investigation into the fixed-ended carbon steel hot-rolled equal-leg and the behaviour of hot-rolled carbon steel equal-leg angle sections under compression, focusing on the flexural-torsional buckling failure mode. Through experimental campaigns and a numerical finite element model, the study confirmed the conservatism of the Eurocode 3: Part 1.1 [5], highlighting the more accurate performance of the modified Direct Strength Method (mDSM) developed by [35].

1.5.2 Stainless steel material

In 2013, Reynolds [41] aimed to evaluate the stainless steel design codes, specifically Eurocode 3: Part 1.4 [4], by conducting 33 experimental tests on columns made from welded duplex stainless steel S32003 angle sections under centred compression. Reynolds concluded that the non-linear behaviour of the material becomes more pronounced for shorter column lengths, both in terms of ultimate load and deformation. It was also demonstrated that at such lengths, the columns were more prone to flexural-torsional buckling phenomena, especially with higher b/t ratios. The tests indicated that the design rules of Eurocode 3: Part 1.4 [4] do

not accurately reflect the columns' behaviour, either predicting the ultimate limit state incorrectly or being overly conservative.

In 2017, Menezes *et al.* [42] also aimed to gain a deeper understanding of fixed-ended columns' behaviour featuring hot-rolled equal-leg angle cross-section $L64 \times 64 \times 6.4$ made of austenitic stainless steel 304. This investigation was conducted through eleven experimental tests at the Civil Engineering Laboratory (LEC) of the State University of Rio de Janeiro (UERJ), examining columns of six different lengths ranging from 500 mm to 1500 mm. The findings indicated that columns shorter than 750 mm predominantly failed due to flexural-torsional buckling, while those of greater lengths exhibited minor-axis flexural buckling as the primary failure mode. Additionally, the study assessed the applicability of the design standard provisions outlined in Eurocode 3: Part 1-4 [4], concluding that these provisions did not offer an accurate design for these columns.

In 2018, Liang *et al.* [43] conducted 16 tests on fixed-end columns with hot-rolled equal-flange compact stainless steel angles using two types of stainless steel – EN 1.4307 and EN 1.4571 – which correspond to austenitic stainless steel 304L and austenitic stainless steel 316, respectively, according to European nomenclature. Two cross-sections were adopted, $L80 \times 80 \times 10$ and $L100 \times 100 \times 10$, with four tests conducted for each section and steel type, varying the length. The authors assessed the current design criteria for stainless steels and also the new methodology based on the Direct Strength Method, concluding that the proposal based on the Direct Strength Method, although developed for carbon steel columns, can predict a more coherent ultimate load for stainless steel columns than European standard design.

In 2020, Sirqueira *et al.* [44] at LEC/UERJ conducted eighteen tests to investigate the ultimate strength of fixed-ended austenitic stainless steel 304 hot-rolled equal-leg angle columns. Three cross-sections were used, namely $L64 \times 64 \times 4.8$, $L76 \times 76 \times 6.4$, and $L102 \times 102 \times 6.4$, with lengths ranging from 152 to 1893 mm. According to the authors, it was concluded that for the three assessed sections, at lengths shorter than 500 mm, flexural-torsional buckling occurred. For the $L64 \times 64 \times 4.8$ section with lengths between 500 mm and 1000 mm, flexural-torsional buckling was observed, and above these lengths, bending buckling occurred in the minor axis. For the $L76 \times 76 \times 6.4$ section with lengths between 500 mm and 1200 mm, failure due to flexural-torsional was observed, and above these, buckling occurred due to bending in the minor axis. For the $L102 \times 102 \times 6.4$ section with lengths between 500 mm and 1500 mm, flexural-torsional buckling was observed, and above these lengths, bending buckling occurred in the minor axis.

In 2020, Sarquis *et al.* [45] conducted a comprehensive experimental and numerical investigation into the flexural-torsional buckling behaviour of fixed-ended hot-rolled austenitic stainless steel 304 columns. The experimental phase encompassed four main activities: selecting the cross-sections and lengths of the columns through elastic buckling analysis; prototypes' initial geometrical imperfections measurements, including local (cross-section rotation) and global (bending along the major and minor axes) imperfections; stainless steels' material characterization based on compressive and tensile responses; and conducting ten tests to identify the failure modes, establish the equilibrium paths, and obtain the columns' ultimate strength. Concurrently, a numerical study was performed with a finite element model validated against the experimental data, thereby extending the findings to additional cross-sections and column lengths prone to failure by flexural-torsional buckling. This study also evaluated two design methods: the standard provisions for stainless steel materials in Eurocode 3: part 1.4 [4] and a design procedure based on the direct strength method by Dinis *et al.* [35] for carbon steel materials. Both methods were found to be inadequate for predicting the ultimate loads of the columns, prompting the proposal of two new design procedures adapted from the Eurocode 3: Part 1.4 [4] approach. These two proposed design methods yielded more reliable outcomes, particularly when the design of fixed-ended austenitic stainless steel hot-rolled equal-leg angle columns.

In 2020, Dobrić *et al.* [46] conducted axial load tests on cold-formed stainless steel angle columns, identifying unique behavioural patterns under axial loads that are crucial for accurate modelling and design. The following year, Filipović *et al.* [47] expanded this research to hot-rolled stainless steel angle columns, providing essential data through experimental tests. Concurrently, another study by Filipović *et al.* [48] delved into the performance of laser-welded stainless steel angle columns, revealing that these connections could enhance structural capabilities, opening up new avenues for construction applications. Furthermore, in 2021, Dobrić *et al.* [49] proposed new design procedures for cold-formed stainless steel equal-leg angle columns, achieving improvements in structural behaviour prediction. Collectively, these studies from 2020 and 2021 have made pivotal contributions to the structural engineering field, offering deeper insights into the design and application of stainless steel angle columns across different manufacturing and connection techniques. These findings not only augment the existing body of knowledge but also provide practical guidance for safer and more efficient construction practices involving stainless steel angle columns.

These series of studies underscore the need for an updated approach in the European code to accurately reflect the actual behaviour of stainless steel short-to-intermediate equal-leg

angle columns. The gathered research highlight significant gaps in the Eurocode 3: Part 1.4 [4]. The results indicate that the standard design approach is not only scattered and conservative for stainless steel short-to-intermediate equal-leg angle columns, but the cross-section classification and column buckling curve “*b*” used to estimate the flexural-torsional buckling resistance is unable to predict the drop in columns’ ultimate strength. In other words, a change in the methodology used by the European code is necessary to improve the accuracy of forecasting resistance according to the actual columns’ structural behaviour.

For this purpose, Botelho *et al.* [50] conducted an experimental campaign considering hot-rolled equal-leg angle section $L63.50 \times 4.76$ ($b/t = 13.34$) to evaluate the structural response of these types of starred columns’ assembly procedure (welded and bolted – as illustrated in Figure 27(c) and (d)). The study focused on austenitic stainless steel fixed-ended short-to-intermediate starred columns prone to failure by torsional buckling to assess these columns’ torsional buckling ultimate strength. The findings revealed significant discrepancies in the ultimate strength of the columns between the experimental results and the predictions from the European code.

2 STAINLESS STEEL COLUMNS' DESIGN – EUROCODE 3: PART 1.4 (EC3)

2.1 Introduction

Design standards evaluate structures by identifying limit states, representing conditions beyond which the structure no longer meets its design requirements. Three categories of limit states are identified: ultimate, serviceability, and durability. For ultimate limit states, the following relationship must be satisfied: $S_d \leq R_d$, i.e., the design action effect value due to the load applied (S_d) must be less or equal to the members' design resistance value (R_d).

Members under uniform axial compression (i.e., columns) are susceptible to several forms of failure, including (i) cross-section yielding, (ii) local buckling, (iii) global buckling – (iii₁) minor-axis flexural buckling, (iii₂) torsional buckling, and (iii₃) flexural-torsional buckling – and (iv) interaction between local-global buckling. For instance, local buckling may reduce the effective area of the cross-section that contributes to load-bearing capacity, consequently decreasing the critical load necessary to initiate global buckling. Likewise, the emergence of global buckling can introduce extra stresses, worsening local buckling conditions.

Thus, the European code design guidelines check the columns' buckling ultimate limit state from the (i) cross-section classification, (ii) cross-section resistance, and (iii) member buckling resistance. Therefore, this section shows the European standard design rules procedures for structural austenitic and duplex stainless steel columns prone to failure by torsional buckling – Eurocode 3: Part 1.4 (EN 1993-1-4) [4].

2.2 Cross-section classification and resistance

The European steel design code establishes that cross-section evaluations must be conducted independently of the global analysis. This analysis is crucial for ensuring that elements subjected to full or partial compression are thoroughly assessed for their susceptibility to local buckling (which reduces the member resistance). Consequently, the code guidance on classifying cross-sections emerges as a critical component of the members' design process, and the section's susceptibility to local buckling is assessed through four distinct rotational

capacities behaviours, categorised into class 1, 2, 3, or 4 – as illustrated in Figure 31. This methodology leads to the classification of cross-sections by comparing the maximum slenderness ratio of the component plates (b/t) with a non-dimensional parameter related to the materials' mechanical properties $\varepsilon = [(235/\sigma_{0.2\%})/(E/210000)]^{0.5}$.

Specifically, class 1 cross-sections are designed to achieve the plastic moment of resistance (M_{pl}) and accommodate significant deformations beyond the elastic limit, allowing for the application of plastic hinges in designs (internal force redistribution). Class 2 cross-sections also reach the plastic moment of resistance but have a limited capacity for inelastic deformation before encountering local buckling. Meanwhile, class 3 cross-sections, being more slender, can only reach the elastic moment (M_{el}). Class 4 cross-sections are extremely slender plates elements that undergo local buckling before achieving the theoretical elastic moment. Employing these cross-sections classified as class 4 necessitates adherence to the additional stipulations outlined in Eurocode 3: Part 1.5 [51], ensuring a thorough and comprehensive approach to steel structure design.

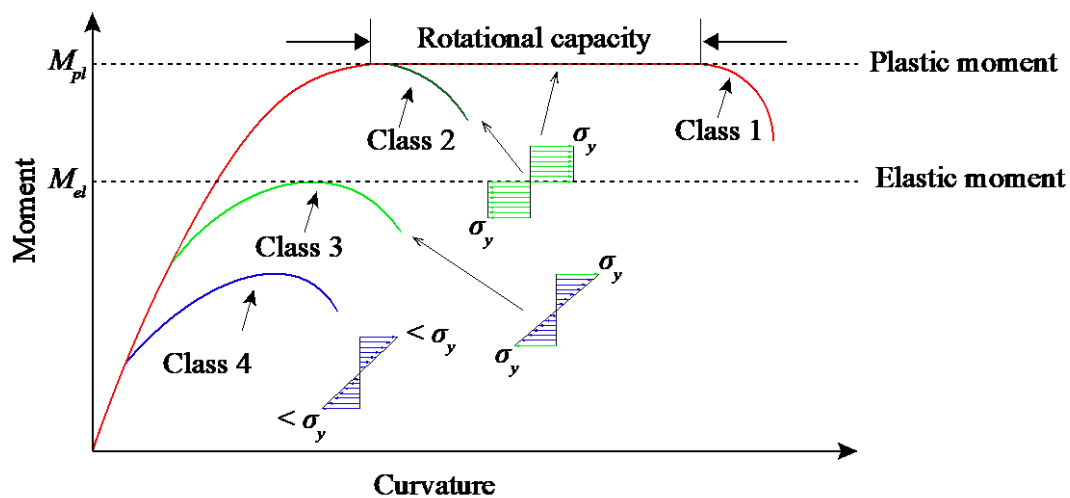


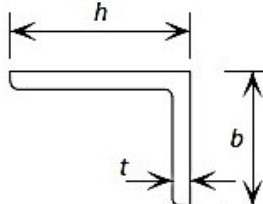
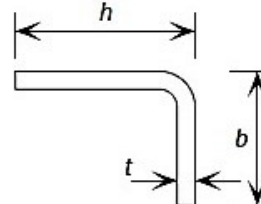
Figure 31: Eurocode 3 categorizes cross-sections into four distinct behavioural classes.

However, as specified in Eurocode 3: Part 1.4 [4] within Table 5.2, an equal-leg angle cross-section can only be classified as either class 3 or 4 – shown in Table 3. Therefore, the properties of a class 4 cross-section ($b/t > 11.5\varepsilon$) are determined by reducing the gross cross-section area (A_g) according to the Effective Width Method (EWM). The concept adopted in this method transforms a non-uniform stress distribution diagram into a uniform one, as illustrated in Figure 32. It is assumed that the stress distribution becomes uniform across the fictitious effective width “ b_{eff} ” with a value equal to the edge stresses, i.e., neglecting a part of the

section's width that fails to reach the yield stress (ineffective areas). By applying this reduction factor (ρ), the effective width (b_{eff}) is assessed and multiplied by the element thickness (t) to determine the effective area (A_{eff}).

For calculating the effective width (b_{eff}), EC3 employs a parameter which correlates the internal normal stresses ratio in the cross-sections' element (ψ) with the plate buckling coefficient (k_σ), as shown in Table 4 for outstanding elements in compression. Therefore, it becomes evident that, in scenarios concerning columns (i.e., uniform compression $\sigma_2/\sigma_1 = 1$), the buckling coefficient value is $k_\sigma = 0.43$. Subsequently, the reduction factor (ρ) for outstanding elements in compression can be determined based on the element's slenderness (λ_p), using the Winter-type curve developed by George Winter in 1947 [52] through a semi-empirical approach, as expressed in Eqs. (52) and (53), respectively.

Table 3: Angle section maximum width-to-thickness ratio for compression parts [4].

Angles				
Refers also to Outstand flanges			Does not apply to angles in continuous contact with other components.	
				
Class	Section in compression			
3	$\frac{h}{t} \leq 15,0\varepsilon ; \frac{b+h}{2t} \leq 11,5\varepsilon$			
$\varepsilon = \left[\frac{235}{\sigma_{0,2\%}} \frac{E}{210000} \right]^{0,5}$	Grade	1.4301	1.4401	1.4462
	$\sigma_{0,2\%}$ (N/mm ²)	210	220	460
	ε	1,03	1,01	0,689

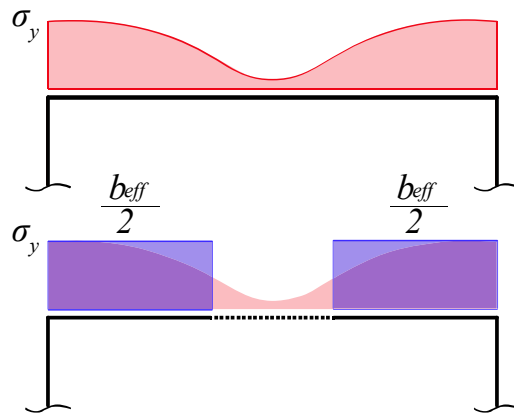
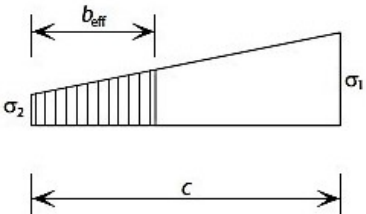
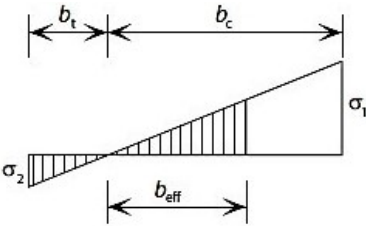


Figure 32: The concept of the Effective Width Method for cross-section class 4 – transforming non-uniform stress distribution into a uniform one.

Table 4: Effective width of outstand compression elements [51].

Stress distribution		Effective width b_{eff}		
		$1 > \psi > 0$ $b_{eff} = \rho c$		
		$\psi < 0$ $b_{eff} = \rho b = \rho c / (1 - \psi)$		
$\psi = \sigma_2 / \sigma_1$	1	0	-1	$+1 \geq \psi \geq -3$
Buckling factor k_σ	0,43	0,57	0,85	$0,57 - 0,21\psi + 0,07\psi^2$

$$\lambda_p = \frac{b/t}{28.4\epsilon\sqrt{k_\sigma}} \quad (52)$$

$$\rho = \frac{1}{\lambda_p} - \frac{0.188}{\lambda_p^2} \leq 1.0 \quad (53)$$

2.3 Columns buckling design curves

The design evaluations for stainless steel axial compression members [4] closely resemble those for carbon steel counterparts [5]. The adopted European multiple buckling curves indexed as “ a_0 ”, “ a ”, “ b ”, “ c ”, and “ d ”, find their roots in comprehensive studies by the European Convention for Constructional Steelwork (ECCS), including pivotal experimental research by Stinfresco [53] and Jacquet [54], alongside theoretical contributions from Beer and Schultz [55].

Each curve, from “ a_0 ” to “ d ”, is developed to reflect buckling behaviours in assessing steel structural members’ stability. The “Ayrton-Perry” [56] equation plays a crucial role in calculating the column reduction factor (χ) by utilizing the relevant buckling curve, defined by the non-dimensional slenderness limit ($\lambda_0 = 0.2$) and corresponding imperfection factor ($\alpha = 0.13, 0.21, 0.34, 0.49$ and 0.76 , respectively), as shown in Figure 33(a). This strategy allows for a specific approach to various steel grades and cross-section shapes, as presented in Table 6.2 in Eurocode 3: Part 1.1 [5].

As one progresses from curve “ a_0 ” to curve “ d ”, there is a notable transition towards members with a lower inherent strength. This gradation signifies an increasing risk of buckling, necessitating careful consideration in the design procedure to ensure structural integrity. When comparing the buckling curve “ a_0 ” with curve “ d ” across identical non-dimensional slenderness values, a notable discrepancy in the reduction factor emerges, with curve “ a_0 ” presenting a higher factor, thus predicting a greater ultimate strength. For example, with a non-dimensional slenderness (λ) of 0.8, the reduction factors are $\chi_{a_0} = 0.85$ and $\chi_d = 0.58$, respectively, marking a substantial difference of 31.76% in the resistance forecast. On the other hand, it is also possible to observe that as the non-dimensional slenderness increases, this difference significantly diminishes.

However, the columns’ torsional buckling resistance – the main aim of this work – is determined employing column buckling curve “ b ”, defined by the non-dimensional slenderness limit ($\lambda_0 = 0.2$) and the imperfection factor ($\alpha = 0.34$), as shown in Figure 33(b). Therefore, the columns’ buckling resistance obtained by Eurocode 3: Part 1.4 [4] ($P_{u,EC3}$) is assessed according to Eqs. (54)-(57), where: A is equal to the A_g for class 3 or A_{eff} for class 4 cross-section; $\sigma_{0.2\%}$ is the stainless steel proof stress; χ_T is the column reduction factor determined from the buckling curve “ b ”; λ_T is the non-dimensional torsional slenderness calculated by Eq. (57) – $A\sigma_{0.2\%}$ is the

cross-section resistance (A_g or A_{eff}) and $P_{cr,T}$ is the elastic critical torsional buckling load defined in Eq. (1).

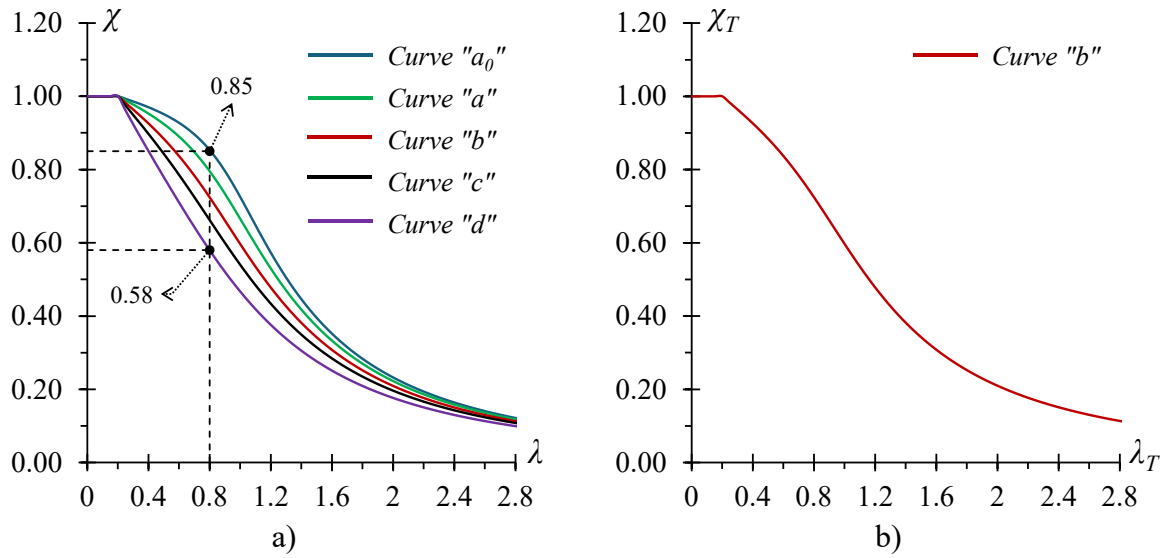


Figure 33: Eurocode 3: Part 1.1 a) multiple column buckling curves [5] and b) curve “b”.

$$P_{u,EC3} = \chi_T A \sigma_{0.2\%} \quad (54)$$

$$\chi_T = \frac{1}{\phi + [\phi^2 - \lambda_T^2]^{0.5}} \leq 1 \quad (55)$$

$$\phi = 0.5 [1 + \alpha (\lambda_T - \lambda_0) + \lambda_T^2] \quad (56)$$

$$\lambda_T = \sqrt{\frac{A \sigma_{0.2\%}}{P_{cr,T}}} \quad (57)$$

3 STAINLESS STEEL FIXED-ENDED STARRED COLUMNS EXPERIMENTAL RESULTS

3.1 Introduction

Botelho *et al.* [50] conducted an experimental campaign to evaluate the structural response of short-to-intermediate austenitic stainless steel columns with fixed ends created by two equal-leg angles cross-sections $L63.50 \times 4.76$ forming a starred section, i.e., prone to failure by torsional buckling.

This experimental programme may be briefly summarised in the following sequences of steps: assembly procedure of dual equal-leg angle starred cross-sections with two different connections approaches, including the use of two directions bolted plates and the application of fillet welding, both positioned at distances corresponding to one-third ($1/3$) and two-thirds ($2/3$) of the columns' length (L); material characterisation through tensile and compression tests aimed at determining the mechanical properties of the stainless steel; columns' initial geometrical imperfections measurements to map the prototypes' primary maximum amplitude; compression tests were performed to evaluate columns' ultimate load, load versus axial shortening curves, mid-span load versus transverse displacements, and failure modes. The entire experimental programme can be seen in detail in [50].

Therefore, this section aims to provide significant details (which will be used in the numerical study presented in the following sections) regarding the experimental (i) columns' assembly procedure, (ii) instrumentation setup, and (iii) the results obtained, i.e., (iii₁) columns' ultimate load, (iii₂) equilibrium paths, and (iii₃) failure mode.

3.2 Welded and bolted starred columns' assembly procedure of Botelho *et al.* [50]

The welded starred columns (denoted as WSC) were assembled by connecting the corners of two austenitic equal-leg angle profiles $L63.50 \times 4.76$, which have a longitudinal (y) length of 700 mm, using four stainless steel welds. These welds were strategically positioned

at one-third and two-thirds of the column's total length (L), employing a fillet weld with a leg length matching the thickness (t) of the angle profile, as shown in Figure 34.

The assembly procedure for the bolted starred columns (denoted as BSC) entailed the connection of the same equal-leg angle profiles (austenitic stainless steel, cross-section dimensions of $L63.50 \times 4.76$, and longitudinal length equal to 700 mm). The configuration of the BSC was established by implementing two bolted connections, each positioned at specific longitudinal (y) locations placed at one-third ($1/3$) and at two-thirds ($2/3$) of the column's length (L) through two bolts and a connection plate in the z and x transversal directions, respectively, as shown in Figure 35(a).

The connections employed ASTM A490 structural hexagonal steel bolts having a minimum ultimate tensile strength ($f_{u,b}$) of 1034.21 MPa with a $1/2"$ diameter (i.e., $d_b = 12.70$ mm) for easy gripping and ensuring a tight and secure fit – offering strength and reliability. Also, the plate connections were carefully designed with specific dimensions, i.e., the plate's height, width, and thickness ($h_p = b - 3t$, $w_p = 2b + t$, and $t_p = t$) were determined based on the equal-leg angle cross-section profile selected ($b = 63.50$ and $t = 4.76$ mm).

Figure 35(b) provides a visual illustration highlighting the section of the equal-leg angle profile cut to manufacture the connection plates. Furthermore, Figure 35(c) presents the dimensions of the designed plates measuring $131.76 \times 49.22 \times 4.76$ mm and showing the position of two holes made in the plate with a diameter (d_p) of 14 mm to fit the selected bolts for the connection ($d_b = 12.70$ mm). It is crucial to emphasise that this assembly approach ensures two pivotal aspects: (i) the plate used in the connection has the same stainless steel mechanical properties as the equal-leg angle profiles used to create the starred columns, and (ii) this technique simplifies the column's assembly procedure in practice – standardising the connection plate according to the equal-leg angle cross-section selected.

After setting the geometry with the welds and bolted connection components, the next step was to include (through dot welds) robust square plates with a thickness of 30 mm at the column's prototype top and bottom – ensuring that the centroid of the prototype aligns precisely with the thick plates' centroids. This experimental methodology ensures the column's uniform distribution of normal stress and effectively restrains torsion and secondary warping at the supports. For instance, Figure 36 presents the prototypes of two bolted starred columns to conduct the tests.

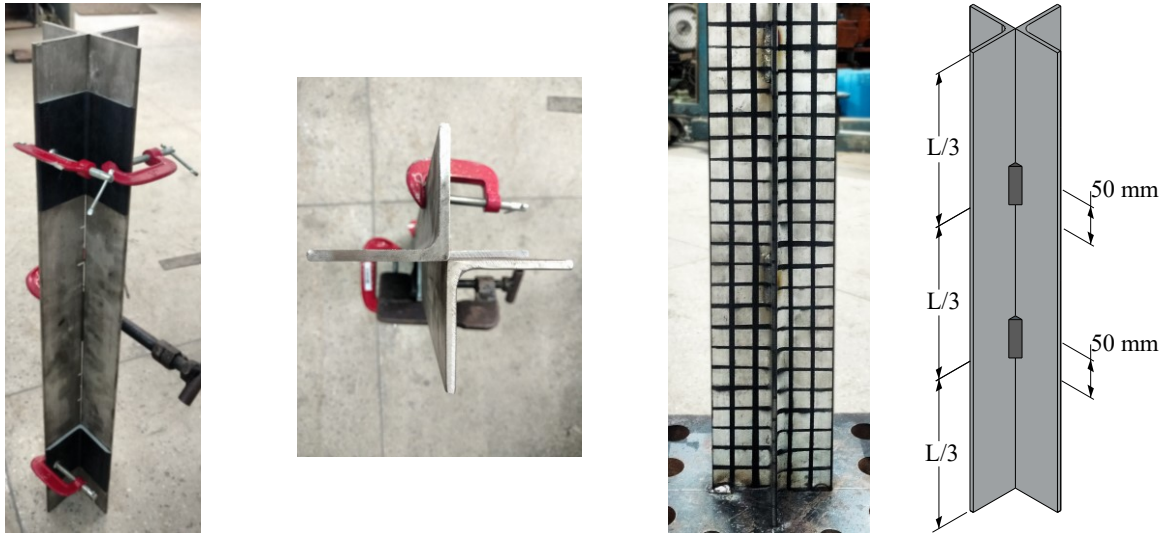


Figure 34: Column's layout procedure to create a welded starred cross-section [50].

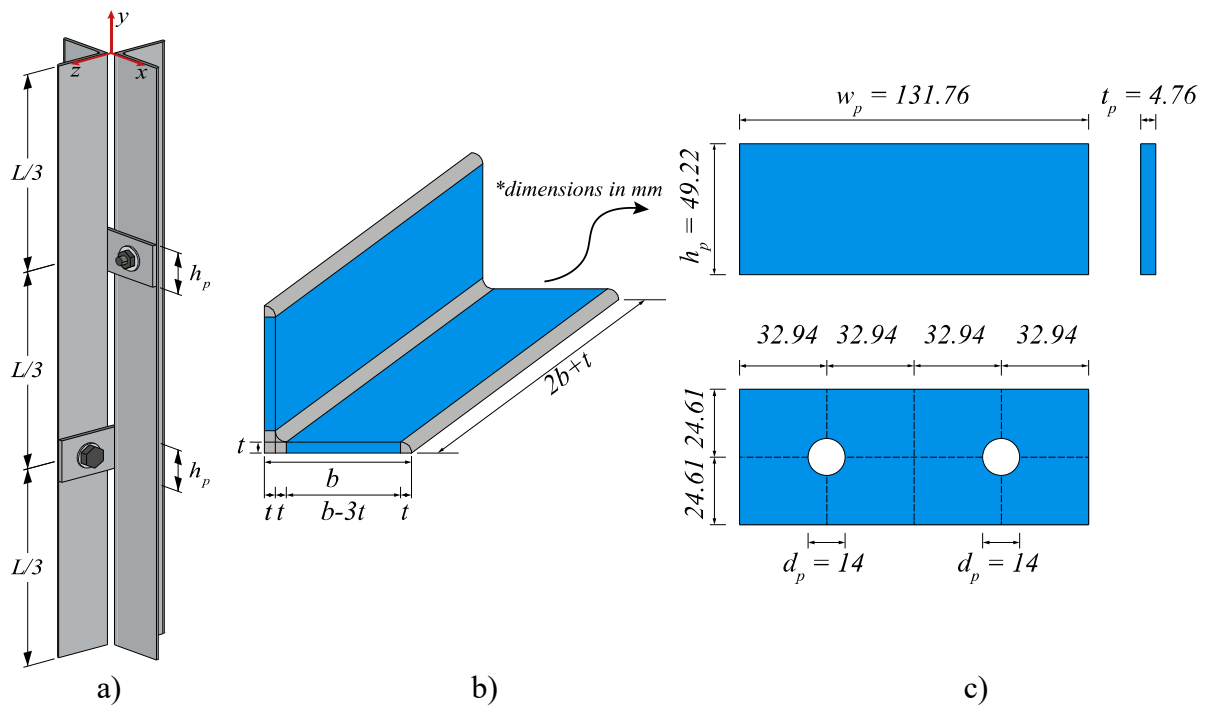


Figure 35: Equal-leg angle bolted starred column, b) section cut from the equal-leg angle profile to produce the connection plates, and c) designed plate dimensions for experimental bolted connection.

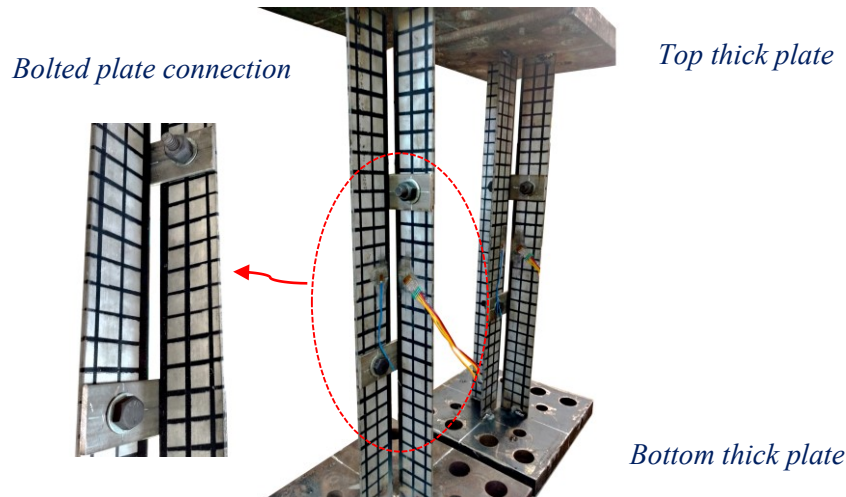


Figure 36: Bolted starred columns experimental prototypes [50].

3.3 Experimental setup and instrumentation

The specimens were placed in the Universal Lousenhausenwerk test machine so that the centroid of the column was precisely aligned with the centroids of the top and bottom plates of the load application system. It is essential to note that this test machine allows only longitudinal displacement (Δ_y) of the bottom plate, thus establishing fully fixed-ended support conditions.

The instrumentation setup was achieved using 10 Linear Variable Differential Transducers (LVDT) to read longitudinal and transversal displacements during the tests. Two LVDTs (V1 and V2) were vertically positioned at the press machine's bottom plate to acquire the column axial shortening (Δ_y). Furthermore, eight LVDTs were horizontally positioned 15 mm from the equal-leg angle section edge along the entire column length to obtain the starred cross-section's transversal displacements (Δ_x e Δ_z), i.e., four LVDTs (V3, V4, V9, and V10) were placed at a longitudinal distance of $L/6$ from both the columns' top and bottom ends. In contrast, the remaining four (V5, V6, V7, and V8) were positioned at the mid-length of the column ($L/2$).

It is essential to highlight that the results obtained by LVDTs V3, V4, V9 and V10 are not discussed in this work. This arrangement was developed to comprehensively understand the columns' behaviour during the tests, i.e., (i) axial shortening and (ii) mid-span cross-section torsional rotation equilibrium paths. Figure 37(a) shows an overview of the tests' setup, and Figure 37(b) highlights the mid-span cross-section's instrumentation.

Finally, during the test procedure, an initial preload of 20 kN, i.e., a minute compressive load, was applied to eliminate any potential gaps between the machine's end support and the specimens. After the load application, a displacement control strategy was used with a loading rate consistently maintained at 0.003 mm/s until the end of the tests. This approach provides a more controlled and precise means of assessing the column's behaviour under increasing loads, allowing for a detailed analysis of its structural response.

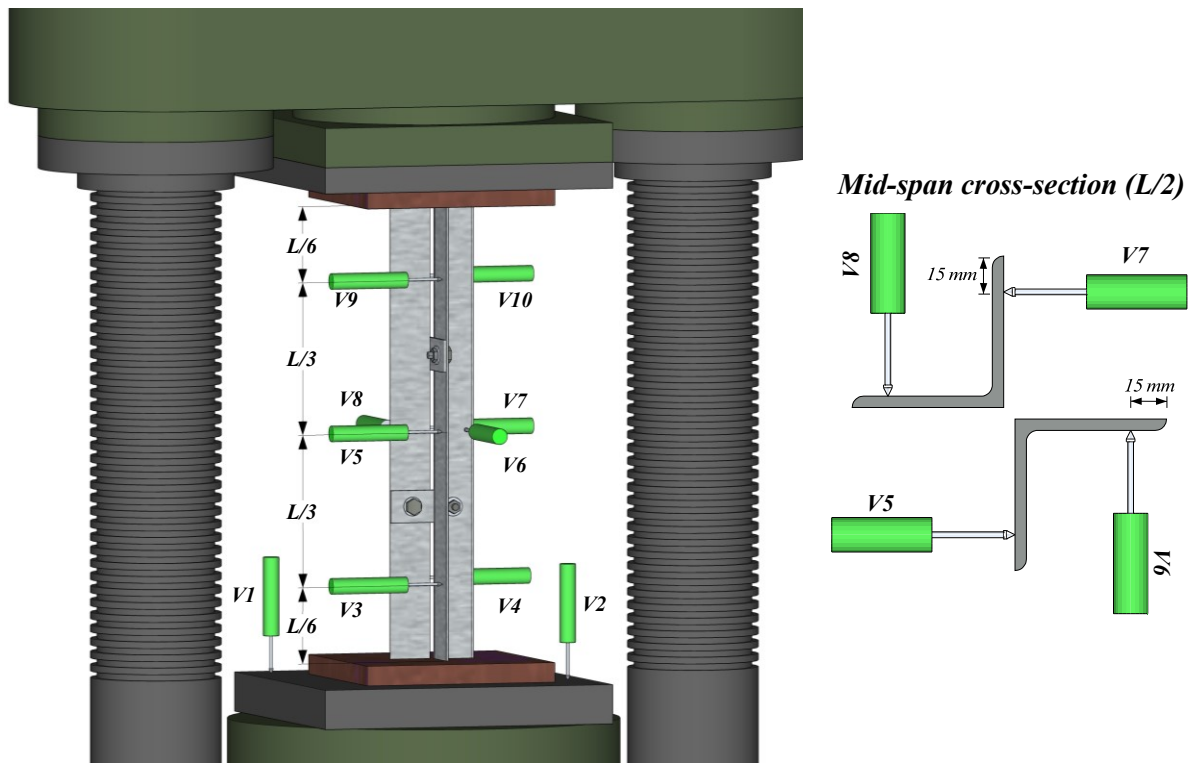


Figure 37: An overview of the experimental layout with a) displacement transducer position and b) mid-span cross-section ($L/2$) instrumentation.

3.4 Experimental results

This section provides an overview of the experimental results obtained from austenitic stainless steel fixed-end welded and bolted starred columns tests, including (i) columns' ultimate load ($P_{u,exp}$), (ii) load versus axial shortening curves (P vs Δ_y), (iii) mid-span load versus transverse displacements (P vs Δ_x and P vs Δ_z), as well as the observed failure mode. Table 5

briefly provides the experimental ultimate loads and failure modes of the conducted tests, outlined by test repetition indexes A and B.

Table 5: WSC and BSC experimental ultimate load and failure mode.

<i>Test</i>	<i>P_{u,exp}</i> (kN)	<i>Failure mode</i>
WSC 63.5x4.76 – A	640.40	Torsional buckling
WSC 63.5x4.76 – B	652.44	Torsional buckling
BSC 63.5x4.76 – A	680.08	Torsional buckling
BSC 63.5x4.76 – B	608.26	Torsional buckling

3.4.1 Welded starred columns

Figure 38 displays for WSC the equilibrium paths obtained from the experimental tests regarding the load and axial shortening (P vs Δ_y) curves and five deformed shapes developed throughout test A. Additionally, Figure 39 depicts the columns' mid-span ($L/2$) load versus transverse displacements (P vs Δ_x and P vs Δ_z). The observation of these experimental results prompts the following observations:

- i) The equilibrium paths for welded starred columns (WSC) indicate a high degree of similarity, with ultimate loads of 640.40 kN and 652.44 kN, showing a minimal variation of about 2%. This consistency underscores the repeatability of the tests, which align on a common deformation mode predominantly characterized by torsional rotation, as evidenced by a single sinusoidal half-wave ($m = 1$) across the column's effective length;
- ii) Essentially, (ii₁) the columns' axial shortening equilibrium paths reveal uniform trends and a failure mode characterized by a pronounced pure torsional rotation at the mid-span cross-section, i.e., torsional buckling. However, (ii₂) a slight variation in post-buckling response was observed, with test B showing greater flexibility;
- iii) Figure 38 presents the WSC–A's failure mode evolution as a clearly defined shape with rigid-body torsional rotation at the mid-span cross-section. As the applied load approaches the ultimate load (at points “a” and “b”), the

deformation gradually intensifies until failure is reached (point “c”), followed by a significant increase in torsional deformation at points “d” and “e”;

- iv) Additionally, Figure 39(a) showcases the relationship between the experimental applied load and its transverse displacement at mid-span ($L/2$), highlighting the typical cross-section deformation by torsional rotation. Specifically, all four mid-span LVDTs (V5, V6, V7, and V8) recorded similar measurements in opposite transverse directions (x and z) during the test. For example, upon reaching the column’s ultimate failure load ($P = 640.40$ kN), the LVDT readings were $V5 = +4.10$ mm and $V7 = -4.84$ mm in the x direction, while $V6 = -4.22$ mm and $V8 = +4.43$ mm in the z -direction. This pattern of readings suggests a consistent response among all four legs of the cross-section, i.e., torsional rigid-body movement. Figure 40(b) visualizes the motions of the cross-section’s legs, further confirming the torsional behaviour of the columns.

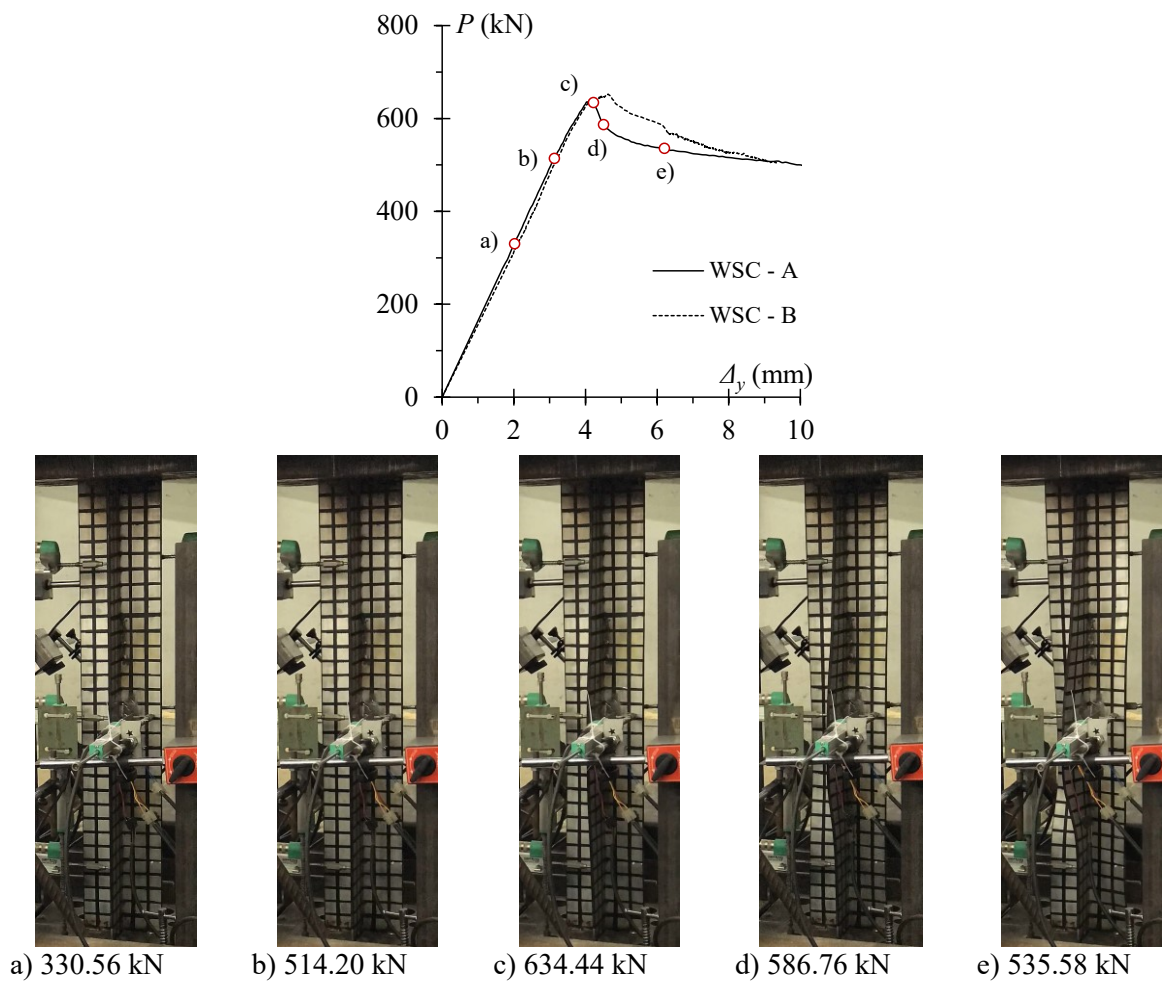


Figure 38: Welded starred column (WSC) equilibrium path – load versus axial shortening curves (P vs Δy) – and five deformed shapes throughout test A.

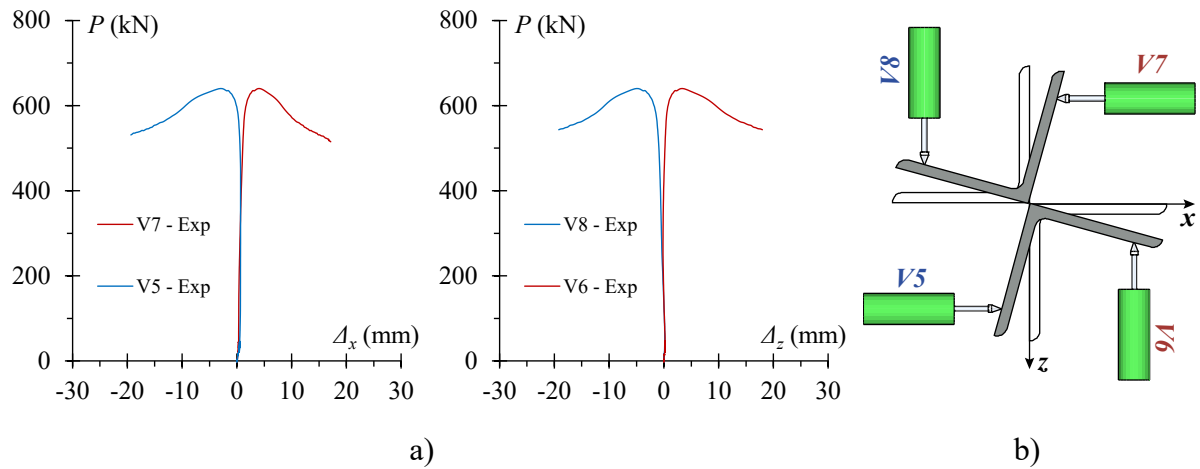


Figure 39: a) Welded starred column (WSC-A) equilibrium path – mid-span ($L/2$) load versus transverse displacements (P vs Δ_x and P vs Δ_z) – and b) the cross-section torsional rotation.

3.4.2 Bolted starred columns

Figure 40 exhibits the results of the experimental test BSC-A, presenting load versus axial shortening curves (P vs Δ_y), including four deformed shapes observed during the test – showing a closer perspective of the final deformed configuration. Additionally, Figure 41 depicts the mid-span ($L/2$) load versus transverse displacements (P vs Δ_x and P vs Δ_z). Lastly, Figure 42 shows the column's failure mode. The observation of these experimental results prompts the following observations:

- i) The experimental columns' ultimate loads display a difference of approximately 10.56%. This variation is intricately linked to the bolt-tightening procedure, as evidenced by the discernible accommodation of the column in the equilibrium path of BSC-B, leading to a subsequent decline in applied load, i.e., with possible slight slippage between the equal-leg angle and the plate used at the connection until accommodation occurs.
- ii) However, the equilibrium paths of the bolted starred columns also exhibit similar trends and failure modes, characterised by a noticeable mid-span cross-section pure torsional rotation, i.e., columns' torsional buckling failure mode. Figure 40 depicts the column's load versus axial shortening curve (P vs Δ_y) in conjunction with a visual representation of torsional buckling failure mode evolution as the

load is applied during the test. Initially, the column's deformation undergoes a gradual and nearly imperceptible deformation increase, as evident from points "a" and "b", until it reaches the column's failure load represented by point "c". After this point, a noticeable and advanced increase in cross-section torsional deformation becomes apparent due to the column's stiffness decrease, as depicted by point "d";

- iii) Additionally, Figure 41(a) also presents the column's load versus transverse displacement mid-span ($L/2$) curves, evidencing the deformed shape characterised by mid-span cross-section torsional rotation. In other words, all four LVDTs (V5, V6, V7, and V8) display comparable readings in opposing transverse directions (x and z) throughout the test. For instance, when the applied load reaches the column's ultimate failure load ($P = 680.00$ kN), the LVDTs' readings were $V5 = +3.71$ mm and $V7 = -3.74$ mm in direction x , while $V6 = -3.72$ mm and $V8 = +3.78$ mm in direction z . This reading pattern indicates rigid body movement of the cross-section as the load is applied, i.e., identical behaviour across each of the four cross-section legs (pure torsion). Figure 41(b) illustrates the torsional rotation deformed cross-section;
- iv) Figure 42 shows the final column's torsional buckling failure deformed configuration from two viewpoints. Visually, the failure mechanisms observed stem from the torsional deformation pattern observed: (iii₁) development of "plastic hinges" adjacent to the cross-sections at one and three-quarters of the column's height, (iii₂) all mid-span four legs exhibit identical behaviour, i.e., pure torsion, and (iii₃) the columns buckle in a single half-wavelength along the column's effective length;
- v) These findings indicate that the method of assembling the columns, entailing the precise positioning of bolts and plates at one-third ($1/3$) and two-thirds ($2/3$) of the column's length (L) in two transverse directions, effectively integrates the connected equal-leg angle profiles into a starred cross-section. This assembly procedure is practical and allows for straightforward disassembly if needed.

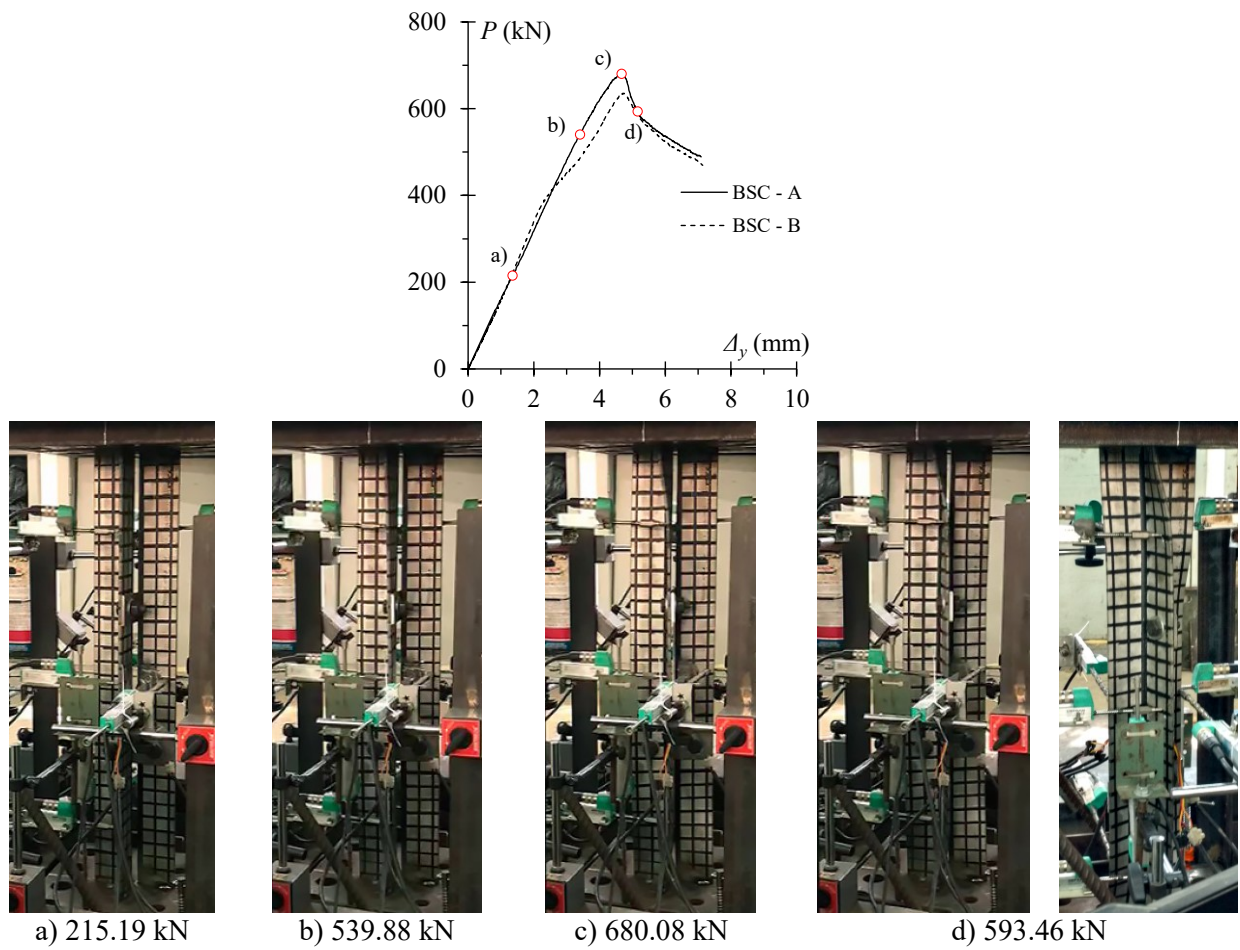


Figure 40: Bolted starred column (BSC) equilibrium path – load versus axial shortening curves (P vs Δ_y) – and four deformed shapes throughout test A.

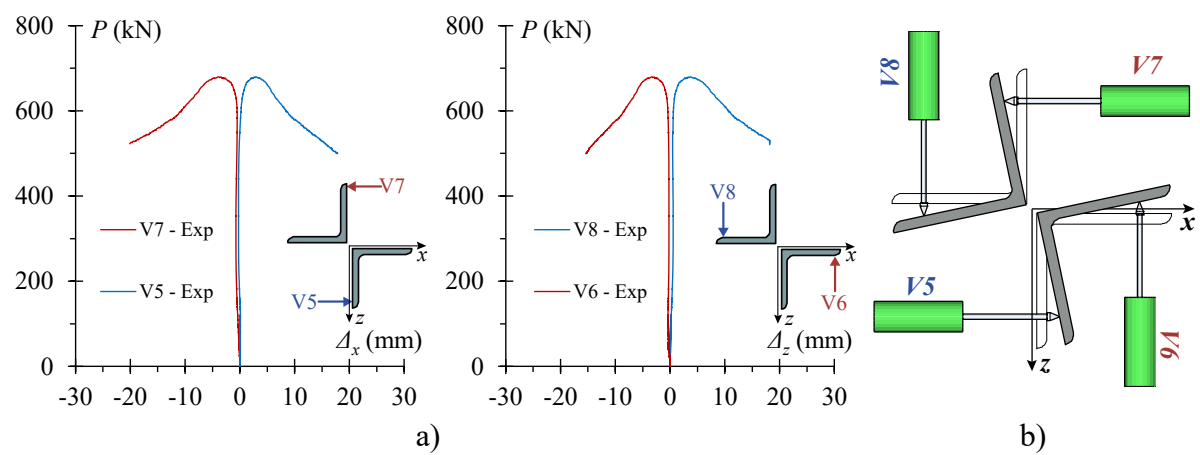


Figure 41: a) Bolted starred column (BSC-A) equilibrium path – mid-span ($L/2$) load versus transverse displacements (P vs Δ_x and P vs Δ_z) – and b) the cross-section torsional rotation.

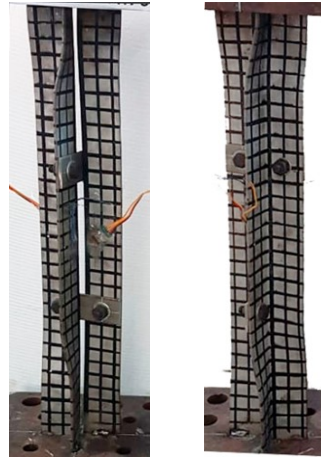


Figure 42: Bolted starred columns experimental results column's failure mode through two viewpoints.

3.4.3 Conclusions

Based on these experimental results, it is possible to obtain the following conclusions regarding austenitic stainless steel short-to-intermediate fixed-ended welded and bolted starred columns:

- i) The assembly procedure used for the columns, involving strategic placement of welds and bolts with plates at one-third and two-thirds of the column's length (L) along two transverse directions, efficiently unifies the equal-leg angle profiles into a starred cross-section (i.e., centroid and shear centre coincident), and, consequently, due to the geometry the fixed-ended short-to-intermediate columns are susceptible to pure torsional buckling failure mode – the main aim of this work;
- ii) Comparing welded and bolted starred columns reveals subtle differences in assembly and potential structural integrity. While both methods effectively create the desired starred cross-section, welded columns offer a more permanent solution with potentially greater rigidity due to the continuous nature of the welds. In contrast, bolted connections provide flexibility for disassembly, making them advantageous for applications requiring adjustability or temporary assembly;

iii) However, the susceptibility to torsional buckling suggests that regardless of the assembly method, careful consideration of the columns' geometrical properties is crucial in design and analysis to prevent early failure. However, a more extensive study is needed to encompass a broader range of fixed-ended welded and bolted starred columns and validate whether this structural behaviour is consistent across varied geometries. Hence, the objective of this study is to numerically extend these findings to gain a deeper understanding of these columns' behaviour.

4 WELDED STARRED COLUMNS ELASTIC BUCKLING BEHAVIOUR AND FINITE ELEMENT MODEL VALIDATION

4.1 Introduction

A numerical model was developed using the finite element software ANSYS 17.0 [29] to investigate the structural behaviour and ultimate strength of (austenitic and duplex) stainless steel fixed-ended short-to-intermediate welded starred columns, i.e., columns susceptible to torsional buckling failure. This section presents the particulars of the developed finite element model, including information on column geometry, element types, mesh size, boundary conditions, the implementation of initial geometrical imperfections, and the employed solution technique.

In order to comprehend the structural behaviour of the fixed-ended short-to-intermediate stainless steel welded starred columns, it is essential to conduct a preliminary investigation. Two types of structural analyses – assuming an elastic material behaviour ($E = 210$ GPa and $\nu = 0.3$) and columns geometries including a pair of compact equal-leg angle cross-sections ($b/t < 20$) – were initially conducted to gain insight into fixed-ended welded starred columns' stability.

Firstly, (i) linear buckling analysis is performed (i_1) to verify the columns assembly procedure and (i_2) to identify column lengths susceptible to torsional buckling failure as the length increases – the “signature” curve. Based on the column buckling behaviour, (ii) a non-linear elastic post-buckling analysis is performed to determine the columns' equilibrium path as the length increases, i.e., evaluating the welded starred columns' structural response regarding solely the geometrical non-linearity associated with torsional buckling failure. These analyses play a crucial role in verifying the effectiveness of the column assembly procedure across a range of column geometries – varying cross-section width (b), thickness (t), and column length (L).

Afterwards, (iii) the austenitic stainless steel behaviour is included in the finite element model, considering material non-linearity to assess the columns' strength accuracy and to validate by comparing the numerical results against the experimental results obtained by Botelho *et al.* [50]. Finally, (iv) an initial imperfection sensitivity study is conducted to assess

the impact of amplitude on the non-linear behaviour of the fixed-ended bolted starred stainless steel columns.

4.2 Solid finite element model development

All the components of the welded starred columns were discretised into SOLID185 elements – homogenous structural solid elements present in the ANSYS library [29] – defined by eight nodes having three degrees of freedom at each node: translations in the nodal directions x , y , and z . According to the software manual, this element is suitable for modelling general solid structures, even in irregular regions, such as welds. Moreover, the element has plasticity, stiffening, large displacements, and large deformations, which are capabilities necessary for instability phenomena.

Initially, the column geometry is modelled following the specifications used by Botelho *et al.* [50], which involves two equal-leg angles profiles ($2Lb \times t$) joined by a fillet weld, where the weld's leg length matches the section's thickness (t). It is strategically placed at both one-third and two-thirds of the column's length with 50 mm, as illustrated in Figure 43(a). However, the role of the columns' built-up procedure (bolted or welded) is exclusive to ensure that the pair of equal-leg angle sections are joined, working uniquely to form a starred cross-section along the entire column length, i.e., shear centre and centroid coincident. Therefore, to solve and eliminate this spacing issue between welding points in the future parametric analysis, this work employs a fillet weld continually along the column length (L), as shown in Figure 43(b).

To clarify this observation, Figure 44 presents an elastic buckling analysis that compares these two assembly procedures considering three starred column lengths $L = 700$, 1400 and 2800 mm featuring $2L63.50 \times 4.76$. For the experimentally tested column length ($L = 700$ mm), there is no difference in the column structural behaviour using weld spacing $L/3$ or continuously along the column's length. Given the relatively short length of these columns, such spacing is deemed adequate for maintaining proper structural integrity. This behaviour is also observed in columns of intermediate lengths ($L = 1400$ mm). However, for longer columns ($L = 2800$ mm, for instance), reduced spacing between weld points becomes necessary, i.e., it is crucial to add more parts of welds along the column length to guarantee the welded starred section properties.

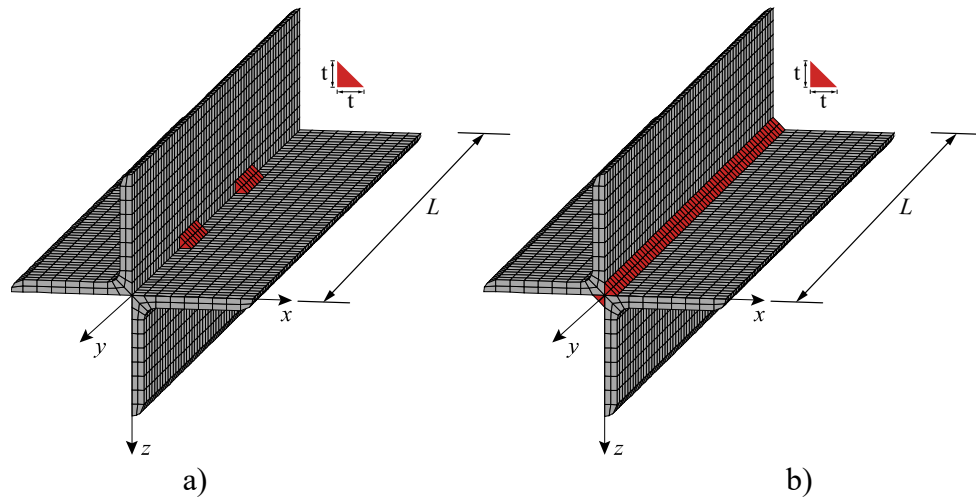


Figure 43: a) Experimental assembly procedure used in Botelho *et al.* [50] and b) finite element model assembly procedure with continuous fillet weld.

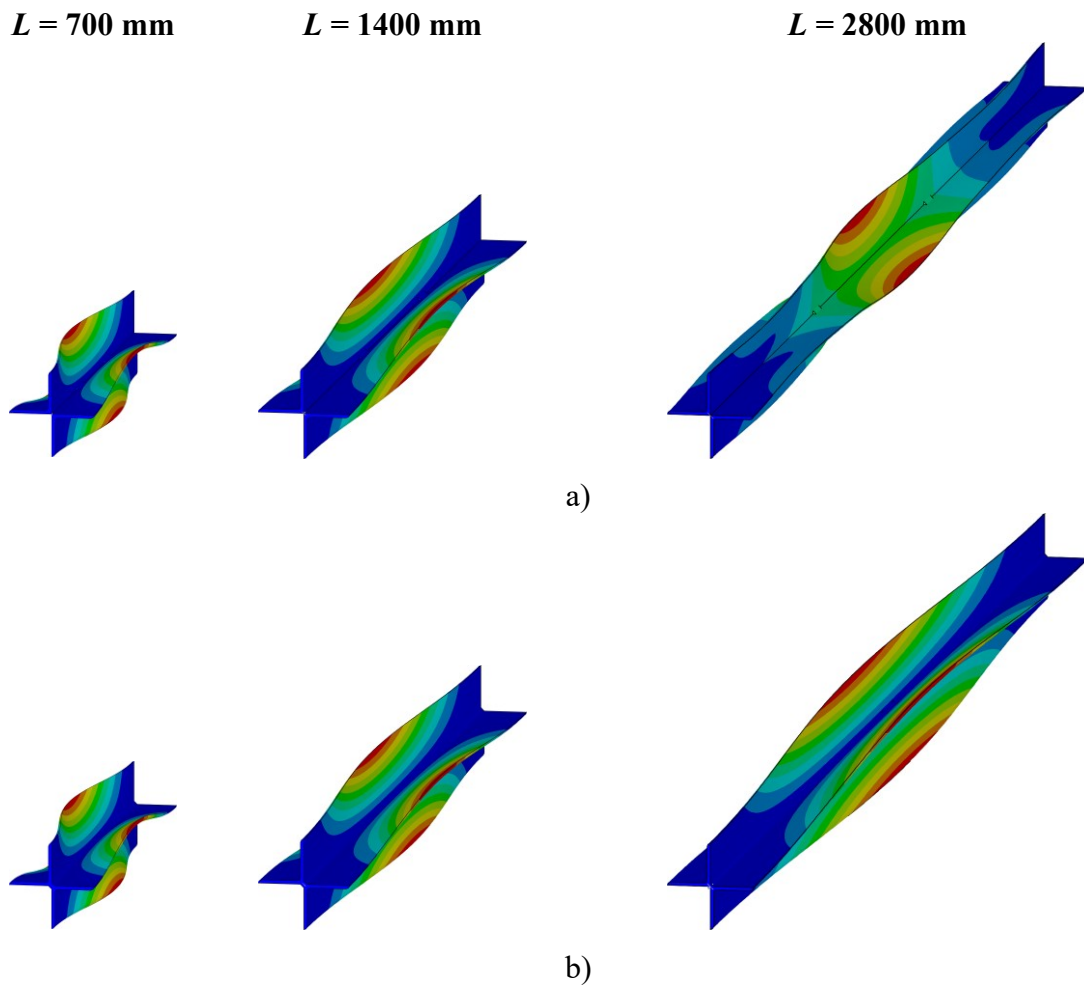


Figure 44: Starred columns' elastic buckling behaviour featuring two equal-leg angle sections 2L63.50 \times 4.76 and varying length $L = 700, 1400$ and 2800 comparison between welding a) spaced at intervals of $L/3$, and b) applied continuously along the entire length of the column.

After the geometry definition, the fixed supports are modelled by creating point elements (MASS21) having six degrees of freedom – nodal translations in x , y and z directions and rotations about the x , y , and z axes – positioned at the end sections centroid. Each end section node was rigidly connected to the point element of the respective end section (bottom and top), creating two rigid regions. So, the support condition is imposed in these point elements, restraining translation and rotation in all three directions (x , y , and z), except for the column top axial displacement (UY), which was free to move.

Column geometry, including initial geometrical imperfections, was created through a linear buckling analysis, which was performed to determine the critical buckling mode shape (eigenvector). For the investigated instability phenomena in this work, the first eigenvector (representing the critical mode) corresponds to the pure torsional buckling, characterised by a cross-section torsional rotation (β) about the longitudinal axis (y), with the maximum amplitude occurring at the cross-section located at the mid-span ($L/2$), i.e., constituting one half-wavelength. After this analysis, the “UPGEOM” command updates the ideal column geometry mesh – Figure 45(a) – to a column real mesh by including the initial geometrical imperfections vector sum with a maximum amplitude specified value. This procedure results in a mid-span ($L/2$) rigid-body rotation (β_0), i.e., each of the four legs works together, as presented in Figure 45(b) with an amplified scale.

The analysis methodology encompassed several key steps: (i) the definition of fixed-ended equal-leg angle welded starred column mesh, (ii) performing a linear buckling analysis, (iii) introduction of initial geometrical imperfection by updating the column geometry to include the torsional buckling mode, (iv) uniform compression loading was applied using by imposing a prescribed displacement (UY) at the centroid of the column’s top end, and (v) a non-linear solution strategy was employed using an incremental-iterative approach based on the full Newton-Raphson algorithm. This comprehensive methodology accounted for both material and geometrical non-linearities. Finally, a mesh convergence investigation revealed that an 8 mm x 8 mm element size could provide a real correlation between numerical and experimental behaviour, requiring a fair computational effort.

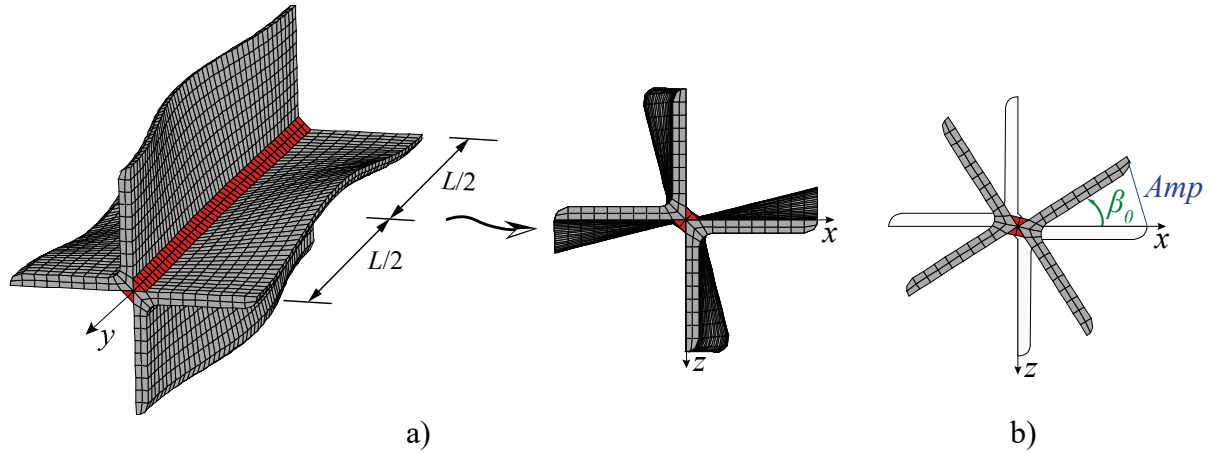


Figure 45: a) Welded starred column geometry with initial geometrical imperfection and b) mid-span ($L/2$) cross-section torsional rotation.

4.3 Column buckling behaviour

The first step was to employ the finite element model to investigate the linear stability of fixed-ended welded starred columns to obtain the cross-section “signature” curve (P_{cr} vs. L), i.e., understanding the structural element’s elastic buckling behaviour as the column length increases.

Figure 46(a) shows the variation of the elastic critical buckling load (P_{cr}) obtained by ANSYS with the column length (L) – in logarithmic scale – for columns with fixed ends created by a pair of welded equal-leg angles cross-section $L63.50 \times 4.76$ ($b/t = 13.34$) and $L88.90 \times 4.76$ ($b/t = 18.68$), respectively. These elastic buckling results lead to the following comments:

- i) According to the plate classical theory [10],[15] and also verified by Dinis *et al.* [30] using the Generalized Beam Theory (GBT) [16], it is established that local buckling (or plate buckling) occurs in a structural element if its signature curve has a local minimum and the buckling mode exhibits multiple half-waves – only possible if the plate bends transversally. In a practical range ($L \geq 30$ cm), it is noted that the fixed-ended welded starred columns’ signature curve shows (i₁) no cross-section plate bending during the buckling, (i₂) all lengths always buckles in single half-wave mode along the column’s effective length, and (i₃) for that reason no local minimum exists in the signature curve. Consequently, the critical column buckling deformation mode involves two rigid body

movements depending on the column length, i.e., solely global buckling modes: pure torsion about the shear centre for short-to-intermediate columns – Figure 46(b) – or major-axis displacements about the centroid for longer lengths;

- ii) It is observed for the entire length range investigated (30 cm to 1000 cm) that the critical buckling load (P_{cr}) decreases as column length increases (L) and shows two distinct branches revealing the critical global buckling mode: (ii₁) torsional buckling approximately “plateau” for short-to-intermediate column lengths and (ii₂) minor-axis flexural buckling for long and very long lengths. It is essential to highlight that this elastic buckling behaviour is the same obtained in fixed-ended columns with plain cruciform sections [36];
- iii) Dinis *et al.* [30] underscore the critical role of considering secondary warping effects (I_{ws}) for a precise representation of the initial descending portion of the torsional buckling in the “signature” curve. Consequently, this study includes a numerical analysis in Appendix A using ANSYS [29], aiming to investigate and determine the properties of dual equal-leg angle welded starred sections;
- iv) Notably, the onset of minor-axis flexural critical buckling mode limits the torsional buckling plateau, i.e., at a given column length, the elastic critical loads are equivalent ($P_{cr,T} = P_{cr,F}$). The length at which this shift in the buckling phenomenon occurs along the columns’ signature curve is referred to as the transition length, denoted in this work for fixed-ended welded starred columns as L_{TFS} ;
- v) Moreover, with the increasing b/t ratio (13.34 up to 18.68) straightforward observations must be highlighted: (iv₁) the column length transition (L_{TFS}) increases; (iv₂) elastic critical buckling loads decrease; (iv₃) the elastic behaviour remains consistent across the varying b/t ratios for compact cross-sections, i.e., the elastic buckling behaviour in fixed-ended welded equal-leg angle columns does not alter its shape and tends to follow the same pattern. For instance, Figure 47 illustrates a column length range from $0.30L_{TFS}$ up to $0.95L_{TFS}$ (torsional plateau) considering columns created by a pair of welded equal-leg angles $2L63.50 \times 4.76$ with $L_{TFS} = 2950$ mm and $2L88.90 \times 4.76$ with $L_{TFS} = 6100$ mm;
- vi) Another pivotal consideration is ascertaining that as the column’s length extends from $0.30L_{TFS}$ up to $0.95L_{TFS}$, the relationship between elastic critical torsional and minor-axis flexural buckling (highlighted in red dotted line) exhibits a substantial high ratio ($P_{cr,F}/P_{cr,T}$) for 90% of column lengths (i.e., $L \leq 0.90L_{TFS}$).

This characteristic indicates that only a limited number of column lengths might display interaction between global modes (torsional and minor-axis flexural buckling) during the post-buckling analysis. This behaviour will be further investigated in section 4.4;

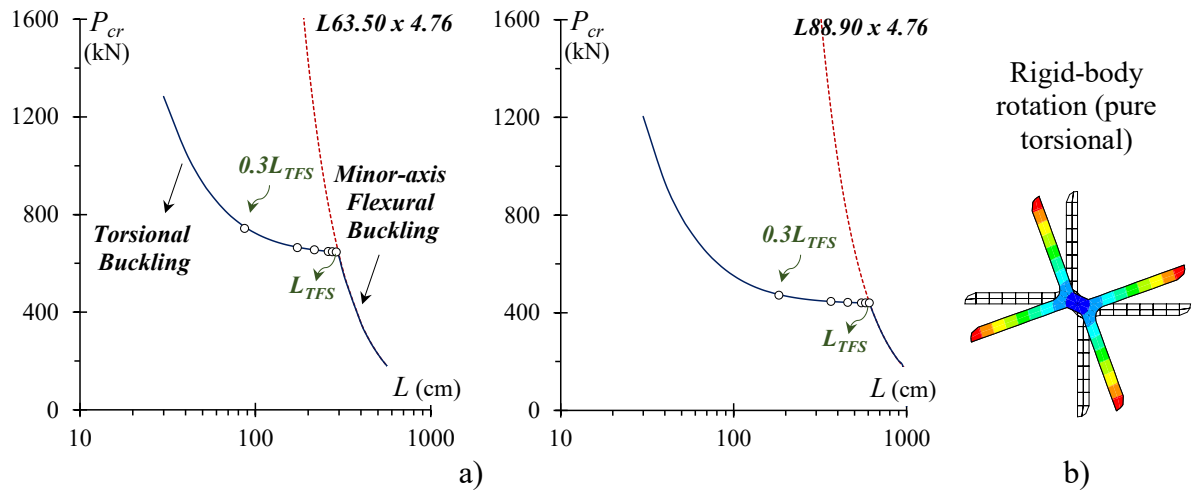


Figure 46: P_{cr} vs. L curves for columns with fixed ends created through two equal-leg angle b/t ratios of 13.34 and 18.64, respectively, and b) columns' mid-span ($L/2$) torsional buckling deformation.

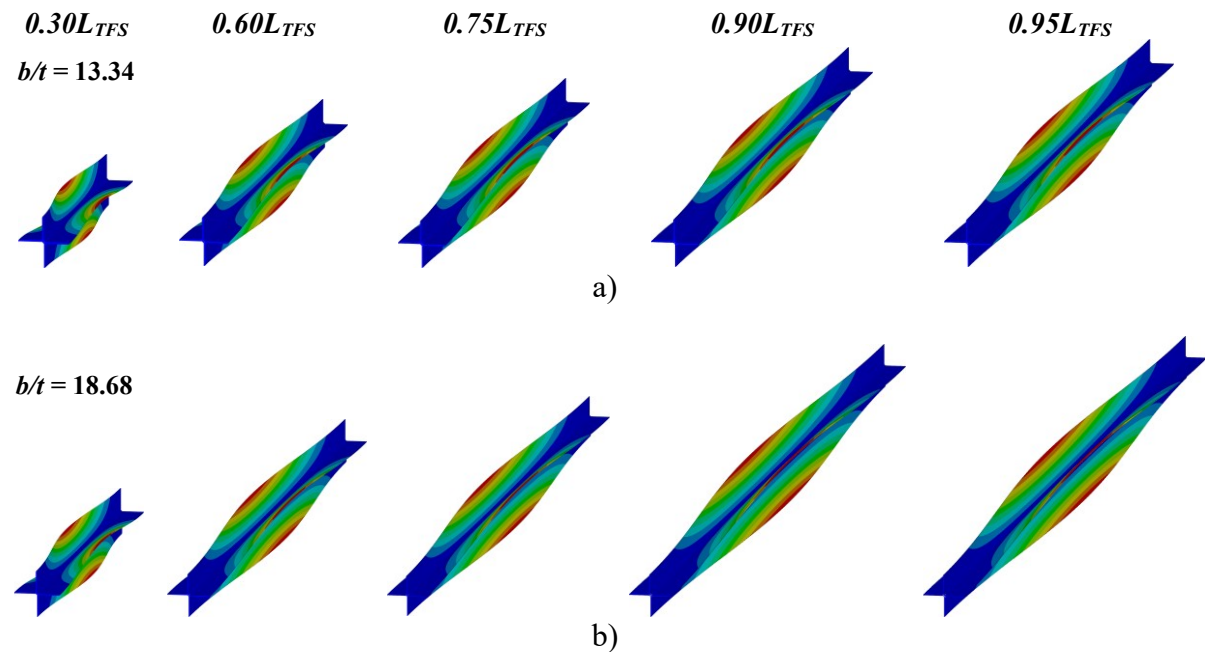


Figure 47: Torsional buckling elastic buckling shape for columns with lengths from $0.30L_{TFS}$ up to $0.95L_{TFS}$ considering a) $b/t = 13$ and b) $b/t = 18$.

4.4 Column elastic post-buckling behaviour

The next step was to investigate the elastic non-linear post-buckling behaviour of fixed-ended short-to-intermediate bolted equal-leg angles starred columns, i.e., prone to failure by torsional buckling ($L \leq L_{TFS}$). These analyses containing critical-mode initial geometrical imperfection are employed to determine the equilibrium paths, i.e., curves that correlate the corresponding load parameter value and mid-span ($L/2$) rigid-body cross-section torsional rotation (P/P_{cr} vs. β), is essential for study the potential mode interaction between critical global torsional buckling and minor-axis flexural buckling at lengths approaching the transition length (L_{TFS}), directly affecting the columns' ultimate load (P_u).

Therefore, five distinct column lengths sharing the same L/L_{TFS} ratio were selected for each cross-section ($L63.50 \times 4.76$ and $L88.90 \times 4.76$) to determine the equilibrium paths as the length increase on the signature curve ($0.30L_{TFS}$, $0.60L_{TFS}$, $0.75L_{TFS}$, $0.90L_{TFS}$, and $0.95L_{TFS}$), aiming to cover the torsional buckling range – depicted in Figure 48. All columns containing torsional critical mode initial geometrical imperfections with amplitudes equivalent to 10% of the equal-leg angle section thickness⁴ ($0.1t$) yielding an initial mid-span rigid-body cross-section torsional rotation equal to $\beta_0 = 0.0075$ rad and 0.0053 rad for $L63.50 \times 4.76$ and $L88.90 \times 4.76$, respectively.

Figure 48 presents the elastic post-buckling columns equilibrium paths (P/P_{cr} vs. β) results, where β represents the mid-span rigid-body cross-section torsional rotation relating to the applied load and is positive clockwise. Based on these elastic post-buckling results, the following comments can be made:

- i) As the width-to-thickness ratio (b/t) increases from 13.34 to 18.68, the elastic post-buckling behaviours of columns with fixed ends (created by a pair of welded equal-leg angles $2L63.50 \times 4.76$ and $2L88.90 \times 4.76$) reveals nearly identical equilibrium paths. Indicating that this behaviour is practically equivalent in lengths that share the same L/L_{TFS} ratio on the signature curve

⁴ According to Schaffer and Pekoz [57], this value is significant enough to avoid numerical problems, whereas it is ideal for allowing other critical buckling modes to contribute to the nonlinear analysis, i.e., accurately representing the column's elastic behaviour.

regardless of the b/t ratio up to 20, i.e., varying the compact equal-leg angle cross-section dimensions;

- ii) Additionally, it is essential to observe that all columns fixed-ended bolted starred columns exhibit clear, stable behaviour with substantial post-buckling strength ($P > P_{cr,T}$). Nevertheless, as the column lengths increase, approaching the transition length, there is a decrease in the post-buckling strength, although the load parameter consistently remains above 1;
- iii) After reaching the critical elastic torsional buckling load ($P/P_{cr,T} = 1$), all columns deformed configurations solely involve mid-span cross-section rigid-body rotations, with no occurrences of centroid displacements. In order to clarify this comment, Figure 49 provides, respectively, an isometric and top view showing the progression of the deformed configuration from 0.1 to 0.5 rad in columns with a length of $0.95L_{TFS}$ formed by a pair of welded equal-leg angles of $2L63.50 \times 4.76$ and $2L88.90 \times 4.76$, showing the position of each deformed configuration on the column equilibrium path;
- iv) Consequently, it has been observed that fixed-ended columns of short-to-intermediate length, composed of two compact equal-leg angle sections (specifically, with a width-to-thickness ratio $b/t < 20$) and featuring welded connections throughout their length, demonstrate no interaction between the two principal global critical modes – torsional and minor-axis flexural buckling – even for large deformations ($\beta = 0.6$ rad). This finding underscores such structural configurations' stability and distinct behaviour under critical conditions;
- v) Finally, the elastic post-buckling behaviour observed in this study for fixed-ended short-to-intermediate welded starred columns closely resembles that of fixed-ended short-to-intermediate cruciform columns that fail by torsional buckling. This similarity arises from the assembly procedure, which ensures the equal-leg angle columns' connection and overall column structural stability.

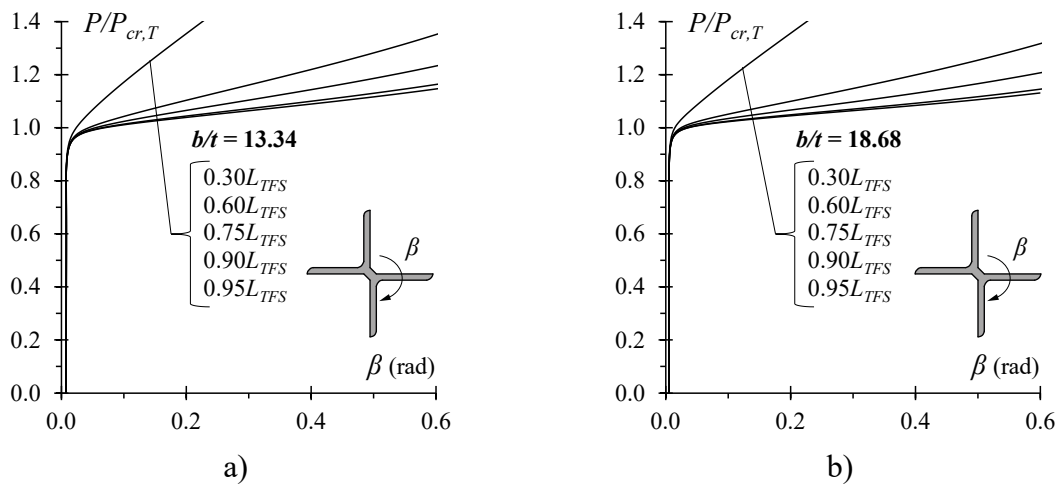


Figure 48: Fixed-ended welded starred columns equilibrium paths P/P_{cr} vs. β created through equal-leg angle cross-section with a) $b/t = 13.34$ and b) $b/t = 18.64$.

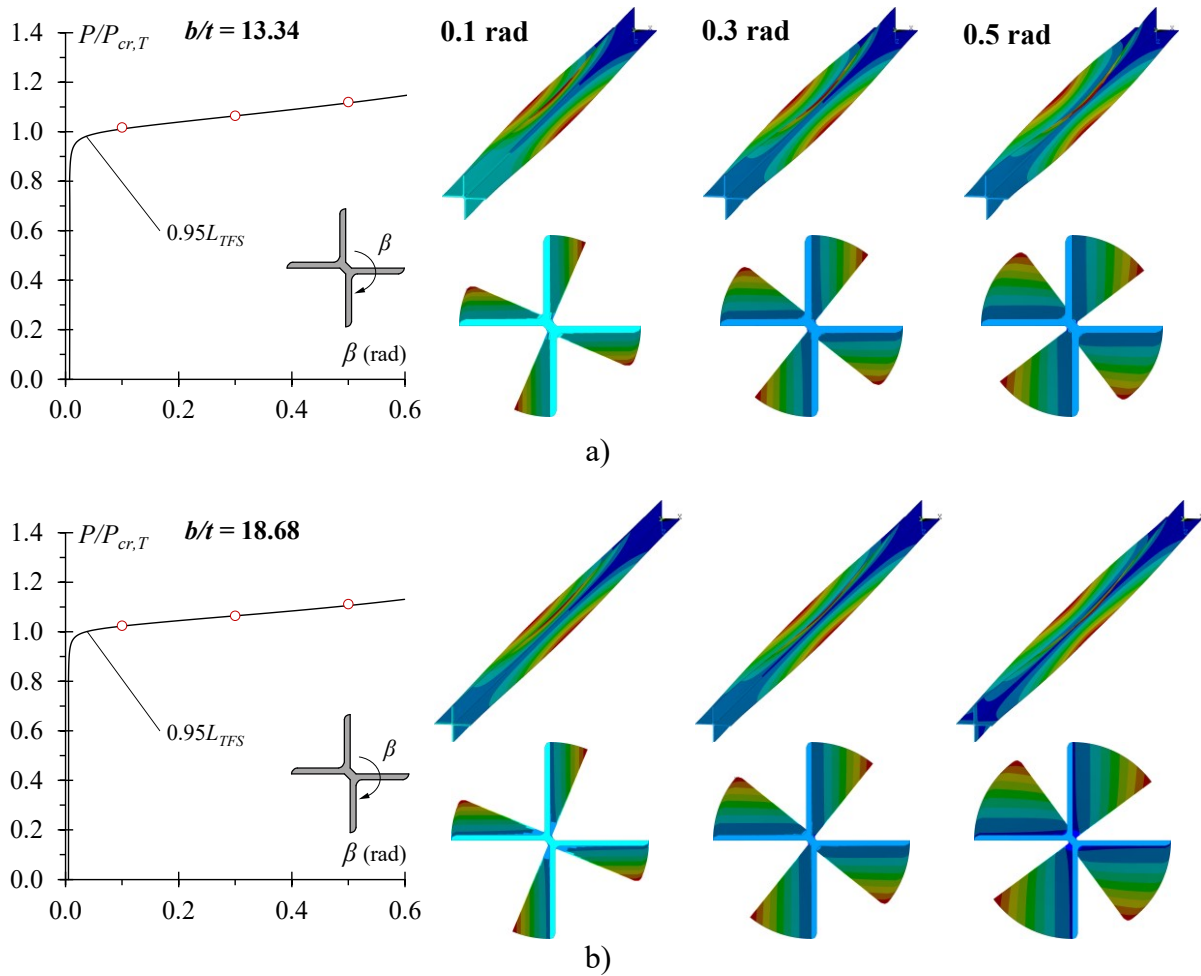


Figure 49: P/P_{cr} vs β equilibrium path for fixed-ended welded starred columns with length equal to $0.95L_{TFS}$ showing three columns deformed configuration as the cross-section torsional rotation increases from 0.1 to 0.5 rad featuring a) $b/t = 13.34$ and b) $b/t = 18.68$

4.5 Numerical model validation – stainless steel material behaviour

Following the preliminary investigation into the elastic buckling and post-buckling column behaviour, the finite element model was updated to include three crucial features from the experimental programme conducted by Botelho *et al.* [50]: (i) column geometry ($L63.50 \times 4.76$ cross-section with a column length of 700 mm), (ii) the experimental nonlinear austenitic stainless steel material behaviour stress-strain curve obtained from tensile coupon tests average depicted in Figure 50, and (iii) initial geometrical imperfection experimental amplitude measured equal to $t/13.64$ to establish the mid-span rigid-body rotation as illustrated in Figure 45(b).

The purpose was to evaluate the numerical model's accuracy (including a non-linear stress-strain material behaviour) and validate comparing against the experimental results concerning columns' ultimate load (P_u), load versus axial shortening curves (P vs Δ_y), load versus transverse displacements (P vs Δ_x and P vs Δ_z), and failure modes. Figure 51 compares the experimental and numerical results for fixed-ended bolted starred columns. These validation results provide the following comments:

- i) Concerning columns' ultimate loads, a satisfactory correlation is observed when comparing the finite element model and experimental loads, with a minor discrepancy of 2.43%. The numerical ultimate load reached 656.38 kN, whereas the experimental loads were 640.40 and 652.44 kN, respectively;
- ii) As shown in Figure 51(a), quantitative analysis reveals that the disparity in initial axial stiffness (observed during the linear phase) among equilibrium paths is roughly 8%, as indicated by the variance in slopes between the experimental and numerical findings. Furthermore, the divergence in post-buckling behaviour is less than 1% when comparing WSC-A and reaches 9.88% for WSC-B, up to an axial displacement of $\Delta_y = 7\text{mm}$. These results demonstrate a suitable correlation between experimental and numerical results of axial shortening equilibrium paths';
- iii) A less pronounced disparity is observed in transverse displacements (Δ_x and Δ_z), with the maximum value reaching 6% at (LVDT) *V7* – Figure 51(b) – after a large displacement $\Delta_x = 18\text{mm}$. This variation may be attributed to inherent inaccuracies that are unavoidable in real structural engineering tests. It should

be highlighted that LVDT measurements positioned at the mid-span ($L/2$) might exhibit deviations due to slip during the load application phase of the test, causing the measurement point to vary. As a consequence, this variability diminishes the precision of the acquired readings. However, the results make it possible to verify that the finite element model also defines these transverse equilibrium paths satisfactorily;

- iv) Figure 52 compares the experimental and numerical failure modes, emphasizing the notable agreement in the columns' deformed configuration in the finite element model, i.e., reproducing the torsional global buckling column behaviour. It is essential to visualise that the cross-section rotation causes the column collapse mechanism, i.e., the torsional failure mode start of yielding arises around the $1/4$ and $3/4$ – span zones of the welded starred column – highlighted in red circles. Mechanically, torsional buckling deformation cannot occur exclusively in one or two flanges of the starred cross-section, i.e., the cross-section's four flanges must behave identically (rigid body movement);
- v) It is worth noting that, in alignment with the study of elastic post-buckling analysis, the initial geometrical imperfection arising from torsional effects of mid-span rigid-body rotation ensures an adequate columns' structural response when also including the material behaviour nonlinearity;
- vi) Finally, considering all these observations, it can be concluded that the finite element model effectively replicates the behaviour of fixed-ended stainless steel welded starred columns prone to torsional buckling failure regarding (vi₁) ultimate failure load, (vi₂) equilibrium paths and (vi₃) failure mode.

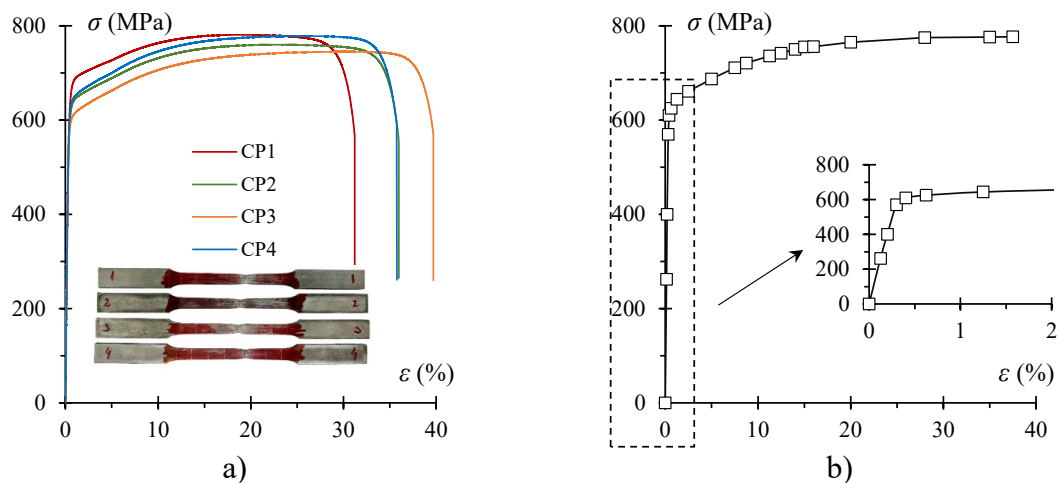


Figure 50: a) Tensile coupon tests obtained by Botelho *et al.* [50] and b) average stress-strain curve adopted to validate the finite element model.

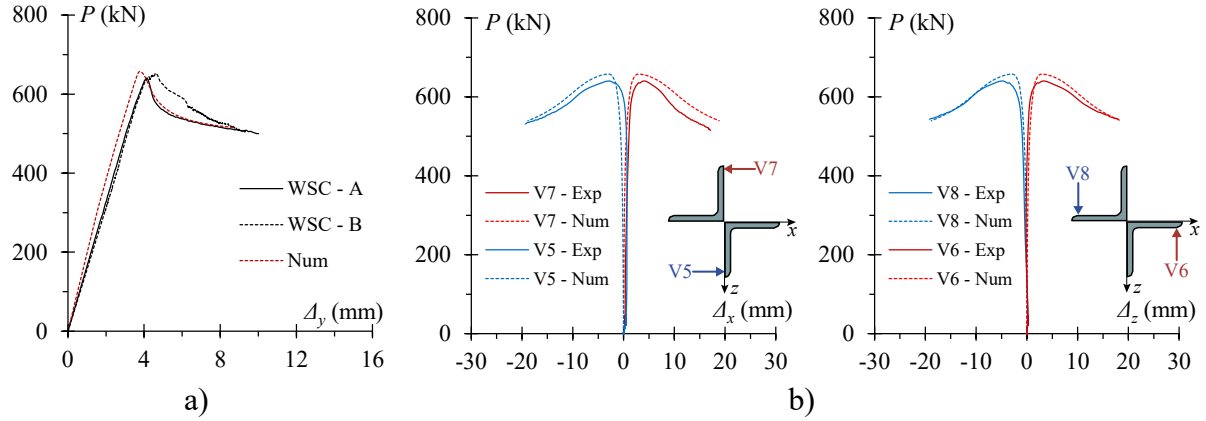


Figure 51: Finite element model validation comparing the column's equilibrium path concerning a) load versus axial shortening curves (P vs Δ_y) and b) load versus transverse displacements (P vs Δ_x and P vs Δ_z).

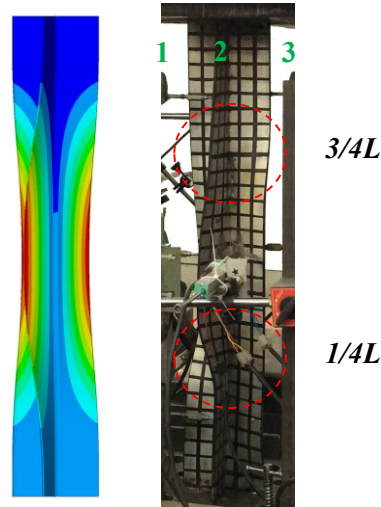


Figure 52: Finite element model comparing torsional failure mode.

4.6 Initial geometrical imperfection sensitivity

The initial geometrical imperfection sensitivity study of fixed-ended stainless steel welded starred columns involves a comparison of the numerical ultimate loads ($P_{u,FE}$) and load vs axial shortening curves (P vs Δ_y) results. Five amplitude values are assumed concerning the

mid-span initial cross-section torsional rotation (β_0), specifically $t/20$, $t/10$, $t/5$, $t/2.5$, and t – as illustrated in Figure 45(b).

Firstly, the effect of the initial geometrical imperfection amplitude is assessed using the measured imperfection amplitude from the experimental column geometry as a reference, i.e., the validation study (VS) – $L63.50 \times 4.76$, $L = 700$ mm, and $t/13.64$. The subsequent stage expands this investigation to evaluate this impact on two additional intermediate columns as the length increases (1600 mm and 2400 mm), consequently ranging from $0.24L/L_{TFS}$ to $0.82L/L_{TFS}$.

Table 6 provides the amplitude of the initial geometrical imperfection adopted, the initial mid-span cross-section torsional rotation yielded, and the ultimate numerical load obtained for each column. Additionally, Figure 53 shows load vs axial shortening curves (P vs Δ_y) concerning each initial geometrical imperfection amplitude for the selected columns. Based on the obtained results, the following remarks can be highlighted:

- i) As expected, there is a decrease in columns' ultimate loads with an increase in the initial geometrical imperfection. However, this reduction becomes significant only when comparing the extremes of initial geometrical imperfection amplitudes, from the smallest ($t/20$) to the largest (t), showing reductions up to 17.80% for a column length of 700 mm, 14.89% for 1600 mm, and 12.47% for 2400 mm in length. This trend suggests that the impact of initial geometrical imperfections on the ultimate load diminishes as the column length increases;
- ii) The decrease in the ultimate load is significantly less prominent within the amplitude range from $t/20$ to $t/2.5$, reaching a maximum value of 10.27% for the column length of 700 mm. Following this reasoning, a comparison between amplitudes of $t/20$ and $t/5$ reveals that the reduction in ultimate load is restricted to a maximum of 5.31%;
- iii) These comparisons emphasise the need for a considerable increase in the initial geometrical imperfection amplitude value to influence the column's ultimate load consistently. In other words, an increase of almost 20 times ($t/20 \rightarrow t$) in the initial geometrical imperfection amplitude value is necessary for this influence to become statistically significant;
- iv) Additionally, as depicted in Figure 53, concerning most substantial amplitude values equal to $t/2.5$ and t , it becomes evident that a substantial increase in the initial geometrical imperfection value induces a deviation in the column's

equilibrium path-load vs axial shortening curves (P vs Δ_y). These results indicate that when using a high initial geometrical imperfection value might lead to misinterpretation of the structural element's behaviour and, consequently, ultimate strength;

- v) In general, it is observed in Table 6 and Figure 53 that the initial geometrical imperfection amplitude value equal to $t/20$, $t/10$, and $t/5$ presents (v_1) an adequate correlation concerning the column's ultimate load and (v_2) equilibrium path for each length, i.e., mitigating the reduction in column resistance while ensuring a satisfactory non-linear response;
- vi) Indeed, the initial geometrical imperfection amplitude value equal to $t/10$ (highlighted in blue) is commonly used in previous works concerning fixed-ended short-to-intermediate columns that fail by torsional buckling with cruciform section [36], consistently achieving satisfactory results. Therefore, based on these observations and in alignment with the previous works available in the literature, the initial geometrical imperfection amplitude value $t/10$ is adopted in the developed parametric analysis in this work.

Table 6: Initial geometrical imperfection sensitivity study for fixed-ended stainless steel welded starred columns ranging from $0.24L/L_{TFS}$ to $0.83L/L_{TFS}$.

<i>Column</i>	<i>Amplitude</i>	β_0 (rad)	$P_{u,FE}$ (kN)
$L63.50 \times 4.76 - 700 \text{ mm}$	$t/13.64 - VS$	0.0055	656.38
	$t/20$	0.0037	662.10
	$t/10$	0.0075	650.39
	$t/5$	0.0149	626.95
	$t/2.5$	0.0299	594.06
	t	0.0748	544.20
$L63.50 \times 4.76 - 1600 \text{ mm}$	$t/20$	0.0037	637.40
	$t/10$	0.0075	627.66
	$t/5$	0.0149	608.00
	$t/2.5$	0.0299	582.36
	t	0.0748	542.47
$L63.50 \times 4.76 - 2400 \text{ mm}$	$t/20$	0.0037	629.67
	$t/10$	0.0075	619.60
	$t/5$	0.0149	604.64
	$t/2.5$	0.0299	584.98
	t	0.0748	550.56

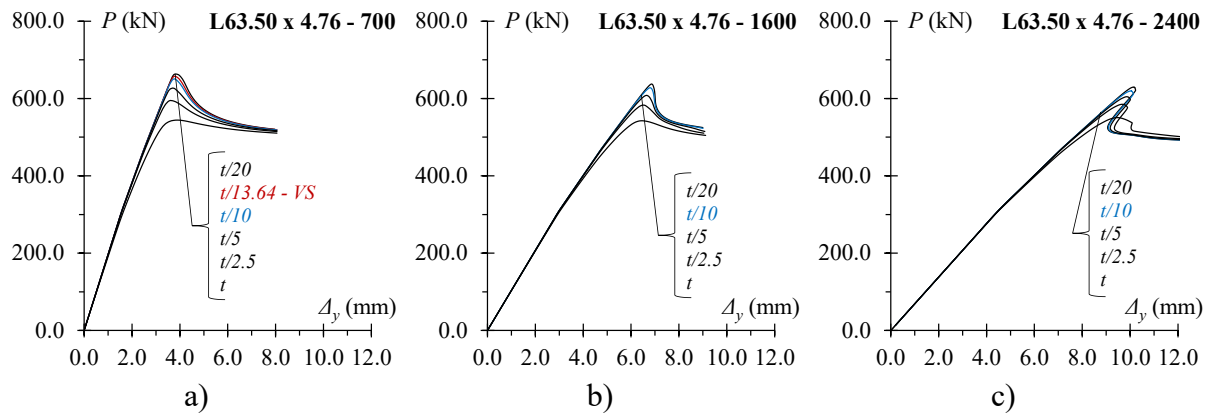


Figure 53: Load vs axial shortening curves (P vs Δ_y) concerning each initial geometrical imperfection amplitude for fixed-ended welded starred columns with a length equal to a) 700 mm, b) 1600 mm, and c) 2400 mm.

5 WELDED STARRED COLUMNS NUMERICAL PARAMETRIC INVESTIGATION

5.1 Introduction

Following the validation of the finite element model and the sensitivity study regarding the initial geometrical imperfections, a parametric investigation was conducted to expand the database of numerical ultimate loads of austenitic and duplex stainless steel fixed-ended short-to-intermediate bolted starred columns, i.e., solely column lengths that fail by torsional buckling – the main aim of this work.

Hence, the subsequent steps encompassed: (i) including the austenitic and duplex stainless steel behaviour derived from experimental tests; (ii) selecting the appropriate cross-section profiles ($b/t < 20$); (iii) numerical investigation of the geometrical section's properties, i.e., torsional constant (I_t) and secondary warping (I_{ws}); (iv) column length selection through elastic buckling analysis ($L \leq L_{TFS}$); (v) initial geometrical imperfection with amplitude equal to $t/10$; (vi) the influence of residual stress distribution on the ultimate load; and (vii) nonlinear analysis to achieve the fixed-ended short-to-intermediate welded starred columns numerical ultimate load ($P_{u,FE}$).

5.2 Austenitic and duplex stainless steel material behaviour

The stress-strain curve of austenitic and duplex stainless steel incorporated into the finite element model was obtained from tensile tests – crucial for characterising material properties – conducted by Sarquis *et al.* [45] and Afshan *et al.* [3] for austenitic and duplex stainless steel, respectively. Given the material's nonlinear behaviour, the stress-strain curves were represented using a multilinear isotropic curve implemented through the “MISO” command in ANSYS software [29].

Figure 54(a) and (b) depict the complete stress-strain curves (σ vs. ε) employed in this parametric analysis, derived from the experimental data and characterised by twenty-two points for austenitic stainless steel and twenty-nine points for duplex stainless steel. Table 7 briefly provides the essential material properties for austenitic and duplex stainless steel, in which E is

Young's Modulus, $\sigma_{0.2\%}$ is the stainless steel 0.2% proof stress, σ_u is the ultimate stress, and ε_u is the failure strain at σ_u . The observation of Table 7 and Figure 54 prompts the following comments:

- i) It is well-known that stainless steel material exhibits remarkable ductility and strain-hardening characteristics. Nevertheless, there is a notable disparity in ductility between austenitic and duplex materials. Austenitic stainless steel demonstrates a ductility of up to 60.69% strain (ε_u) at the point of ultimate stress (σ_u). In contrast, duplex stainless steel displays lower ductility, with a value of 20.02%;
- ii) The initial Young's Modulus (E) is a critical mechanical property in columns' structural behaviour and instability phenomena. It is worth mentioning that austenitic stainless steel ($E_A = 207.91$ GPa) exhibits greater initial stiffness compared to duplex stainless steel ($E_D = 177.97$ GPa), with a ratio (E_A / E_D) of 1.17. Poisson's ratio remains constant at $\nu = 0.3$, and the shear modulus is calculated as $G = E/[2(1 + \nu)]$;
- iii) This difference directly influences the columns' elastic critical loads, i.e., the torsional buckling load and minor-axis flexural buckling load decrease in the same ratio as Young's Modulus. Nonetheless, despite the disparity in Young's Modulus of the materials, the transition length of the welded columns will remain consistent for both materials, simplifying the process of selecting column lengths for parametric investigation, i.e., $L_{TFS,A} = L_{TFS,D}$;
- iv) Furthermore, austenitic stainless steel exhibits a 0.2% proof stress ($\sigma_{0.2\%A} = 310.11$ MPa) – a parameter used as the yield strength in design calculations – which is notably lower than that of duplex stainless steel ($\sigma_{0.2\%D} = 548.99$ MPa). This results in a ratio ($\sigma_{0.2\%A} / \sigma_{0.2\%D}$) of 0.56 between these two types of stainless steel, highlighting another crucial difference for the investigated instability phenomena;
- v) This variation in 0.2% proof stress allows for a broader range of non-dimensional torsional slenderness (λ_T) to be covered without requiring modifications to the column's geometry. In other words, identical column geometries will yield two distinct non-dimensional torsional slenderness values solely due to the difference in material strength.

Table 7: Summary of essential material properties used in the finite element model.

<i>Stainless Steel</i>	E (GPa)	$\sigma_{0.2\%}$ (MPa)	σ_u (MPa)	ε_u (%)	$\sigma_u/\sigma_{0.2\%}$
<i>Austenitic (A)</i>	207.91	310.11	718.62	60.69	2.31
<i>Duplex (D)</i>	177.97	548.99	743.28	20.02	1.35

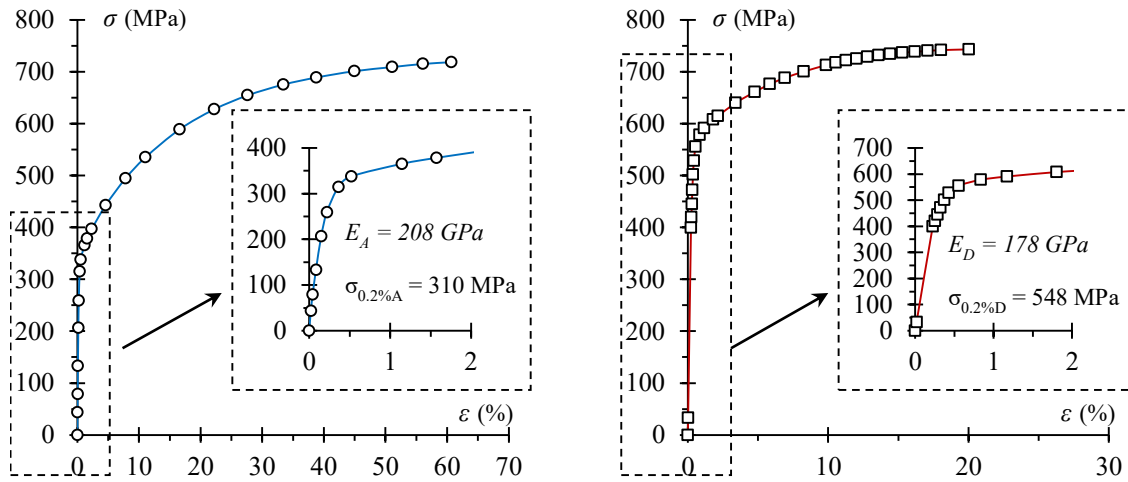


Figure 54: a) Austenitic and b) Duplex stainless steel stress-strain curves adopted in the finite element model.

5.3 Equal-leg angle cross-section selection

Twelve equal-leg angle cross-sections were selected from Elinox's catalogue [58], a recognised supplier of stainless steel in Brazil. This selection was explicitly centred on compact equal-leg angles, i.e., $b/t < 20$, to assess the ultimate loads of fixed-ended short-to-intermediate welded starred columns. It comprises a range of equal-leg angle cross-section geometries encompassing variations in width (b), thickness (t), and width/thickness ratio (b/t) to cover a practical hot-rolled cross-section range completely. Table 8 provides information on the cross-section identification (ID), dimensions (b and t), and width/thickness ratio (b/t) from 5 up to 18.68.

Table 8: Equal-leg angle cross-section selection to create a welded starred section.

<i>ID</i>	<i>Cross-section</i>	<i>b</i> (mm)	<i>t</i> (mm)	<i>b/t</i>
<i>S1</i>	63.50x12.70	63.50	12.70	5.00
<i>S2</i>	76.20x12.70	76.20	12.70	6.00
<i>S3</i>	63.50x9.53	63.50	9.53	6.66
<i>S4</i>	101.60x12.70	101.60	12.70	8.00
<i>S5</i>	28.58x3.18	28.58	3.18	8.99
<i>S6</i>	76.20x7.94	76.20	7.94	9.60
<i>S7</i>	63.50x6.35	63.50	6.35	10.00
<i>S8</i>	76.20x6.35	76.20	6.35	12.00
<i>S9</i>	63.50x4.76	63.50	4.76	13.34
<i>S10</i>	69.85x4.76	69.85	4.76	14.67
<i>S11</i>	76.20x4.76	76.20	4.76	16.01
<i>S12</i>	88.90x4.76	88.90	4.76	18.68

5.4 Welded starred section properties

Appendix A shows that the welded cross-section geometrical properties of welded starred and plain cruciform cross-sections are distinct, i.e., secondary warping constant (I_{ws}) and torsion constant (I_T). Therefore, a numerical study compared the selected twelve welded starred sections with plain cruciform sections sharing the same geometry. Table 9 shows the cross-section identification (*ID*) and the geometrical properties (I_T and I_{ws}) of welded starred and plain cruciform. The following comments can be made:

- i) The main parameter for comparing welded starred and plain cruciform sections' properties is the width/thickness ratio (b/t). Note, regardless of cross-section geometry (b and t – Table 8), the results show tendencies concerning the values of torsion constants ($I_{T,sta}/I_{T,cru}$) and secondary warping ($I_{ws,sta}/I_{ws,cru}$) as the b/t ratio increases from 5 to 18.68;
- ii) There is not much difference in the ratio between the torsion constants of starred and cruciform sections ($I_{T,sta}/I_{T,cru}$), with a maximum of 22% and a tendency to approach unity as the b/t ratio increases;
- iii) The welded starred cross-section secondary warping constant ($I_{ws,sta}$) tends to be approximately four times the plain cruciform cross-section secondary warping constant ($I_{ws,cru}$). This value is more evident as the b/t ratio increases;

- iv) It is also noted that from the ratio $b/t \geq 10$ (i.e., $S7$ to $S12$), the results show convergence in section properties, meaning that the welded starred secondary warping constant ($I_{ws,sta}$) can be calculated employing a simple modification in Eq. (A.1), given by Eq. (58). This modification results in a maximum discrepancy of 2%, decreasing as the b/t ratio increases. Similarly, the welded starred torsion constant ($I_{T,sta}$) can be calculated according to Eq. (59).
- v) Based on these statements, Eqs. (58) and (59) can simplify and aid the welded starred columns' design through analogies between cross-sections since calculating the geometrical properties for columns with plain cruciform sections is a straightforward task. In contrast, the welded starred sections present a greater complexity due to their geometry.

$$I_{ws,sta} = 3.97 \frac{b^3 t^3}{9} \quad (58)$$

$$I_{T,sta} = 1.08 \frac{4bt^3}{3} \quad (59)$$

Table 9: Comparison between welded starred and cruciform geometrical sections' properties.

<i>ID</i>	<i>Welded starred section</i>		<i>Cruciform section</i>		$\frac{I_{T,sta}}{I_{T,cru}}$	$\frac{I_{ws,sta}}{I_{ws,cru}}$
	$I_{T,sta}$ (mm^4)	$I_{ws,sta}$ (mm^6)	$I_{T,cru}$ (mm^4)	$I_{ws,cru}$ (mm^6)		
<i>S1</i>	211478	221642781	173429	58276012	1.22	3.80
<i>S2</i>	246169	389171145	208115	100700949	1.18	3.86
<i>S3</i>	85394	95763135	73280	24623930	1.17	3.89
<i>S4</i>	315534	936344838	277487	238698548	1.14	3.92
<i>S5</i>	1380	328183	1225	83411	1.13	3.93
<i>S6</i>	56711	97043911	50857	24608430	1.12	3.94
<i>S7</i>	24068	28764863	21678	7284501	1.11	3.95
<i>S8</i>	28401	49882887	26014	12587618	1.09	3.96
<i>S9</i>	9895	12182747	9131	3068312	1.08	3.97
<i>S10</i>	10807	16233194	10044	4083923	1.08	3.97
<i>S11</i>	11719	21093111	10957	5302043	1.07	3.98
<i>S12</i>	13544	33535618	12783	8419448	1.06	3.98
				Mean	1.12	3.93
				CoV	0.05	0.05

5.5 Residual stresses effects

The residual stresses (defined as self-equilibrating) in welded starred columns arise from the construction process to join two equal-leg angles by the corner (welding technique). This effect was included in the finite element model using the command “INISTATE”, i.e., the solid finite element’s initial stress is assigned at each numerical integration (Gauss points) according to its position in the cross-section.

The 3-point distribution was employed with negative values (“-”) corresponding to compressive stresses and positive values (“+”) to tensile stresses – currently used in the Eurocode 3 [4][5] and also adopted by Trahair [59] in plain cruciform sections. The $\beta_{RS} = 0.3$ was adopted as the maximum value that correlates the yield strength ($\sigma_{0.2\%}$) to the peak (maximum) residual stress, illustrated in Figure 55(a). Additionally, Figure 55(b) presents the residual stress distribution in the finite element model for an austenitic stainless welded starred column ($\sigma_{0.2\%} = 310$ MPa).

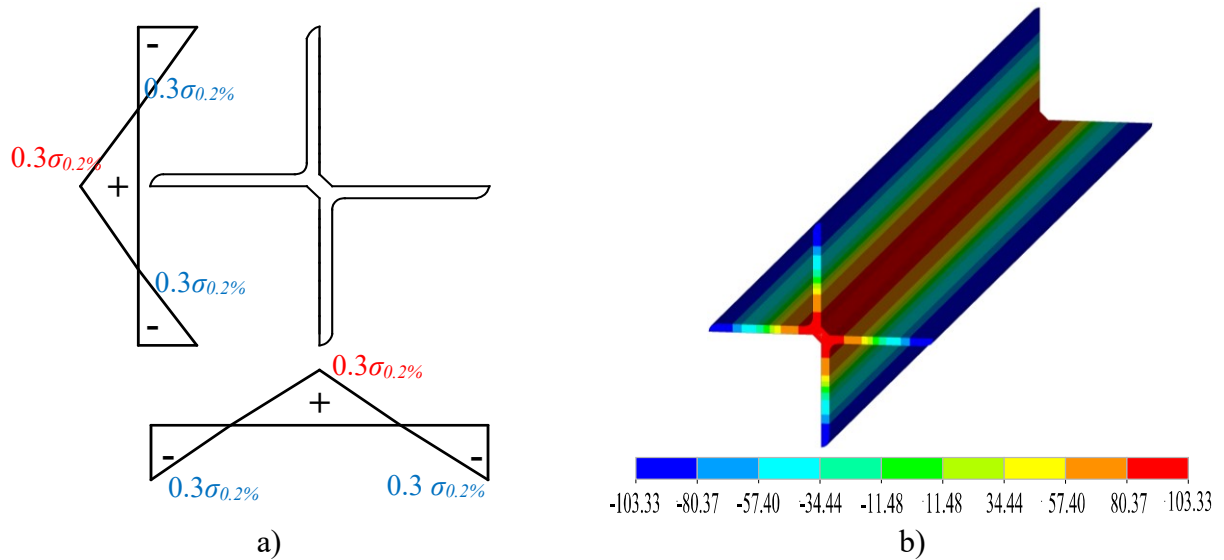


Figure 55: a) Adopted 3-point residual stress distribution on the welded starred cross-section and b) applied residual stress in the finite element model in ANSYS [29].

The effect caused by the residual stresses on the torsional buckling of fixed-ended austenitic and duplex stainless steel welded starred columns’ behaviour was assessed by

comparing the (i) equilibrium paths ($P_{u,FE}$ vs. Δ_v), (ii) deformed shapes development and (iii) ultimate load for columns with and without residual stresses, $P_{u,RS}$ and $P_{u,WRS}$, respectively.

Therefore, a parametric study was carried out verifying four different cross-sections ($S4$, $S7$, $S9$, and $S12$) and 24 lengths for each material (austenitic and duplex stainless steel), i.e., 48 investigated cases covering a broad L/L_{TFS} ratio from 0.11 up to 1.0, and, consequently, a non-dimensional torsional slenderness range (λ_T) from 0.40 up to 1.52. It is essential to highlight that columns with the same L/L_{TFS} ratio but with different materials (austenitic or duplex) have different non-dimensional torsional slenderness.

Initially, Figure 56 and Figure 57 show a comparison between welded starred columns' equilibrium paths and deformed shape evolution with identical geometry ($S9$ and $L = 700$ mm) considering columns without residual stresses (WRS) and with residual stresses (RS) for austenitic and duplex stainless steel, respectively. In addition, Figure 58(a) summarises the parametric investigation results graphically, displaying the variation of the ultimate load ratio ($P_{u,RS}/P_{u,WRS}$) with the non-dimensional L/L_{TFS} ratio. The observation of these results leads to the following comments:

- i) For both austenitic and duplex stainless steel, the welded starred columns without or with initial stresses exhibit similar equilibrium paths and deformed shape evolution, indicating a consistent failure mode across both materials;
- ii) As expected, the ultimate loads of fixed-ended welded starred columns decrease when the residual stresses are included in the finite element model. However, the results reveal that residual stresses have a minor effect on torsional buckling resistance for both materials, with a decrease of 0.9% for austenitic and 6.1% for duplex, as illustrated in Figure 56 and Figure 57, respectively. Indeed, duplex stainless steel presents a more significant drop due to the elevated 0.2% proof stress (as referenced in Table 7), which contributes to a greater distribution of residual stresses in the columns compared to those made from austenitic stainless steel;
- iii) The quantitative analysis presented in Figure 58(b) shows an overview of the reduction factor (χ_{RS}) relative to the column length within the scope of this study, specifically $L \leq L_{TFS}$. It is observed that closer to the transition length, the impact of residual stress becomes more pronounced, with reduction factors reaching up to 6.75% for duplex stainless steel columns and up to 4.3% for austenitic stainless steel columns. Additionally, this decrease can be explicitly attributed

to the longer lengths exhibiting lower post-buckling resistance compared to shorter ones;

- iv) Therefore, it becomes evident that the impact of residual stresses on the behaviour of fixed-ended welded starred columns subjected to torsional buckling is negligible for both types of steel. This observation is consistent with results from similar studies on fixed-ended hot-rolled equal-leg angle columns prone to failure by flexural-torsional buckling [35], as well as research on angle sections by Može *et al.* [60].

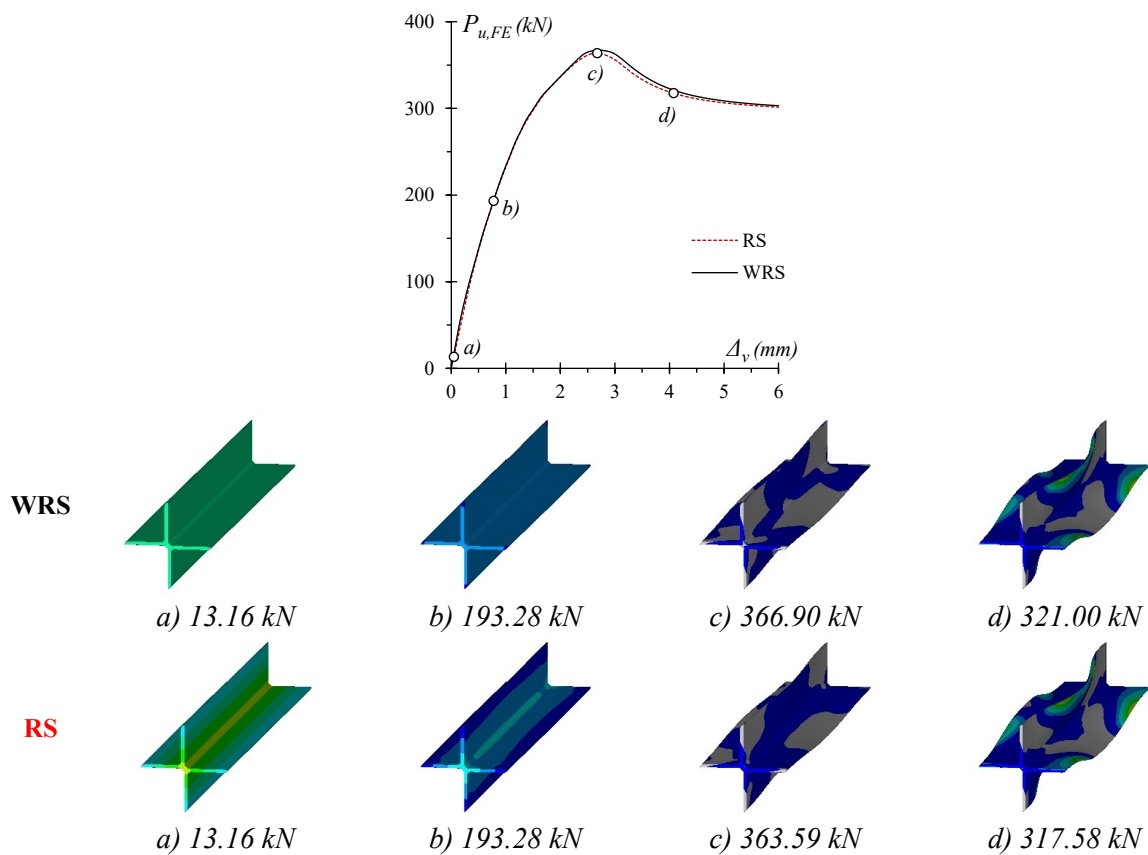


Figure 56: Equilibrium paths ($P_{u,FE}$ vs. Δ_v) and deformed configuration development of austenitic stainless steel welded starred column without and with residual stresses.

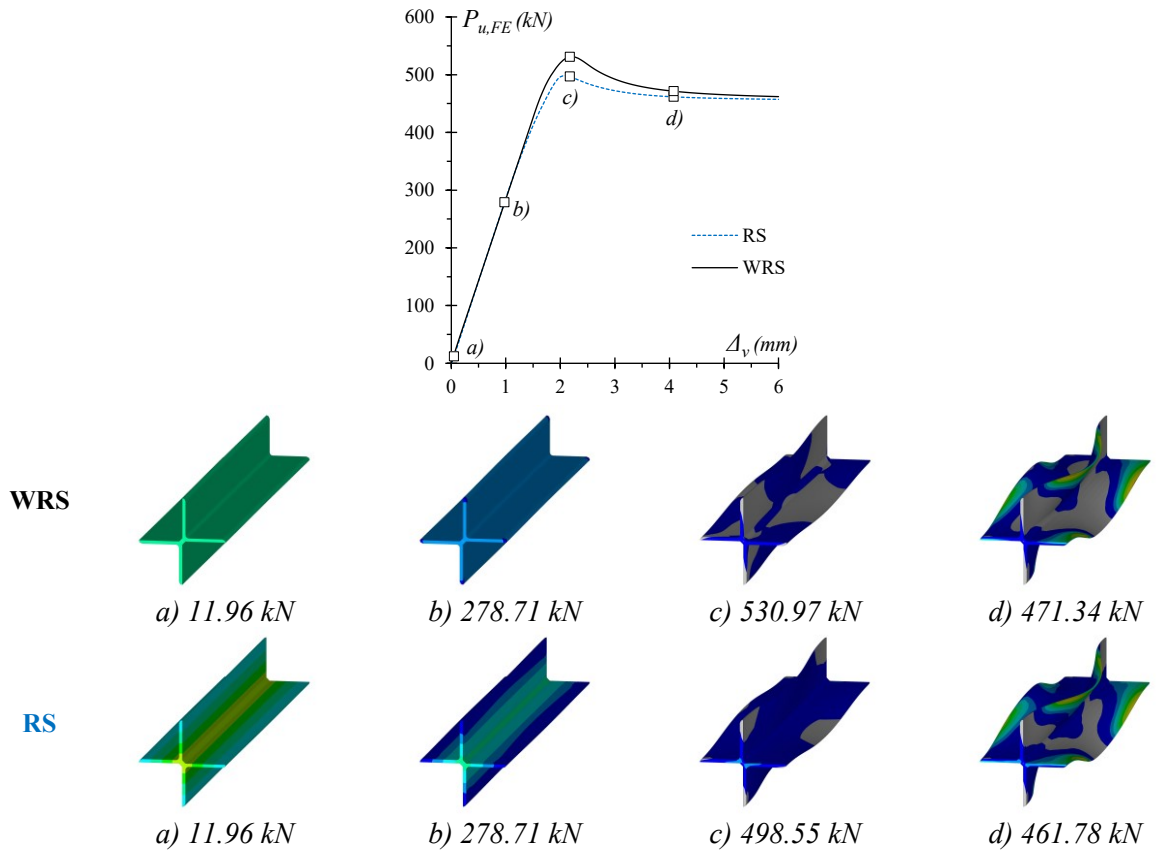


Figure 57: Equilibrium paths ($P_{u,FE}$ vs. Δ_v) and deformed configuration development of duplex stainless steel welded starred column without and with residual stresses.

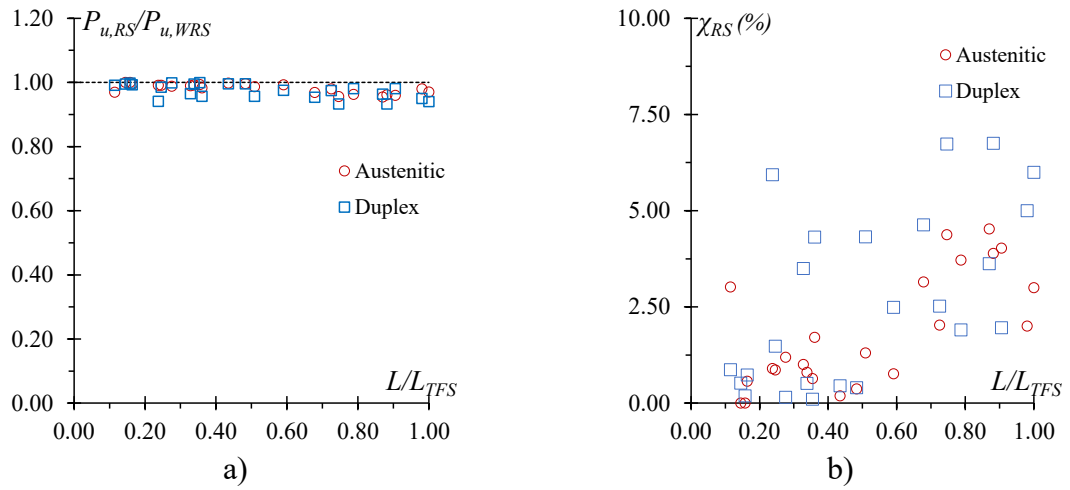


Figure 58: a) Ultimate strength ratio ($P_{u,RS}/P_{u,WRS}$) and b) reduction factor (χ_{RS}) concerning non-dimensional L/L_{TFS} ratio.

5.6 Numerical results

Based on the elastic buckling behaviour, the column lengths selection for each welded starred cross-section was limited to the transition length in the signature curve (i.e., $L \leq L_{TFS}$)⁵, aiming to investigate only the torsional buckling failure mode – the main purpose of this work. Table 10 shows the cross-section identification (*ID*), the geometrical properties (A_g , I_b , and I_{ws}), and the selected lengths (L), increasing by 100 to 100 mm – except the last one – ranging from 300 mm up to each welded starred cross-section transition length (L_{TFS}).

As observed before, it is essential to highlight that the transition length is always equal for both austenitic and duplex stainless steel. Therefore, the exact column lengths were investigated for each material, totalling 544 finite element models, in which *A* and *D* designate austenitic and duplex stainless steel columns, respectively.

Figure 59 summarises the parametric analysis results graphically. The vertical axis represents the normalised strength, i.e., the variation of the numerical ultimate load ratio $P_{u,FE}/A_g\sigma_{0.2\%}$ with non-dimensional torsional slenderness $\lambda_T = [(A_g\sigma_{0.2\%})/P_{cr,T}]^{0.5}$ in the horizontal axis covering a range from 0.19 to 1.52. The observation of all these results enables the following conclusions:

- i) For the same column geometry, the difference in non-dimensional torsional slenderness λ_T is directly related to the 0.2% proof stress materials ($\sigma_{0.2\%A} / \sigma_{0.2\%D} = 0.56$) since the discrepancy in elastic critical torsional buckling load ($P_{cr,T}$) is short, equal to 17% as shown in Figure 59(a). In other words, their non-dimensional slenderness increases or decreases by varying the proof stress ($\sigma_{0.2\%}$), improving the investigation and covering a more comprehensive range. For instance, concerning columns formed by cross-section *S11*, the austenitic stainless steel columns' non-dimensional slenderness range is from 0.80 to 1.00, while for duplex stainless steel columns' it is 0.86 to 1.32;
- ii) Based on the non-dimensional torsional slenderness values covered in this work, two distinct column failure modes are evident: (ii₁) gross cross-section yielding occurs for columns with normalised slenderness up to 0.74, while (ii₂) column failure due to torsional buckling becomes apparent beyond this threshold;

⁵ All $P_{cr,T}/P_{cr,F}$ elastic buckling load ratio is evidently under 1, covering a range from 0.05 to 0.40 ratios – except for the transition length (L_{TFS}).

- iii) Notably, the columns formed by sections *SI* up to *S7* ($b/t = 5$ up to 10, respectively) present failure due to gross cross-section yielding, i.e., the numerical failure load is greater or equal to squash load ($P_{u,FE}/A_g\sigma_{0.2\%} \geq 1$), reaching a ratio up to 1.5. It can be explained because stocky columns formed by compact sections present a high critical torsional buckling load, leading to the cross-section yielding failure before column torsional buckling occurs ($P_{cr,T} \gg A_g\sigma_{0.2\%}$). Also, these values reveal the strain-hardening capacity of stainless steel;
- iv) Similarly, the torsional buckling failure mode becomes predominant from this value $\lambda_T = 0.74$ onwards, where a decrease in gross cross-section yielding of up to approximately 30% was observed, i.e., $P_{u,FE}/A_g\sigma_{0.2\%} = 0.7$;
- v) Regardless of stainless steel type, columns with similar non-dimensional torsional slenderness (λ_T) values present similar behaviour and ultimate strengths. As columns with closely matched torsional slenderness values display nearly identical ultimate strengths, it becomes apparent that this parameter is a practical and convenient metric for constructing a design column buckling curve, i.e., the design curve proves to be effective in predicting the load-carrying capacity of columns susceptible to torsional buckling failure;
- vi) It indicates that the design standard developed is satisfactory for setting a buckling curve – Eurocode 3: Part 1.4 [4] column buckling curve “*b*” – to forecast the ultimate strength of fixed-ended stainless steel columns subjected to torsional buckling. This observation is particularly evident when comparing the numerical results to the two curves established by Eurocode 3: Part 1.4 [4], specifically “*a*” and “*b*”. The European code assessment is presented in section 8.2.

Table 10: Cross-section dimensions, ratio b/t , geometrical section's properties, and chosen lengths for numerical parametric investigation.

ID	A_g (mm ²)	I_T (mm ⁴)	I_{ws} (mm ⁶)	L (mm)	Austenitic columns		Duplex columns	
					(A)		(D)	
$S1$	2991.93	211478.85	221642781.00	300 – 810	6		6	
$S2$	3637.09	246169.21	389171145.00	300 – 1200	8		8	
$S3$	2288.93	85394.87	95763135.90	300 – 1250	10		10	
$S4$	4927.41	315534.47	936344838.00	300 – 2540	23		23	
$S5$	348.87	1380.11	328183.45	300 – 790	5		5	
$S6$	2328.70	56711.05	97043911.90	300 – 2370	21		21	
$S7$	1554.43	24068.71	28764863.50	300 – 2070	18		18	
$S8$	1877.01	28401.84	49882887.00	300 – 3120	29		29	
$S9$	1176.19	9895.20	12182747.70	300 – 2950	27		27	
$S10$	1297.09	10807.49	16233194.20	300 – 3640	34		34	
$S11$	1417.99	11719.86	21093111.40	300 – 4370	41		41	
$S12$	1659.80	13544.60	33535618.90	300 – 6100	50		50	

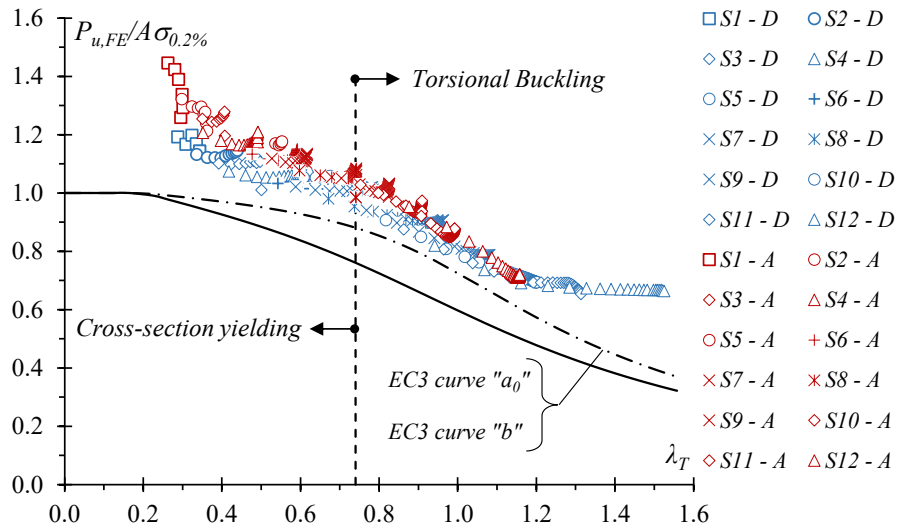


Figure 59: Numerical results compared to buckling curves “ a_0 ” and “ b ” for torsional buckling failure mode.

6 BOLTED STARRED COLUMNS FINITE ELEMENT MODEL DEVELOPMENT

The numerical model was developed using the finite element software ANSYS 17.0 [29] to investigate the structural behaviour and ultimate strength of stainless steel fixed-ended short-to-intermediate bolted starred columns, i.e., columns susceptible to torsional buckling failure. This section presents the particulars of the developed finite element model, including information on column geometry, element types, mesh size, boundary conditions, contact modelling, bolt preload, the implementation of initial geometrical imperfections, and the employed solution technique.

6.1 Element type and bolted starred column geometry

The finite element model bolted starred column geometry assembly procedure follows the same steps in the experimental programme described in section 3.2. Initially, two distinct equal-leg angle columns length (L) are created and aligned along the longitudinal axis (y) with an equal spacing – equivalent to half of the cross-section thickness ($t/2$) – in both the transverse directions (x and z). Four holes with a diameter equal to 14 mm ($d_h = 14$ mm) – that exceed the nominal diameter of the bolt ($d_b = 12.70$ mm) – are created at the midpoints of the one equal-leg angle cross-section ($b/2$), two positioned at one-third ($1/3L$) and two others at two-thirds ($2/3L$) of the columns' length, at z and x transverse directions, respectively, to fit the holes of the connection plates.

Additionally, two rectangular plates, each with two holes ($d_p = 14$ mm), were positioned to function as the intermediary connection interface between the columns, one plate at one-third and the other at two-thirds of the columns' length, with dimensions based on the equal-leg angle cross-section ($b \times t$), featuring a height, width and thickness plate equal to $h_p = 3b - t$, $w_p = 2b + t$ and $t_p = t$, respectively. For instance, for equal-leg angle cross-section $L63.50 \times 4.76$, the dimensions of the connection plate are shown in Figure 35(c).

The four bolts are also represented using 3D shapes elements, with each node having three degrees of freedom (3 DOFs). This configuration leads to a substantial number of equations that must be solved during the analysis. Thus, a simplified cylinder solid bolt

modelling approach was adopted, in which the threads on the bolt are removed⁶, and the nut and the bolt head share identical diameter and thickness dimensions ($d_{b,h} = d_{b,n} = 17$ mm and $t_b = 5$ mm) with grip length equal to $2t$.

Figure 60 illustrates the finite element model bolted connection, the dimensions of the plate and the bolt geometry used. It is essential to highlight that all the column geometries investigated in this study have identical dimensions of the connection plates' holes and the bolts (except for the bolt grip length, which naturally adjusts according to the cross-section thickness t).

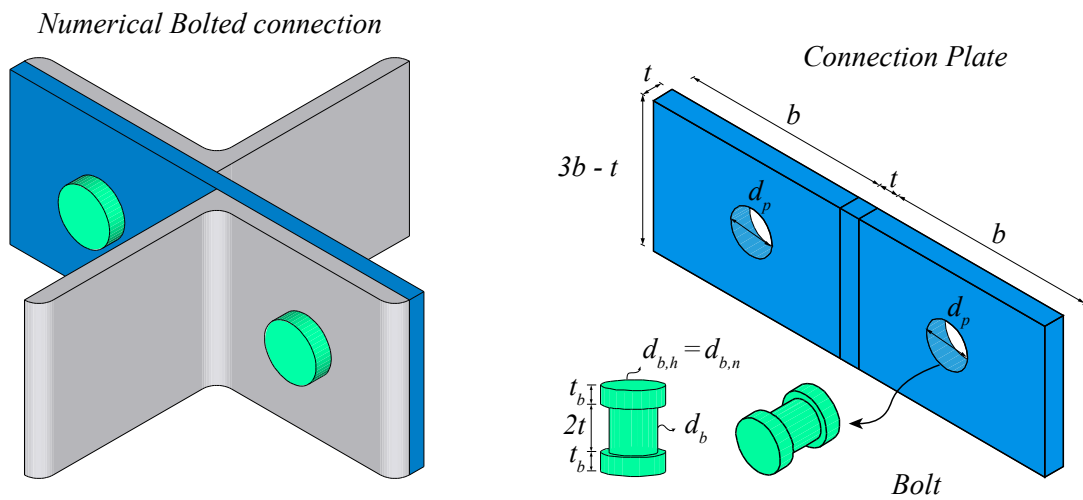


Figure 60: Finite element model bolt connection overview, including connection plate dimensions and bolt geometry.

6.2 Contact modelling at the bolt connection

In bolted joints employed in this work, three crucial contact interfaces are evident, as illustrated in Figure 61: the connection between the bolt head and the flange of the equal-leg angle column, the juncture between the flange of the equal-leg angle column and the plate, and the interface involving the bolt nut and the plate. Establishing these three contact interactions in ANSYS [29] software is pivotal for adequate transmitting forces between the bolts and the

⁶ It is considered that the threads have adequate strength for the applied load and can be omitted from the numerical simulation.

assembled components. Consequently, surface-to-surface contact elements *CONTA174* and *TARGE170* were used to capture the non-linear response in these contact regions.

CONTA174 has capabilities to define precisely the interface between contact structural components with parameter settings – such as *KEYOPT(2)*, *KEYOPT(4)*, *KEYOPT(10)*, and *KEYOPT(12)* – adjusted to dictate crucial aspects of the contact mechanic. In this work, these adjustments encompass the selection of the Augmented Lagrange method as the preferred contact algorithm, the specification that contact detection operates at the nodes of the contact elements rather than Gauss points, the prescription for contact stiffness updates to occur during each iteration, and the specification of the behaviour for contact surfaces, expressly permitting sliding without separation with friction coefficient (μ) assumed to be 0.3.

Complementing this, *TARGE170* enables the definition of target surfaces for the associated contact elements. Together, these two elements can simulate contact-induced forces and deformations, ensuring the accurate representation of inter-component interactions in the finite element model.

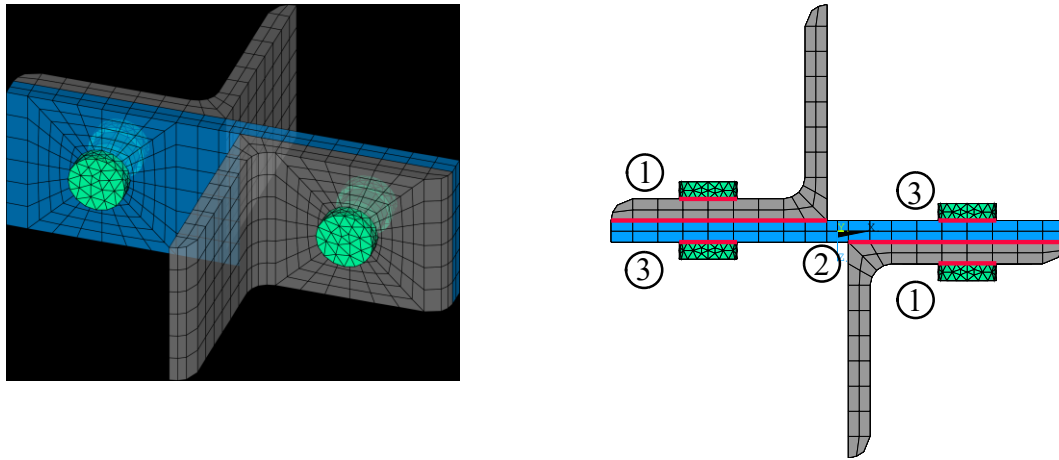


Figure 61: Three pairs of contact interactions: 1) the bolt head and the flange of the equal-leg angle column; 2) the plate and the equal-leg angle columns; 3) the bolt nut and the plate.

6.3 Bolt preload

The bolt used in the conducted tests [50] was not characterised, as its sole purpose was to guarantee the interaction between the two equal-leg angle sections, forming a unique starred

section. In this specific application, the bolt works primarily as a tightening mechanism rather than contributing structurally, ensuring the authentic behaviour of the starred columns, i.e., shear centre and centroid coincident.

Hence, the nominal characteristics of ASTM A490 bolts were included in the finite element model using a bilinear isotropic hardening stress-strain material behaviour (BISO in ANSYS [29]), characterised by Young's Modulus $E = 210000$ MPa, Poisson's ratio $\nu = 0.3$, yield strength $f_{y,b} = 940$ MPa, ultimate tensile strength $f_{u,b} = 1034.21$ MPa, and tangent modulus $E_T = 695$ MPa.

To establish the bolted connection, the bolts' preload was applied using a pretension procedure by the PSMESS command. This command creates the bolt pretension section and the corresponding meshes, inserting pretension elements PRETS179. Subsequently, the SLOAD command was employed to establish the pretension loads upon these created pretension sections, specified to be equivalent to 70% of the bolt's ultimate tensile strength ($f_{u,b} = 1034.21$ MPa) multiplied by the cross-sectional area of the bolt ($A_b = 126.67$ mm²) providing 91.70 kN. Figure 62 displays, for instance, the von-Mises stress distribution generated at the bolted connection due to the bolt preload application.

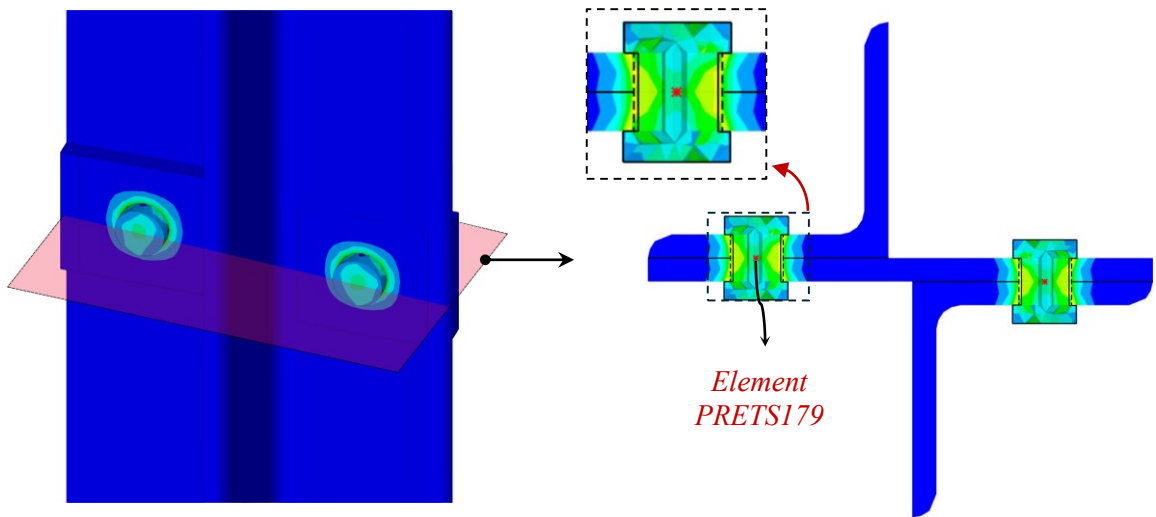


Figure 62: Numerical von Mises stresses at the bolt connection due to the bolt preload application.

6.4 Boundary conditions

The fixed supports were modelled by creating two point elements (MASS21) having six degrees of freedom – translations in x , y and z directions and rotations about the x , y and z axes – positioned at the bottom and top end sections centroid. Each node at the end section is connected to the corresponding point element, resulting in two distinct rigid regions (top and bottom). The boundary conditions were enforced by restraining the corresponding displacements and rotations of the nodes in all directions (x , y , and z), except for the column top axial displacement (UY) that was free – as depicted in Figure 63(a). At this stage, it is essential to emphasise that the cross-sections at the column ends are fully constrained, thereby preventing any cross-sectional torsional rotation and secondary warping.

6.5 Initial geometrical imperfection and residual stress

The column geometry, including initial geometrical imperfections, was generated following the same procedures used for welded starred columns in section 4.2. First, a linear buckling analysis was performed to determine the critical buckling mode shape (eigenvector). Subsequently, the “UPGEOM” command was used to update the perfect column geometry mesh to the actual mesh. This process corresponds to pure torsional buckling, characterized by a cross-section torsional rotation (β) about the longitudinal axis (y), with the maximum amplitude occurring at the cross-section located at mid-span ($L/2$), thereby constituting one half-wavelength with cross-section rigid-body rotation (β_0), as presented in Figure 63(b) with a scale amplified factor.

Regarding residual stress, it is well known in the available literature that its influence is negligible in equal-leg angle columns that fail due to flexural-torsional buckling [35],[60]. Additionally, the results obtained in section 5.5 revealed that the effect of residual stress is also negligible on the ultimate strength of austenitic and duplex stainless steel equal-leg angle welded starred columns, showing a reduction factor of up to 6.75% for duplex stainless steel columns and up to 4.3% for austenitic stainless steel ultimate strength columns. Therefore, considering the minor influence on the fixed-ended equal-leg angle welded starred columns’

ultimate strength – which represents the most critical assembly procedure scenario – this work did not account for the effect of residual stress in the finite element model.

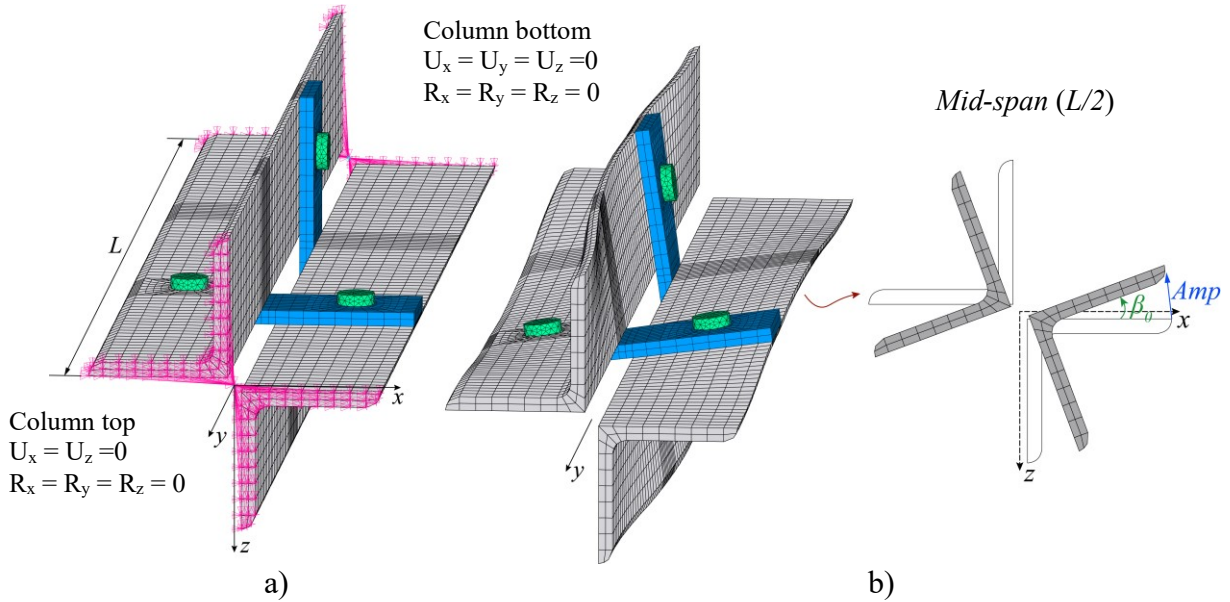


Figure 63: a) Bolted starred equal-leg angle columns boundary conditions and b) mid-span ($L/2$) cross-section torsional rotation – initial geometrical imperfection.

6.6 Analysis methodology and solution

The analysis methodology encompassed several key steps: (i) the definition of fixed-ended equal-leg angle bolted starred column mesh, (ii) establishing the contact modelling to define the behaviour between parts of the bolted joint, (iii) applying of the bolt preload, (iv) perform a linear buckling analysis, (v) introduction of initial geometrical imperfection by updating the column geometry to include the torsional buckling mode, (vi) uniform compression loading was applied using imposing a prescribed displacement (UY) at the centroid of the column's top end, and (vii) a nonlinear solution strategy was employed using an incremental-iterative approach based on the full Newton-Raphson algorithm. This comprehensive methodology accounted for both material and geometrical non-linearities.

Finally, a mesh convergence study was performed to ensure the accuracy of the numerical results. Different mesh configurations were considered, varying the element sizes from 10 mm to 4 mm. Based on the results, the finite element model discretisation used is a

finer mesh at the bolt connections with element sizes equal to 4 mm and 8 mm in other general parts provide an adequate correlation between numerical and experimental behaviour, requiring a fair computational effort.

7 BOLTED STARRED COLUMNS' ELASTIC BUCKLING BEHAVIOUR, FINITE ELEMENT MODEL VALIDATION, AND PARAMETRIC INVESTIGATION

7.1 Introduction

Two types of structural analyses were initially conducted to assess the fixed-ended bolted starred columns' stability, assuming an elastic material behaviour ($E = 210$ GPa and $\nu = 0.3$) and column geometries featuring a pair of compact equal-leg angle cross-section ($b/t < 20$). First, (i) a linear buckling analysis is performed, (i₁) to verify the columns assembly procedure, and (i₂) to identify column lengths susceptible to torsional buckling failure as the length increases. Based on the column buckling behaviour, i.e., “signature” curve, (ii) a nonlinear elastic post-buckling analysis is carried out to determine the columns' equilibrium paths as the length increases, evaluating the structural response of the fixed-ended bolted starred columns concerning geometrical non-linearity associated with torsional buckling failure mode. Afterwards, (iii) the austenitic stainless steel nonlinear material behaviour is incorporated into the finite element model to validate the numerical results by comparing them with the experimental results obtained by Botelho *et al.* [50]. Finally, (iv) a sensitivity study on initial torsional geometrical imperfections was conducted to assess their impact on these columns' ultimate strength.

Following the validation of the finite element model and the sensitivity study concerning the initial geometrical imperfections effect, (v) a parametric investigation was conducted to expand the database of numerical ultimate loads of austenitic and duplex stainless steel fixed-ended short-to-intermediate bolted starred columns, i.e., solely columns lengths that fail by torsional buckling – the main aim of this work.

7.2 Column buckling behaviour

The first step was to investigate the fixed-ended columns' buckling behaviour to obtain the “signature” curve (P_{cr} vs. L). Figure 64(a) shows the variation of the elastic buckling critical load (P_{cr}) obtained by ANSYS with the column length (L) – in logarithmic scale – for columns

with fixed ends created by a pair of bolted equal-leg angles cross-section $L63.50 \times 4.76$ ($b/t = 13.34$) and $L88.90 \times 4.76$ ($b/t = 18.68$), respectively. This elastic buckling analysis led to the following comments:

- i) Unlike fixed-ended welded starred columns, using plates at the $1/3L$ and $2/3L$ positions, adjusted according to cross-section geometry ($h_p = 3b-t$, $w_p = 2b+t$ and $t_p = t$), effectively ensures that the shear centre and centroid of the bolted starred columns remain coincident. This method significantly improves the columns' assembly procedure effectiveness and stability, leading to better overall structural performance;
- ii) For practical lengths ($L \geq 30$ cm), the signature curve of fixed-ended bolted starred columns reveals that (ii₁) there is no cross-section plate bending during buckling, (ii₂) all column lengths buckle in a single half-wave mode, and (ii₃) no local minimum is present. Consequently, the critical buckling deformation mode involves two rigid body movements depending on the column length, i.e., purely global buckling modes: pure torsion about the shear centre (as illustrated in Figure 64(b)) or major-axis displacement about the centroid (minor-axis bending);
- iii) Consequently, it is observed that across the entire investigated length range (30 cm to 1000 cm), the critical buckling load (P_{cr}) decreases as column length (L) increases. The results show two distinct branches indicating the critical global buckling modes: (iii₁) torsional buckling for short-to-intermediate column lengths and (ii₂) minor-axis flexural buckling for long and very long lengths. It is important to note that this elastic buckling behaviour is consistent with findings for fixed-ended columns with cruciform cross-sections [36] and welded equal-leg angle starred cross-sections demonstrated in section 4.3. Notably, the onset of minor-axis flexural critical buckling mode limits the torsional buckling mode, i.e., at a given column length referred to as the transition length, L_{TFS} , the elastic critical loads are equivalent ($P_{cr,T} = P_{cr,F}$);
- iv) Moreover, as the b/t ratio increases from 13.34 to 18.68, several key observations can be made: (iv₁) the transition length (L_{TFS}) also increases; (iv₂) the elastic critical buckling loads decrease; (iv₃) the elastic buckling behaviour remains consistent across different b/t ratios for compact cross-sections ($b/t < 20$), meaning the elastic buckling behaviour in fixed-ended bolted equal-leg angle columns maintains its pattern;

- v) Another crucial observation is to note that as the column's length extends from $0.30L_{TFS}$ up to $0.95L_{TFS}$, the relationship between the elastic critical torsional and minor-axis flexural buckling (highlighted in red dotted line) exhibits a substantial-high ratio ($P_{cr,F}/P_{cr,T}$) for 90% of column lengths (i.e., $L \leq 0.90L_{TFS}$). This pattern closely mirrors the behaviour noted in fixed-ended welded starred columns, suggesting that only a small range of column lengths may exhibit global interaction modes in the post-buckling analysis. However, these relationships will be further examined in 7.3;
- vi) Lastly, the elastic buckling analysis reveals that the bolted plate assembly procedure at one-third and two-thirds of their length ensures the actual columns' behaviour, regardless of the column geometry using compact equal-leg angle sections. This method consistently results in torsional buckling behaviour as the column length increases up to the transition length ($L \leq L_{TFS}$). For example, Figure 65 illustrates a column length range from $0.30L_{TFS}$ up to $0.95L_{TFS}$ considering columns created by a pair of bolted equal-leg angles $2L63.50 \times 4.76$, where $L_{TFS} = 2280$ mm.

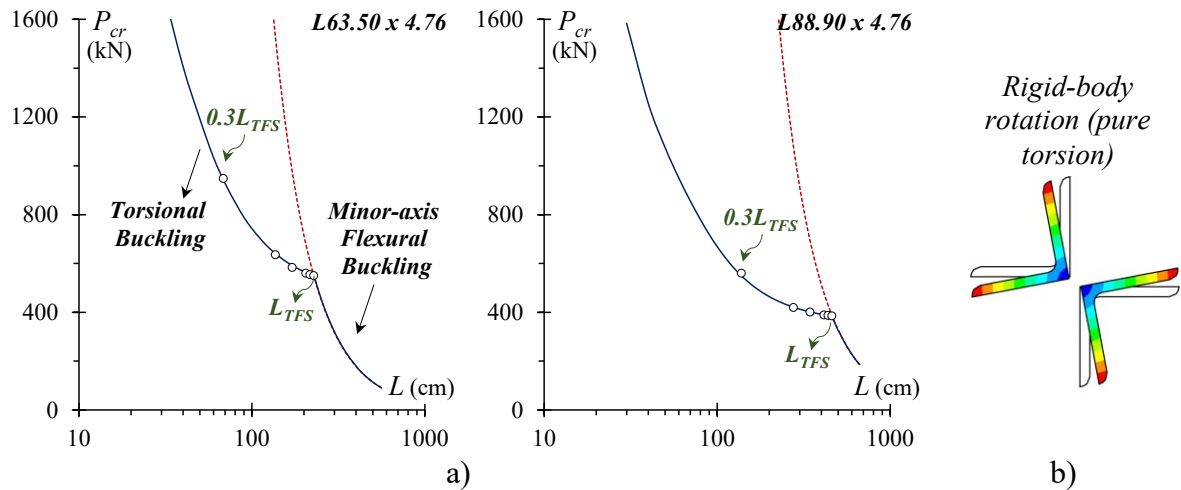


Figure 64: a) P_{cr} vs. L curves for columns with fixed ends created through two equal-leg angle b/t ratios of 13.34 and 18.64, respectively, and b) columns' mid-span ($L/2$) torsional buckling deformation.

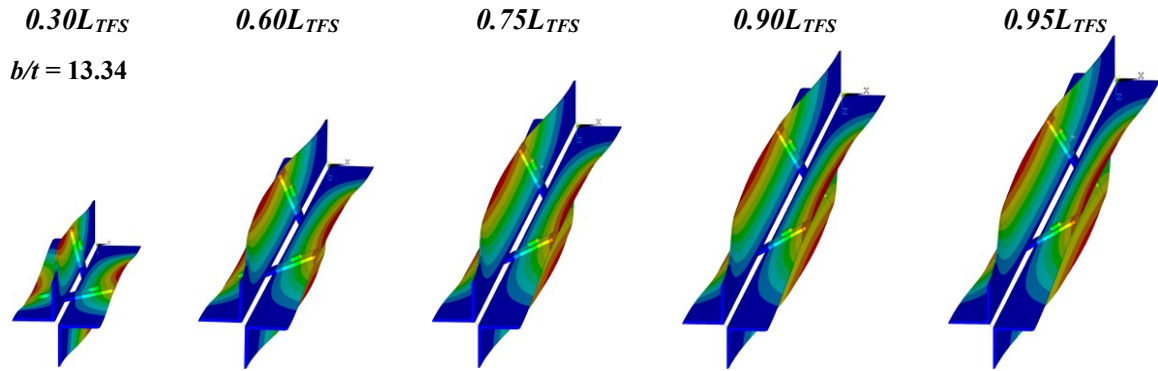


Figure 65: Torsional buckling failure mode shape for columns with lengths from $0.30L_{TFS}$ up to $0.95L_{TFS}$.

7.3 Column elastic post-buckling behaviour

Following the same strategy used for welded starred columns, five distinct column lengths with the same L/L_{TFS} ratio were investigated ($0.30L_{TFS}$, $0.60L_{TFS}$, $0.75L_{TFS}$, $0.90L_{TFS}$, and $0.95L_{TFS}$ – as depicted in Figure 64(a)) for each selected cross-section ($L63.50 \times 4.76$ and $L88.90 \times 4.76$). In this context, all columns considered torsional buckling critical mode initial geometrical imperfections with amplitudes equivalent to $0.1t$, yielding an initial mid-span rigid-body cross-section torsional rotation β_0 .

As mentioned, this approach is essential to determine the columns' mid-span equilibrium paths (P/P_{cr} vs. β) as the length increases along the signature curve, allowing for an in-depth investigation of potential global mode interactions (torsional and minor-axis flexural buckling). Figure 66 presents the results of the elastic post-buckling equilibrium paths for the selected columns. Therefore, the following observations can be made:

- i) The elastic post-buckling behaviour of fixed-ended columns exhibits nearly identical equilibrium paths as the width-to-thickness ratio (b/t) increases from 13.34 to 18.68 for column lengths with the same L/L_{TFS} ratio on the signature curve. This pattern indicates that the elastic post-buckling behaviour remains consistent regardless of the b/t ratio for compact cross-sections ($b/t < 20$);
- ii) Furthermore, it is important to note that all fixed-ended bolted starred columns also exhibit stable behaviour with substantial elastic post-buckling strength ($P > P_{cr,T}$). However, as the column lengths increase and approach the transition length, there is a noticeable decrease in post-buckling strength, although the load parameter ($P/P_{cr,T}$) always remains greater than unity. Notably, bolted starred

columns demonstrate higher post-buckling strength compared to welded starred columns, as evidenced by the comparison between Figure 48 and Figure 66;

- iii) Upon reaching the critical elastic torsional buckling load ($P = P_{cr,T}$), all columns' deformed configuration exclusively involves mid-span cross-section rigid-body rotations, with no centroid displacements observed. To illustrate this behaviour, Figure 67 presents isometric and top views showing the evolution of the deformed configuration from 0.1 to 0.5 rad in the most critical column investigated in this work with a length of $0.95L_{TFS}$, composed of a pair of bolted equal-leg angle $2L88.90 \times 4.76$, highlighting the position of each deformed state along the column's equilibrium path;
- iv) Consequently, it is observed that short-to-intermediate fixed-ended columns show no interaction between the two global critical modes (torsional and minor-axis flexural buckling), even when subjected to large deformations ($\beta = 0.6$ rad). Given this, it can be concluded that the short-to-intermediate bolted starred columns examined in this study fail exclusively by torsional buckling.

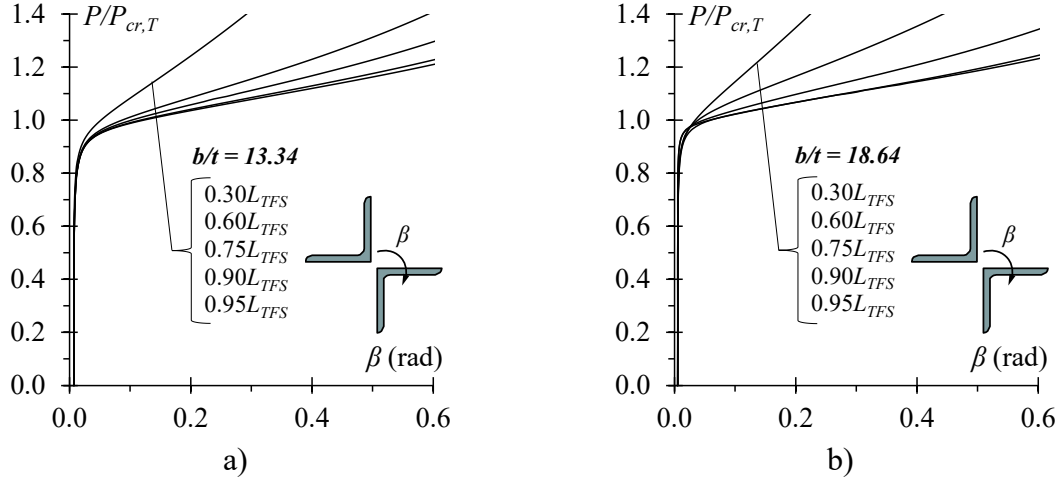


Figure 66: Fixed-ended bolted starred columns equilibrium paths P/P_{cr} vs. β created through equal-leg angle cross-section with a) $b/t = 13.34$ and b) $b/t = 18.64$.

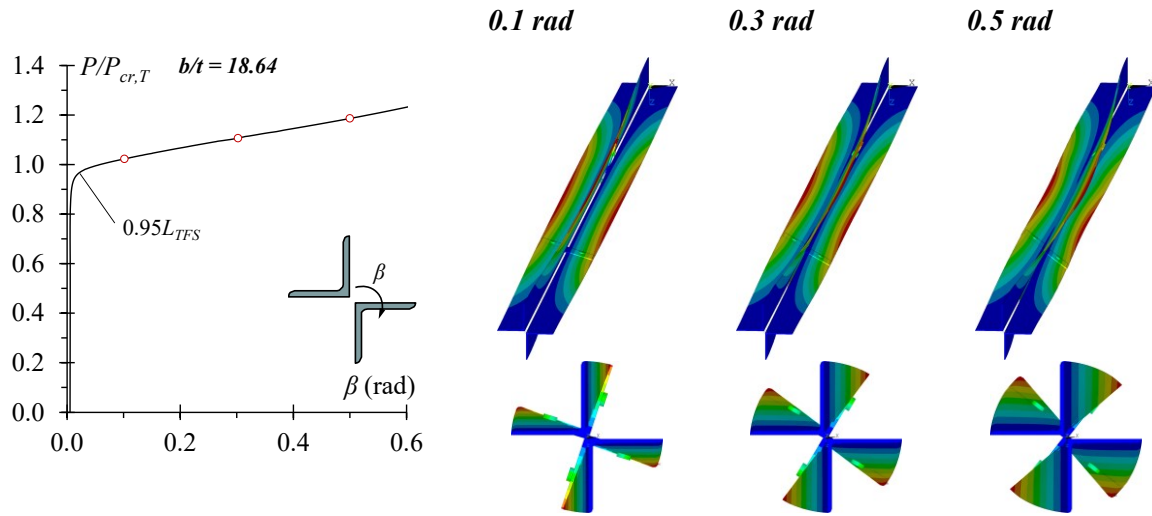


Figure 67: $P/P_{cr,T}$ vs β equilibrium path for fixed-ended bolted starred columns with length equal to $0.95L_{TFS}$ and three columns deformed configuration as the cross-section torsional rotation increases from 0.1 to 0.5 rad.

7.4 Numerical model validation – stainless steel material behaviour

Following the same methodology used in the welded starred columns, the next step involves incorporating the experimental non-linear stress-strain behaviour of austenitic stainless steel, obtained by Botelho *et al.* [50] and presented in Figure 50. This approach aims to evaluate the accuracy and validate the finite element model by comparing it against the experimental results, including (i) columns' ultimate load (P_u), (ii) load versus axial shortening curves (P vs Δ_y), (iii) load versus transverse displacements (P vs Δ_x and P vs Δ_z), and (iv) failure modes.

Figure 68 and Figure 69 compare the experimental data with the numerical outcomes for fixed-end bolted starred columns. The following observations arise from these validation results:

- i) When examining the ultimate loads of the columns, there is a satisfactory correlation between the experimental and numerical results, with a minor discrepancy of 3.87%. The numerical ultimate load was 653.64 kN, while the experimental load was 680.08 kN;
- ii) As shown in Figure 68(a), quantitative analysis shows that the initial axial stiffness (during the linear stage) between the equilibrium paths differs by

approximately 0.05%, as indicated by the slope difference between experimental and numerical results. Moreover, the difference in post-buckling behaviour remains below 1% until reaching an axial displacement $\Delta_y = 7\text{mm}$. These results demonstrate a suitable correlation between the experimental and numerical axial shortening curves (P vs. Δ_y);

- iii) A more significant disparity is observed in transverse displacements (Δ_x and Δ_z), with the maximum discrepancy reaching 9% at (LVDT) V7 – Figure 68(b) – following a large displacement of $\Delta_x = -20\text{mm}$. It is important to note that LVDT measurements at the mid-span ($L/2$) may show deviations due to slip during the load application phase. Nonetheless, the finite element model satisfactorily defines these transverse equilibrium paths as well, showing the mid-span rigid-body rotation;
- iv) Figure 69 compares the experimental and numerical failure modes, highlighting the notable agreement in the deformed shape of the columns, which reproduces the torsional global buckling behaviour;
- v) Finally, it can be confirmed that the FEM accurately replicates the behaviour of fixed-ended stainless steel bolted starred columns prone to torsional buckling failure mode in terms of ultimate failure load, equilibrium paths, and failure mode.

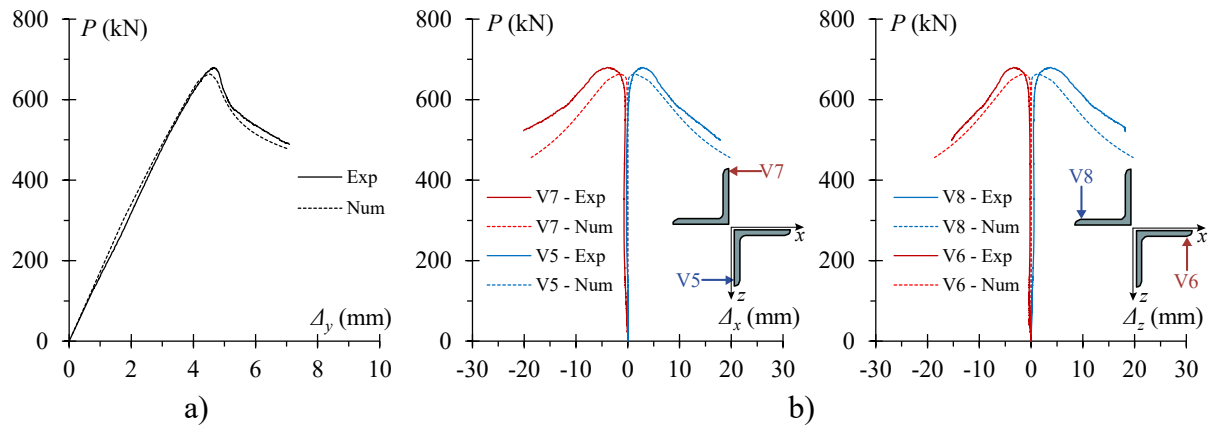


Figure 68: Finite element model validation comparing the column's equilibrium path: a) load versus axial shortening curves (P vs. Δ_y) and b) load versus transverse displacements (P vs. Δ_x and P vs. Δ_z).

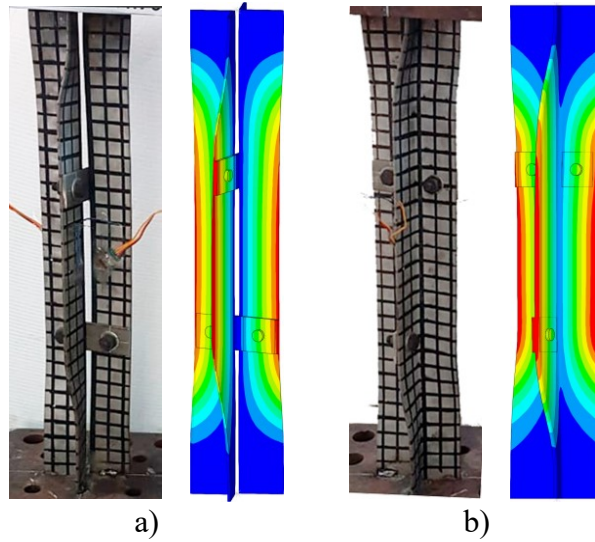


Figure 69: Finite element model validation comparing the column's failure mode through two viewpoints.

7.5 Initial geometrical imperfection sensitivity

The sensitivity study on the initial geometrical imperfection of fixed-ended stainless steel bolted star columns' ultimate strength involves comparing the numerical ultimate loads ($P_{u,FE}$) and the load *vs.* axial shortening curves (P *vs.* Δ_y). Consequently, five different amplitude values are considered for the initial torsional rotation of the mid-span cross-section (β_0), specifically $t/20$, $t/10$, $t/5$, $t/2.5$, and t , as illustrated in Figure 63(b).

The effect of the initial geometrical imperfection amplitude on the columns' ultimate strength is assessed using the measured imperfection amplitude from the experimental column geometry as a reference, i.e., the validation study (VS) – L63.50 \times 4.76, $L = 700$ mm, and $t/13.64$. The next stage extends this analysis to assess the effect on two additional intermediate columns as the length increases to 1400 mm and 2100 mm, covering a range from $0.30L/L_{TFS}$ to $0.92L/L_{TFS}$ – the main aim of this work ($L \leq L_{TFS}$).

Table 11 provides the adopted amplitudes of the initial geometrical imperfections, the mid-span cross-section torsional rotation, and the ultimate loads for each column. Furthermore, Figure 70 presents the load versus axial shortening curves (P *vs.* Δ_y) for each initial geometrical imperfection in the selected columns. From these results, several key observations can be made:

- i) As foreseen, the ultimate loads decrease as the initial geometrical imperfection increases. This reduction is most noticeable when comparing the smallest ($t/20$)

and largest (t) initial geometrical imperfection amplitude values. For column lengths of 700 mm and 1400 mm, the ultimate load decreases by up to 17%, while for a column length of 2100 mm, the reduction is 15%;

- ii) The decrease in ultimate load is significantly less pronounced within the amplitude range of $t/20$ to $t/2.5$, with a maximum reduction of 9% for the 1400 mm column. Comparing the amplitudes of $t/20$ and $t/5$ reveals a maximum reduction of 6% in the ultimate load;
- iii) These comparisons highlight the necessity of a substantial increase in the initial geometrical imperfection amplitude value to influence the column's ultimate load consistently. Specifically, an increase of nearly 20 times ($t/20$ to t) in the initial geometrical imperfection amplitude is required for this influence to become statistically significant;
- iv) Additionally, Figure 70 shows that for the most significant initial geometrical imperfection amplitude values ($t/2.5$ and t), a deviation in the column's equilibrium path load vs. axial shortening curves (P vs Δ_y) is noted. These outcomes suggest that using a high initial geometrical imperfection value might lead to a misinterpretation of the ultimate strength and, consequently, the structural element's behaviour;
- v) Generally, as observed in Table 11 and Figure 70, initial geometrical imperfection amplitudes of $t/20$ and $t/10$ provide (v_1) an adequate correlation with the column's ultimate load and (v_2) equilibrium path for each selected length, mitigating the reduction in column resistance while ensuring a satisfactory non-linear response;
- vi) Indeed, as mentioned in 4.6, an initial geometrical imperfection amplitude of $t/10$ (highlighted in blue) is commonly used in previous studies on fixed-ended short-to-intermediate columns that fail by torsional buckling with cruciform sections and welded equal-leg angle starred sections (in this work), consistently yielding satisfactory results. Therefore, based on these observations and in alignment with previous works available in the literature, an initial geometrical imperfection amplitude of $t/10$ is adopted for the parametric analysis developed in the next section.

Table 11: Initial geometrical imperfection sensitivity study for fixed-ended stainless steel bolted starred columns ranging from $0.30L/L_{TFS}$ to $0.92L/L_{TFS}$.

Column	Amplitude	β_0 (rad)	$P_{u,FE}$ (kN)
L63.50 × 4.76 – 700 mm	t/13.64 – VS	0.0055	653.64
	t/20	0.0037	658.48
	t/10	0.0075	648.82
	t/5	0.0149	632.34
	t/2.5	0.0299	605.16
	t	0.0748	550.40
L63.50 × 4.76 – 1400 mm	t/20	0.0037	591.92
	t/10	0.0075	580.94
	t/5	0.0149	554.94
	t/2.5	0.0299	536.54
	t	0.0748	491.72
L63.50 × 4.76 – 2100 mm	t/20	0.0037	555.08
	t/10	0.0075	542.13
	t/5	0.0149	532.42
	t/2.5	0.0299	512.95
	t	0.0748	476.69

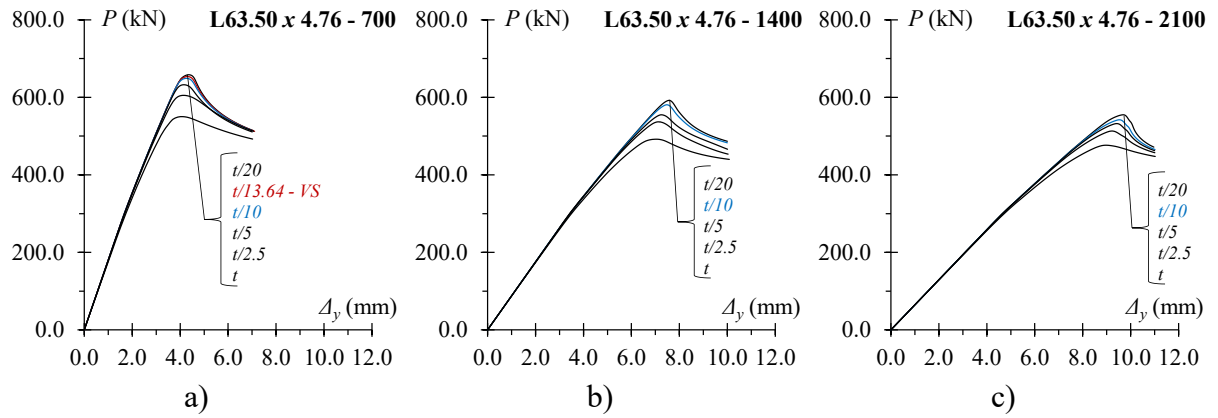


Figure 70: Load vs axial shortening curves (P vs Δ_y) concerning each initial geometrical imperfection amplitude for fixed-ended bolted starred columns with a length equal to a) 700 mm, b) 1400 mm, and c) 2100 mm.

7.6 Numerical parametric investigation

A parametric investigation was carried out through the following steps: (i) incorporating the behaviour of austenitic and duplex stainless steel derived from experimental tests; (ii)

selecting appropriate cross-section profiles ($b/t < 20$); (iii) choosing column lengths based on elastic buckling analysis ($L \leq L_{TFS}$); (iv) applying an initial geometrical imperfection with an amplitude equal to $t/10$; and (v) performing nonlinear analysis to determine the numerical ultimate load ($P_{u,FE}$) of fixed-ended short-to-intermediate bolted starred columns.

As detailed in section 5.2, the stress-strain curves for austenitic and duplex stainless steel used in the finite element model were obtained from tensile tests conducted by Sarquis *et al.* [45] for austenitic stainless steel and Afshan *et al.* [3] for duplex stainless steel. Twelve equal-leg angle cross-sections were selected explicitly centred on compact sections, i.e., $b/t < 20$, to assess the ultimate loads of fixed-ended short-to-intermediate bolted starred columns. The column lengths for each bolted starred cross-section were chosen based on their elastic buckling behaviour, with lengths limited by the transition length in the signature curve ($L \leq L_{TFS}$). Table 12 provides detailed information on the cross-section identification (ID), width/thickness ratios (b/t) ranging from 5 to 18.68, and the selected lengths (L), which span from 300 mm up to the transition length (L_{TFS}) in 100 mm increments. It is essential to emphasize that the same column lengths were evaluated for each material, resulting in a total of 488 finite element models. These models are designated as A for austenitic stainless steel columns and D for duplex stainless steel columns.

Table 12: Typical compact cross-section dimensions and lengths selection for parametric analysis.

<i>ID</i>	<i>Cross-section</i>	<i>b/t</i>	<i>A_g</i> (mm ²)	<i>L</i> (mm)	<i>Austenitic columns</i> (<i>A</i>)	<i>Duplex columns</i> (<i>D</i>)
<i>S1</i>	63.50x12.70	5.00	2830.64	300 – 810	7	7
<i>S2</i>	76.20x12.70	6.00	3475.80	300 – 920	8	8
<i>S3</i>	63.50x9.53	6.66	2198.11	300 – 1060	9	9
<i>S4</i>	101.60x12.70	8.00	4766.12	300 – 2140	20	20
<i>S5</i>	57.16x6.35	8.99	1353.07	300 – 1460	13	13
<i>S6</i>	76.20x7.94	9.60	2265.65	300 – 1950	18	18
<i>S7</i>	63.50x6.35	10.00	1516.34	300 – 1660	15	15
<i>S8</i>	76.20x6.35	12.00	1836.69	300 – 2630	25	25
<i>S9</i>	63.50x4.76	13.34	1153.53	300 – 2280	21	21
<i>S10</i>	69.85x4.76	14.67	1274.43	300 – 3260	31	31
<i>S11</i>	76.20x4.76	16.01	1395.34	300 – 3890	37	37
<i>S12</i>	88.90x4.76	18.68	1637.14	300 – 4160	40	40

Figure 71 provides a graphical summary of the parametric analysis results in terms of the ratio of the numerical ultimate load and squash load ($P_{u,FE}/A_g\sigma_{0.2\%}$) – with non-dimensional torsional slenderness ($\lambda_T = [(A_g\sigma_{0.2\%})/P_{cr,T}]^{0.5}$) covering a range from 0.19 to 1.60. Additionally,

it includes the design buckling curves from Eurocode 3: Part 1.4 [4], specifically curve “b” (appropriate for torsional buckling curve), “a₀”, and curve “a”. The observation of all these results allows the following conclusions:

- i) When considering identical column geometry, the variations in non-dimensional torsional slenderness λ_T directly correlate with the materials’ 0.2% proof stress ($\sigma_{0.2\%A} = 348$ MPa and $\sigma_{0.2\%D} = 548$ MPa). In other words, modifying the proof stress ($\sigma_{0.2\%}$) leads to a corresponding adjustment in the non-dimensional slenderness, thus extending the scope of the investigation and encompassing a more comprehensive range. For example, in the case of columns featuring the *S9* cross-section, the non-dimensional slenderness for austenitic stainless steel columns varies from 0.47 to 0.81, while for duplex stainless steel columns, it ranges from 0.64 to 1.15;
- ii) Moreover, as depicted in Figure 72, exemplified by the *S4*, *S9*, and *S12* cross-sections, it is evident that the results consistently display a complementary relationship between fixed-ended austenitic and duplex stainless steel columns prone to failure by torsional buckling mode. This observation signifies a continuous pattern of columns’ ultimate strength with the increasing of the non-dimensional torsional slenderness, reflecting the increased materials’ resistance strategy to cover a more comprehensive non-dimensional slenderness range;
- iii) Based on the non-dimensional torsional slenderness values covered in this work, two distinct column failure modes are evident: (iii₁) gross cross-section yielding occurs for columns with normalised slenderness up to 0.56, while (iii₂) column failure due to torsional buckling becomes apparent beyond this threshold;
- iv) Notably, columns composed of sections *S1* through *S7* (with b/t ratios ranging from 5 to 10) predominantly experience gross cross-section yielding failure. In these cases, the numerical failure load exceeds or equals the squash load ($P_{u,FE}/A_g\sigma_{0.2\%} \geq 1$), with a ratio reaching 1.27. This phenomenon can be attributed to stocky columns constructed from compact sections possessing a significantly high elastic critical torsional buckling load, causing cross-section yielding to precede column torsional buckling failure ($P_{cr,T} \gg A_g\sigma_{0.2\%}$). These findings also underscore the strain-hardening capacity of austenitic and duplex stainless steel;
- v) Similarly, the torsional buckling failure mode becomes predominant from the point of $\lambda_T = 0.56$ onward, i.e., ($P_{u,FE}/A_g\sigma_{0.2\%} < 1$). This transition denotes a

gradual decrease in columns' resistance of up to 52%, which is established by the ratio $P_{u,FE}/A\sigma_{0.2\%} = 0.48$ for the normalised torsional slenderness equal to 1.60;

- vi) As columns with closely matched torsional slenderness values display nearly identical ultimate strengths, it becomes apparent that this parameter is a practical and convenient metric for constructing a design column buckling curve, i.e., the design curve proves to be effective in predicting the load-carrying capacity of columns susceptible to torsional buckling failure. This observation is particularly evident when compared to the three curves established by Eurocode 3: Part 1.4 [4], specifically “ a_0 ”, “ a ”, and “ b ”;
- vii) Moreover, regardless of stainless steel type (austenitic or duplex), columns with similar non-dimensional torsional slenderness (λ_T) values present similar behaviour and normalised ultimate strengths. Therefore, it means that the design standard preconised in Eurocode 3: Part 1.4 [4] is satisfactory for setting a unique design column buckling curve in order to forecast the ultimate strength of short-to-intermediate fixed-ended stainless steel columns subjected to torsional buckling, i.e., curve “ b ” specific to the torsional buckling phenomenon since providing a conservative design.

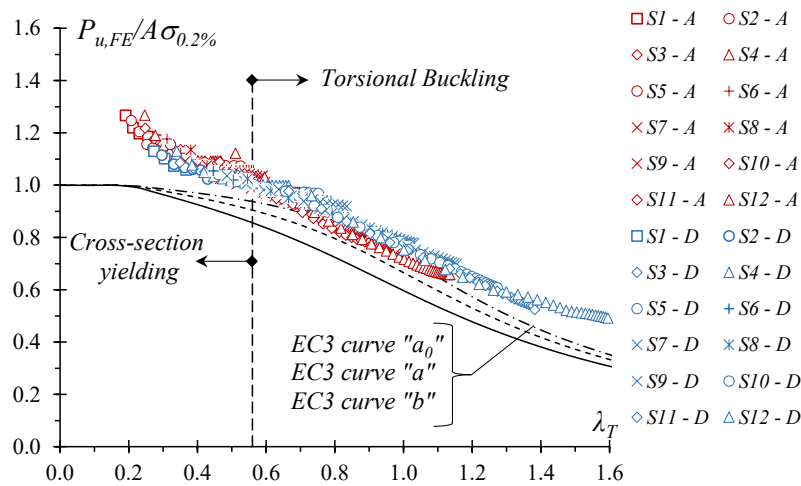


Figure 71: Numerical results compared to buckling curves “ a_0 ”, “ a ”, and “ b ” for stainless steel columns torsional buckling failure mode.

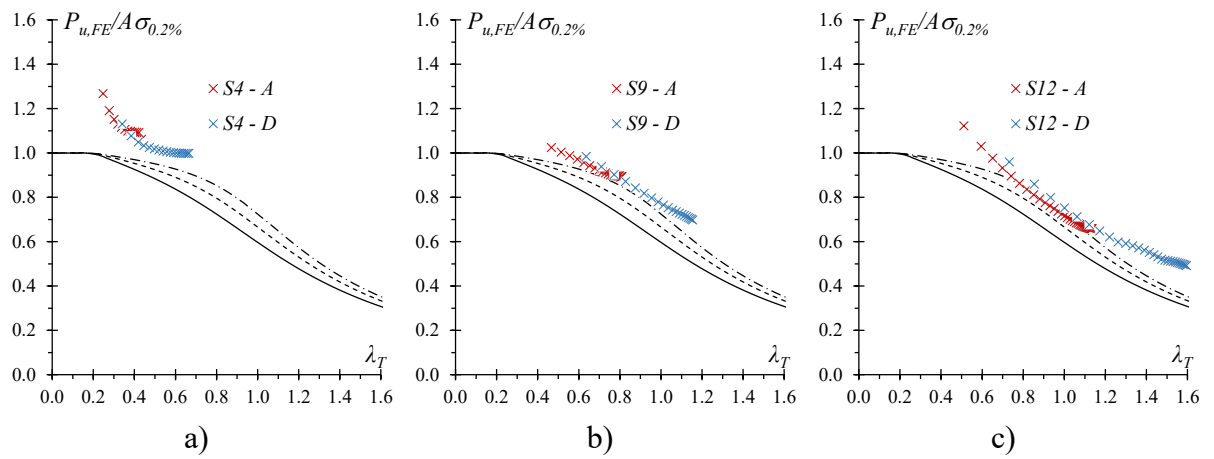


Figure 72: Continuous normalised ultimate strength pattern as non-dimensional torsional slenderness increases considering the austenitic and duplex stainless steel for a) S4, b) S9, and S12 cross-sections.

8 EUROCODE 3: PART 1.4 COLUMNS' DESIGN ASSESSMENT

8.1 Introduction

This section assesses the design rules for austenitic and duplex stainless steel fixed-ended welded and bolted starred columns established in the European standard code for structural stainless steel – Eurocode 3: Part 1.4 (EN 1993-1-4) [4]. The European code design guidelines check the buckling ultimate limit state from the cross-section classification, cross-section resistance, and structural member buckling resistance.

A preliminary cross-section classification (class 1 up to 4) is initially required to determine the susceptibility to local buckling according to the maximum width-to-thickness ratio (b/t) of elements in compression. At this point, it is essential to emphasise that there is no classification for cruciform, welded or bolted starred cross-sections. However, equal-leg angles cross-section can be classified as class 3 or 4, limiting class 3 to a ratio of up to 11.5ε . So, the resistance of class 4 cross-sections ($b/t > 11.5\varepsilon$) is reduced using effective widths elements, i.e., due to local buckling occurrence, the gross cross-section area (A_g) is reduced to an effective area (A_{eff}) through a reduction factor (ρ).

For the resistance of structural members in axial uniform compression (columns), the column buckling curve “b” determines the resistance of all columns susceptible to torsional buckling and is defined by the non-dimensional slenderness limit ($\lambda_0 = 0.2$) and the imperfection factor ($\alpha = 0.34$).

8.2 Fixed-ended short-to-intermediate stainless steel welded starred columns

Table 13 shows the classification of equal-leg angle cross-sections according to the materials (austenitic and duplex) and effective area (A_{eff}). It can be noted that (i) except for austenitic *S1* to *S6* and duplex *S1* to *S3*, all other cross-sections are classified as class 4 due to a high value of 0.2% proof stresses (Table 7) and low cross-sections b/t ratio, (ii) showing a reduction of 49% in the gross cross-section area for duplex stainless steel *S12* ($855.18/1659.80 = 0.51$).

Figure 73(a) and Table 14 show the assessment of Eurocode 3: Part 1.4 [4] design approach by comparing the numerical failure load ($P_{u,FE}$) against the non-factored design torsional buckling resistance forecast ($P_{u,EC3}$). The observation of the comparison prompts the following conclusions:

- i) The results reveal that column buckling curve “b” – specific for torsional buckling – yields a high conservatism and scatter in the torsional buckling resistance forecast of fixed-ended welded starred austenitic and duplex stainless steel columns. The quantitative examination in Table 14 corroborates this comment, where the maximum value is 2.39, the minimum is 1.14, and the mean ratio is 1.56, with the coefficient of variation (CoV) equal to 0.24 – showing excessive inaccuracy in the design;
- ii) As seen in elastic buckling behaviour, it is verified that the cross-section classification is inappropriate, i.e., the local buckling does not occur in fixed-ended welded starred columns. Therefore, this inaccurate classification contributes to the high level of conservatism in the design, as it results in an overly conservative estimation of the cross-section resistance ($A\sigma_{0.2\%}$) directly related to the non-dimensional torsional slenderness – as shown in Eq. (57). For instance, Figure 59 and Figure 73(a) depicts the reduction in non-dimensional torsional slenderness (λ_T) from 1.56 to 1.12 due to the effective area;
- iii) Following the design steps used in the European standard code, the first recourse for less conservatism in torsional buckling resistance is to maintain the cross-section classification, i.e., $A = A_g$ or A_{eff} ; and to change the column buckling curve “b” for the column buckling curve “a0” adopted for high-strength steels. This strategy decreases the imperfection factor from $\alpha = 0.34$ to $\alpha = 0.13$ and, consequently, a higher torsional strengths forecast. Figure 73(b) shows the results of this approach using buckling curve “a0”, demonstrating a general improvement in the torsional buckling resistance forecast. It is possible to note in Table 14 that there is a widespread quantitative reduction, i.e., the maximum ratio value reduced by 21% (2.39/1.98), and the new mean ratio of 1.35 shows a CoV equal to 0.16, revealing the design improvement just adjusting the type of column buckling curve;
- iv) However, another alternative for a more reliable and less conservative design is adopting the column buckling curve “a0” and no cross-section classification, i.e., permanently $A = A_g$. So, it is possible to define the actual torsional column

behaviour (no local buckling), assuming a minor imperfection factor ($\alpha = 0.13$). As seen in Figure 73(c), compared with the established steps in the European standard code – Figure 73(a), this strategy yielded a more precise torsional buckling resistance forecast across the entire natural range of non-dimensional torsional slenderness (0.26 to 1.56). Table 14 depicts a reduction in the mean ratio from 1.56 to 1.21 with a CoV equal to 0.10, which indicates a more reliable and accurate design. Moreover, it is essential to highlight that all strengths forecasts are in the safe zone ($P_{u,FE}/P_{u,EC3} \geq 1$).

Table 13: Classification of cross-section, gross area (A_g) and effective area (A_{eff}).

<i>ID</i>	<i>b/t</i>	A_g (mm ²)	<i>Austenitic Class</i>	A_{eff} (mm ²)	<i>Duplex Class</i>	A_{eff} (mm ²)
<i>S1</i>	5.00	2991.93	3	-	3	-
<i>S2</i>	6.00	3637.09	3	-	3	-
<i>S3</i>	6.66	2288.93	3	-	3	-
<i>S4</i>	8.00	4927.41	3	-	4	4838.70
<i>S5</i>	8.99	348.87	3	-	4	326.59
<i>S6</i>	9.60	2328.70	3	-	4	2078.63
<i>S7</i>	10.00	1554.43	4	1532.26	4	1345.16
<i>S8</i>	12.00	1877.01	4	1854.84	4	1407.74
<i>S9</i>	13.34	1176.19	4	1080.30	4	809.48
<i>S10</i>	14.67	1297.09	4	1110.41	4	823.14
<i>S11</i>	16.01	1417.99	4	1134.22	4	835.35
<i>S12</i>	18.68	1659.80	4	1173.40	4	855.18

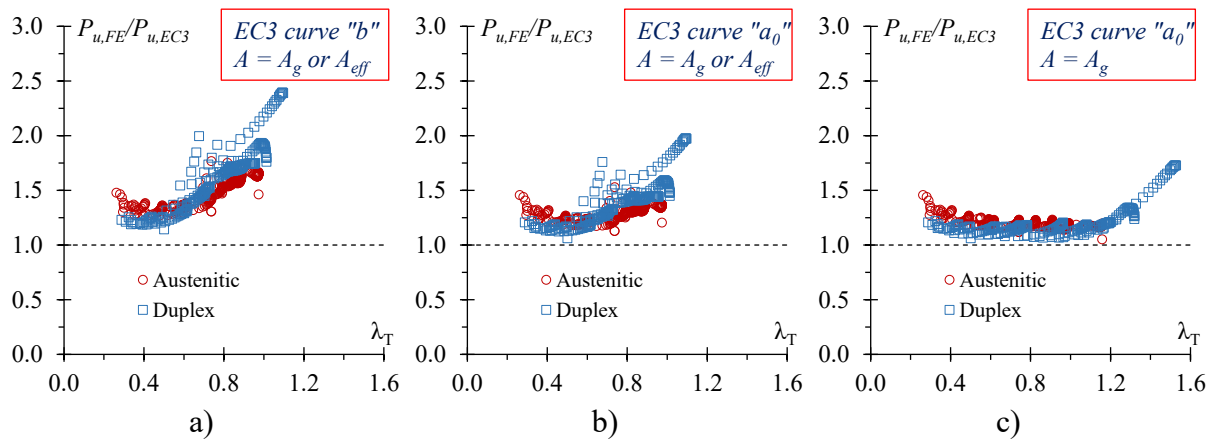


Figure 73: Welded starred columns comparison of numerical results with Eurocode 3: Part 1.4 [4] a) column buckling curve “b”, b) column buckling curve “a₀”, and c) column buckling curve “a₀” using A_g .

Table 14: Welded starred columns strengths comparison summary ($P_{u,FE}/P_{u,EC3}$).

	<i>EC3 Curve</i> “ <i>b</i> ” $A = A_g \text{ or } A_{eff}$	<i>EC3 Curve</i> “ <i>a₀</i> ” $A = A_g \text{ or } A_{eff}$	<i>EC3 Curve</i> “ <i>a₀</i> ” $A = A_g$
<i>Maximum</i>	2.39	1.98	1.73
<i>Minimum</i>	1.14	1.06	1.05
<i>Mean</i>	1.56	1.35	1.21
<i>CoV</i>	0.24	0.16	0.10

8.3 Fixed-ended short-to-intermediate stainless steel bolted starred columns

Table 15 shows the gross cross-section area, the classification of cross-sections according to each material, and the respective effective area. It can be noted that the classification of cross-sections differs based on the material employed, attributed to differences in the values of 0.2% proof stress and Young’s Modulus for each material. Six sections (*S7* to *S12*) and nine sections (*S4* to *S12*) are classified as class 4 for austenitic and duplex material, respectively. This classification reduces the cross-section geometrical properties, notably observed in the gross cross-section area for duplex stainless steel *S12*, undergoing a decrease of up to 46.80% ($870.96/1637.14 = 0.53$).

Table 15: Eurocode 3: Part 1-4 [4] – cross-section classification, gross area (A_g) and effective area (A_{eff}).

<i>ID</i>	<i>b/t</i>	<i>A_g</i> (mm ²)	<i>Austenitic Class</i>	<i>A_{eff}</i> (mm ²)	<i>Duplex Class</i>	<i>A_{eff}</i> (mm ²)
<i>S1</i>	5.00	2830.64	3	-	3	-
<i>S2</i>	6.00	3475.80	3	-	3	-
<i>S3</i>	6.66	2198.11	3	-	3	-
<i>S4</i>	8.00	4766.12	3	-	4	4766.12
<i>S5</i>	8.99	1353.07	3	-	4	1289.48
<i>S6</i>	9.60	2265.65	3	-	4	2064.01
<i>S7</i>	10.00	1516.34	4	1516.34	4	1340.44
<i>S8</i>	12.00	1836.69	4	1836.69	4	1412.41
<i>S9</i>	13.34	1153.53	4	1073.94	4	815.54
<i>S10</i>	14.67	1274.43	4	1107.48	4	832.20
<i>S11</i>	16.01	1395.34	4	1134.41	4	846.97
<i>S12</i>	18.68	1637.14	4	1178.74	4	870.96

Figure 74(a) and Table 16 show the assessment of the Eurocode 3: Part 1.4 [4] design methodology. This evaluation compares the ratio between the numerical failure load ($P_{u,FE}$) and the non-factored EC3 design torsional buckling resistance forecast ($P_{u,EC3}$) plotted against the member's buckling non-dimensional torsional slenderness λ_T . The observation of this comparison results leads to the following conclusions:

- i) These results indicate that the design approach employed by Eurocode 3 for (austenitic and duplex) stainless steel fixed-ended bolted starred columns susceptible to torsional buckling yields a conservative forecast of ultimate strengths. In other words, combining cross-section classification and design buckling curve "b" excessively reduces the columns' resistance. The quantitative analysis in Table 16 reinforces this observation, showing a maximum ratio value of 2.08 and a mean of 1.39. Also, the coefficient of variation (CoV) is 0.20, highlighting a significant level of scatter and inaccuracy in the established design;
- ii) According to the columns' elastic buckling behaviour, the cross-section class 4 is inappropriate for fixed-ended bolted starred columns. As previously presented, local buckling does not occur regardless of the cross-section geometry (i.e., $b/t \leq 20$). This misclassification significantly contributes to the high conservatism observed in the Eurocode 3 design methodology by reducing the cross-section resistance ($A\sigma_{0.2\%}$) through the effective area (A_{eff});
- iii) As shown in Table 15, the selected cross-sections may exhibit reductions in resistance of up to 46.80% for duplex stainless steel. Moreover, this classification also directly influences the columns' non-dimensional torsional slenderness values (λ_T), leading to a reduction in this crucial design parameter from 1.60 to 1.18;
- iv) For this reason, the initial approach to mitigate the conservatism in the Eurocode 3 resistance forecast – for stainless steel fixed-ended bolted starred columns susceptible to torsional buckling – is considering all cross-sections as class 3, i.e., the cross-section resistance ($A\sigma_{0.2\%}$) is always calculated using its gross area ($A = A_g$). Consequently, an essential adjustment in the design is implemented based on the columns' actual structural buckling behaviour;
- v) Figure 74(b) presents the outcomes of this approach, revealing a notable improvement in the torsional buckling resistance forecast. This strategy leads to a more aligned design with the buckling phenomenon investigated in this work,

i.e., without reducing the columns' non-dimensional torsional slenderness (λ_T), covering the original range from 0.19 to 1.60. Additionally, Table 16 shows the modified design enhancement through the quantitative analysis, with the maximum ratio value decreasing by 23% (2.08/1.59) and the mean ratio reaching 1.25, accompanied by a lower coefficient of variation (CoV) equal to 0.09. These values emphasise the improved design achieved through a straightforward adjustment based on the columns' structural behaviour;

- vi) However, these findings also indicate that column buckling curve “b” still presents a considerable conservatism in design forecasting. It is noted that the resistance of fixed-ended bolted starred austenitic and duplex stainless steel columns decreased up to 59%. Consequently, further improvements in predicting these columns' resistance may be achieved by applying the same strategy (all cross-sections class 3) but changing curve “b” with others provided in the Eurocode 3, specifically curves “a” and “a₀”.

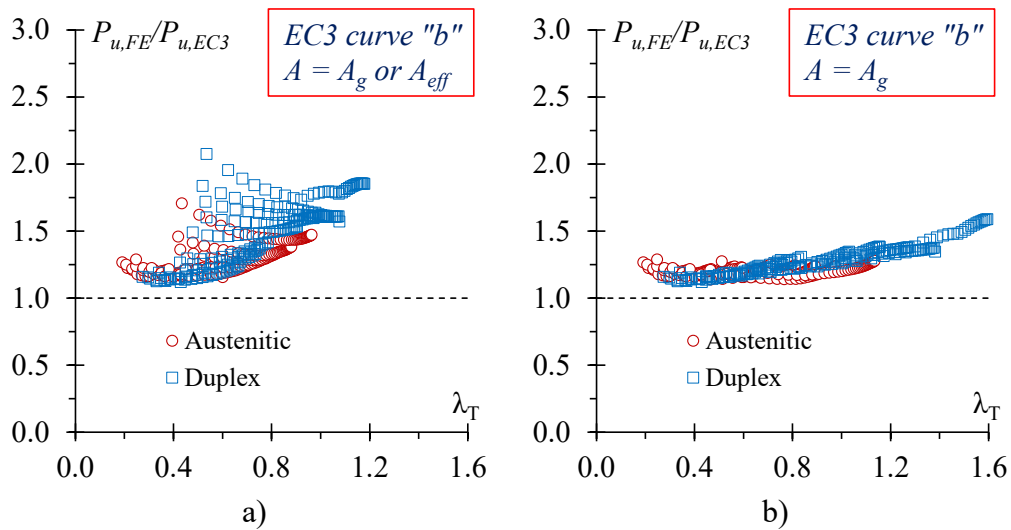


Figure 74: Bolted starred columns comparison of numerical results with Eurocode 3: Part 1.4 [4] a) column buckling curve “b” using $A = A_g$ or A_{eff} and) column buckling curve “b” using A_g .

The second approach aimed at reducing conservatism in the European design resistance forecast involves replacing the curve “b” through the evaluation of two established curves in the European code, namely “a” and “a₀”. Figure 75(a) and (b) show the comparative results using EC3 design buckling curves “a” and “a₀”, respectively. Additionally, Table 16 presents the summarised quantitative analysis. Based on these results, it is possible to note that the evaluation of these two buckling curves yields the following observations:

- i) It can be noted in Figure 75(a) that more appropriate resistance forecasts are obtained when employing the buckling curve “a” in comparison to the predictions associated with the curve “b”, i.e., by decreasing the imperfection factor from 0.34 to 0.21. This conclusion is based on the quantitative analysis, revealing improved design accuracy. Specifically, the maximum ratio value decreased by 8% (1.59/1.47), and the new mean ratio of 1.16, coupled with a coefficient of variation (CoV) equal to 0.07, highlights a more consistent column design. Moreover, it is essential to highlight that all strengths forecasts are safe ($P_{u,FE}/P_{u,EC3} \geq 1$);
- ii) Nevertheless, in Figure 75(b), it is noteworthy that excessively diminishing the imperfection factor from 0.21 to 0.13, i.e., buckling curve “a₀”, results in an inevitable columns’ resistance deterioration. In 7% of the obtained results, the columns exhibited a ratio below 1 ($P_{u,FE}/P_{u,EC3} < 1$), reaching a minimum value of 0.97, showing that the predicted resistance exceeds the obtained resistance and leading to unsafe design;
- iii) Based on these two buckling curve evaluations (“a” and “a₀”), it is possible to note that an imperfection factor within the range of 0.13 to 0.21 is imperative for achieving more precise resistance predictions. However, the main aim of this study is to propose an alternative design that adheres to the well-defined guidelines outlined in the European code for consistency according to the current design rules;
- iv) Therefore, for a more consistent and less conservative resistance forecast in Eurocode 3: Part 1-4 [4] for austenitic and duplex stainless steel fixed-ended bolted starred columns susceptible to torsional buckling failure mode, two modifications are proposed: (iii₁) maintaining a cross-section class 3 for equal-leg angle regardless of b/t ratio, i.e., permanently $A = A_g$, and (iii₂) adopting the column buckling curve “a”. Consequently, it becomes feasible to characterise the actual torsional column behaviour, free from local buckling effects, by assuming a minor imperfection factor ($\alpha = 0.21$).

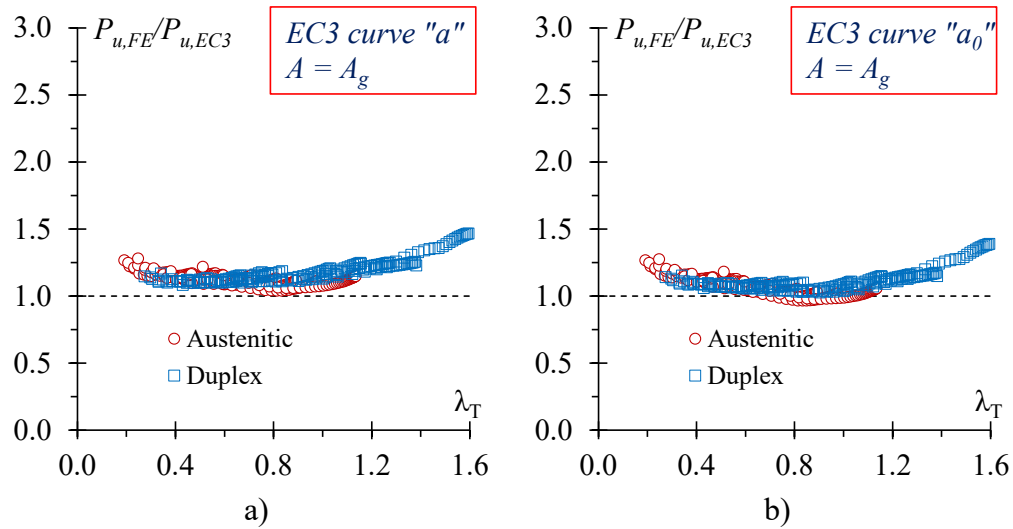


Figure 75: Bolted starred columns comparison of numerical results with Eurocode 3: Part 1.4 [4] a) column buckling curve “a” using A_g and) column buckling curve “a₀” using A_g .

Table 16: Bolted starred columns strengths comparison summary ($P_{u,FE}/P_{u,EC3}$).

	EC3 Curve “b” $A = A_g \text{ or } A_{eff}$	EC3 Curve “b” $A = A_g$	EC3 Curve “a” $A = A_g$	EC3 Curve “a ₀ ” $A = A_g$
<i>Maximum</i>	2.08	1.59	1.47	1.40
<i>Minimum</i>	1.12	1.12	1.04	0.97
<i>Mean</i>	1.39	1.25	1.16	1.09
<i>CoV</i>	0.20	0.09	0.07	0.08

8.4 Reliability analysis

This section presents a reliability analysis – following the standard procedure outlined in Annex D of EN 1990 [61] – to assess (i) the Eurocode 3: Part 1.4 [4] and (ii) the two proposed modifications to the existing EC3 design rules (specifically, employing curve “b” and curve “a₀” or “a” while consistently using cross-section gross area $A = A_g$) concerning welded and bolted starred columns made of (austenitic and duplex) stainless steel with fixed-ends susceptible to failure by torsional buckling.

The methodology of Annex D of EN 1990 [61] initiates with a comparison of theoretical resistance values ($r_{t,i}$), obtained either from the EC3 formulation or employing the two proposed design modifications, with the corresponding experimental/numerical results from each conducted test/simulation ($r_{e,i}$) to calculate the mean value correction factor (b). These

correlations between resistance values are graphically depicted in Figure 76 and Figure 77 for the resistance of austenitic and duplex stainless steel welded starred columns and in Figure 78 and Figure 79 for the resistance of austenitic and duplex stainless steel bolted starred columns.

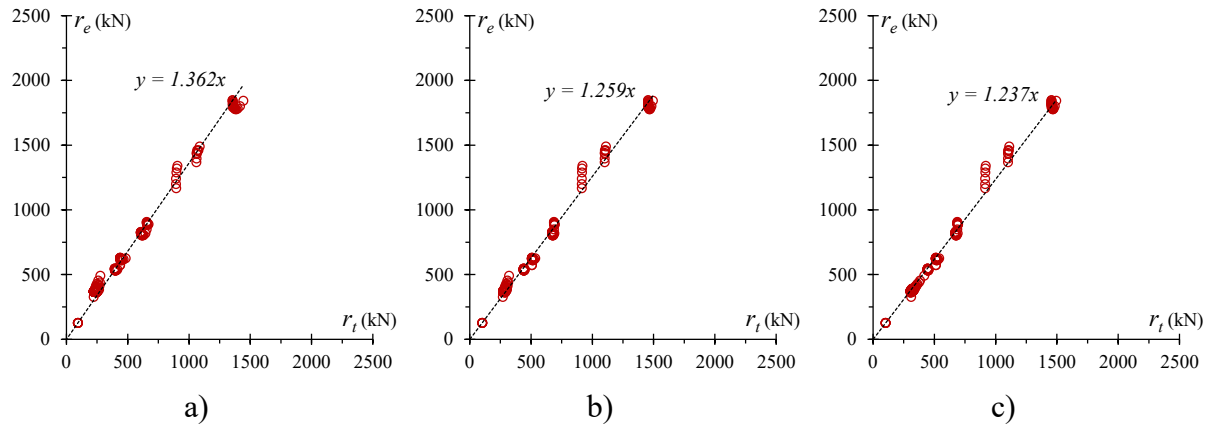


Figure 76: Austenitic stainless steel welded starred columns experimental/numerical (r_e) x theoretical (r_t) results plot a) EC3 approach curve "b", b) modified EC3 approach curve " a_0 " and c) modified EC3 approach curve " a_0 " using A_g .

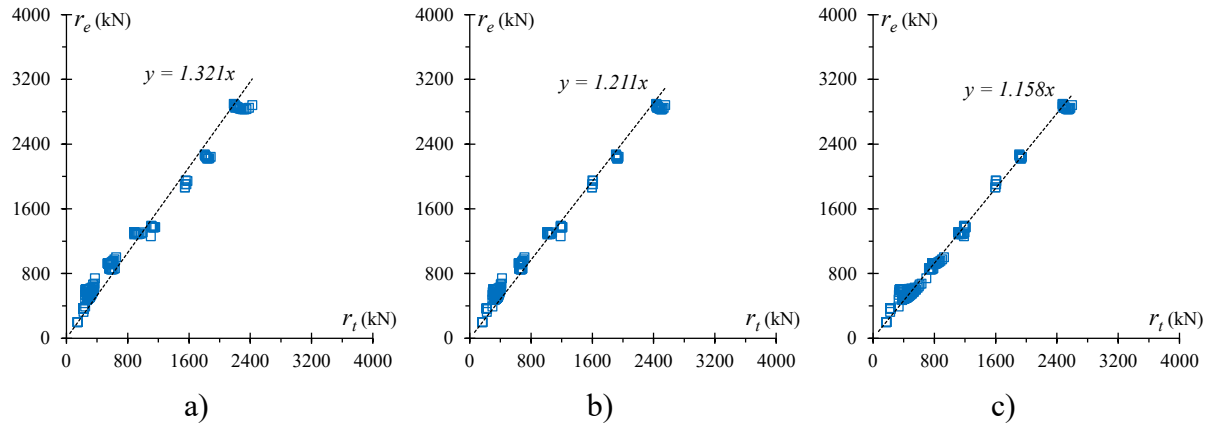


Figure 77: Duplex stainless steel welded starred columns experimental/numerical (r_e) x theoretical (r_t) results plot a) EC3 approach curve "b", b) modified EC3 approach curve " a_0 " and c) modified EC3 approach curve " a_0 " using A_g .

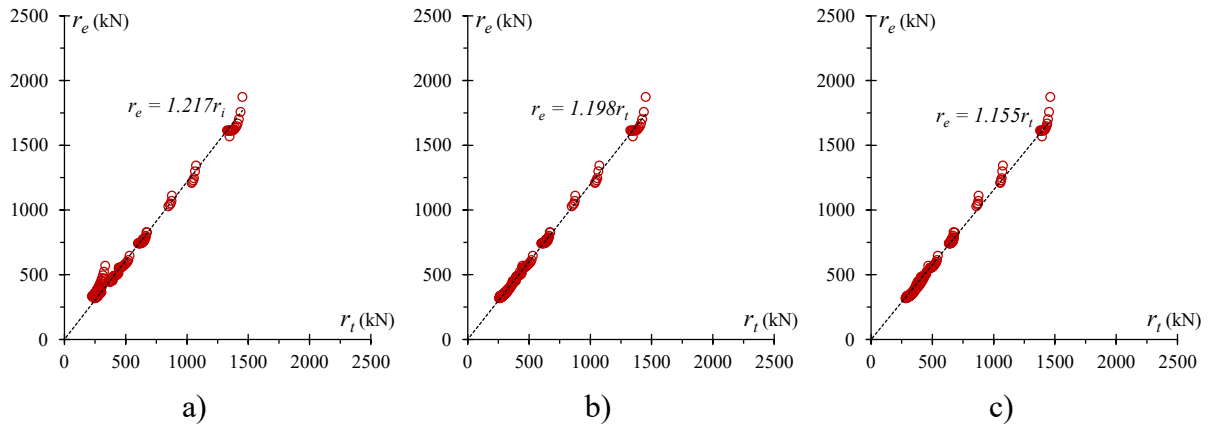


Figure 78: Austenitic stainless steel bolted starred columns experimental/numerical (r_e) x theoretical (r_t) results plot a) EC3 approach curve “b”, b) modified EC3 approach curve “b” using A_g and c) modified EC3 approach curve “a” using A_g .

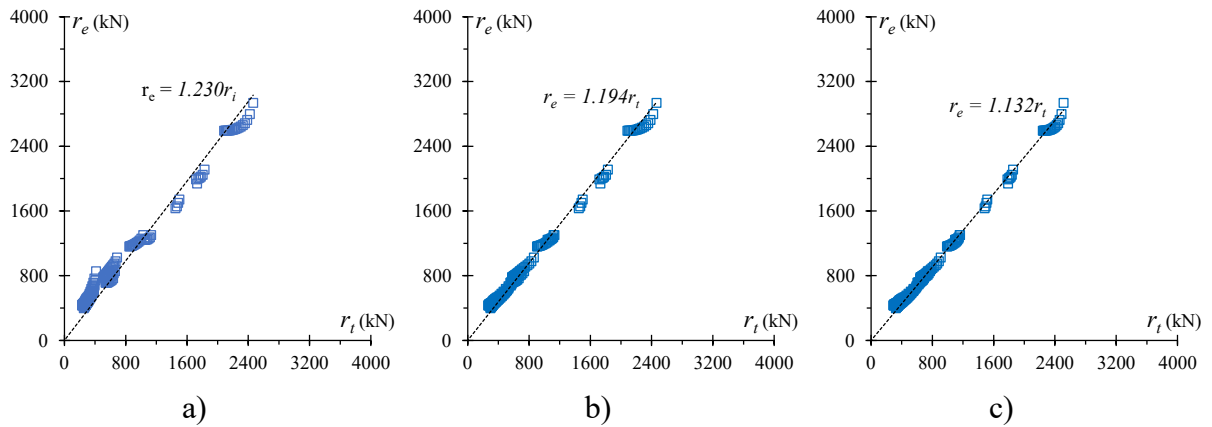


Figure 79: Duplex stainless steel bolted starred columns experimental/numerical (r_e) x theoretical (r_t) results plot a) EC3 approach curve “b”, b) modified EC3 approach curve “b” using A_g and c) modified EC3 approach curve “a” using A_g .

The next step is to calculate the error for each numerical result pair (determined from the expression $\delta_i = r_{e,i}/br_{t,i}$), showing the deviation of the numerical results. The coefficient of variation (CoV) of this error (V_δ) is used to measure the variabilities related to resistance function predictions, considering a normal probability distribution of δ_i , calculated from Eq. (60), where s_Δ^2 is the corresponding variance.

$$V_\delta = \sqrt{\exp(s_\Delta^2) - 1} \quad (60)$$

Moreover, the column buckling resistance function can be expressed in terms of Young's modulus (E), yield strength ($\sigma_{0.2\%}$), and the cross-section area (A). According to Afshan *et al.* [62], the different stainless steel types have an influence and must be accounted for in the reliability analysis. Therefore, following the procedures developed by the cited authors [62], the material over-strength parameter values ($f_{y,mean}/f_{y,nom}$), i.e., the ratio of mean to specified yield nominal strength, and the corresponding CoV of yield strength (V_{fy}) were adopted as 1.3 and 0.06 for austenitic, and 1.1 and 0.03 for duplex, respectively. The CoV of Young's modulus (V_E) was taken as 0.03 based on prior knowledge for both materials (austenitic and duplex) [62]. Regarding the cross-section geometry (area), a larger coefficient of variation parameter (V_A) value equal to 0.05 is more appropriate for stainless steel sections in the reliability analysis, as provided in [62]. These values of V_{fy} , V_E , and V_A are used to calculate the coefficient of variation parameter (V_{rt}) according to equation D.15b from Annex D of EN 1990 [61], presented in Eq. (61), i.e., including the effect of the variability of the basic variables in the resistance function.

$$V_{rt}^2 = \sum_{i=1}^j V_{Xi}^2 = (V_{fy}^2 + V_E^2 + V_A^2) \quad (61)$$

The design resistance value (r_d) can be obtained from equation D.21 in Annex D of EN 1990 [61], considering that the nominal strength in this study was taken as the mean strength from measured test data, reduced by the relevant over-strength factor, e.g., $f_{y,nom} = f_{y,mean}/(\text{over-strength factor})$ being the overstrength factor for each material. Finally, following the procedure presented in [62], the partial safety factor for torsional buckling resistances γ_{M1} can be assessed from Eq. (62), where $r_{n,i}$ is the nominal resistance based on EN 1993-1-4 [4] or EC3 approaches torsional buckling design equations and $r_{d,i}$ is the design resistance – mentioned before obtained from eq. D.21 from Annex D of EN 1990 [61] – both evaluated for each experimental/numerical result.

$$\gamma_{M1} = \frac{\sum_{i=1}^n r_{n,i}^2}{\sum_{i=1}^n r_{n,i} r_{d,i}} \quad (62)$$

A summary of the key results is reported in Table 17 and Table 18 for welded starred columns and bolted starred columns, respectively, and prompts the following comments:

- i) The statistical analysis results show that the obtained partial safety factor for the two proposed approaches is nearly equal to the current EC3 approach for both materials (austenitic and duplex);
- ii) The results for austenitic stainless steel fixed-ended welded starred columns suggest that all design resistance (EC3 curve “b”, EC3 curve “a₀” and EC3 curve “a₀” A_g) has a good agreement and fulfil the Eurocode reliability requirements, i.e., almost equal to 1. Concerning duplex stainless steel results, all the achieved partial factors (γ_{M1}) are greater than the austenitic results. However, the EC3 curve “a₀” A_g design approach presents a slight difference between the materials (only 5%), revealing an improvement in the member resistance for both materials;
- iii) For short-to-intermediate fixed-ended austenitic stainless steel bolted starred columns shows that the derived partial safety factors (γ_{M1}) obtained for the proposed approaches in this work (EC3 curve “a” using A_g) has a value slightly above the target value of approximately 1.1 as specified in EN 1993: Part 1-4 [4] for member buckling design, and is considered acceptable in the context of the analysis. Regarding duplex stainless steel column results, it is noteworthy that all attained partial factors surpass those obtained for austenitic stainless steel. Nevertheless, when adopting the EC3 curve “a” A_g design approach, a marginal distinction between the two stainless steel types is observed, amounting to a mere 9%;
- iv) Overall, it is feasible to conclude that the proposed alternative design approaches for short-to-intermediate fixed-ended austenitic stainless steel welded and bolted starred columns (susceptible to torsional buckling failure) exhibit clear advantages over the current EC3 standard rules. Both present a more consistent design with actual columns’ structural behaviour and reliable resistance forecast, i.e., consistently maintaining safety factors of approximately 1.1 for each type of stainless steel.

Table 17: Reliability analysis results assessed according to EN 1990 [61] for welded starred columns.

<i>Formulation</i>	<i>Grade</i>	<i>n</i>	$k_{d,n}$	<i>b</i>	V_{δ}	V_r	γ_{MI}
EC3 – curve “ <i>b</i> ”	Austenitic	272	3.121	1.362	0.088	0.122	1.077
	Duplex	272	3.121	1.321	0.167	0.179	1.248
EC3 – curve “ <i>a</i> ₀ ”	Austenitic	272	3.121	1.259	0.050	0.098	1.076
	Duplex	272	3.121	1.211	0.124	0.140	1.192
EC3 – curve “ <i>a</i> ₀ ” <i>A_g</i>	Austenitic	272	3.121	1.237	0.038	0.092	1.074
	Duplex	272	3.121	1.158	0.089	0.110	1.136

Table 18: Reliability analysis results assessed according to EN 1990 [61] for bolted starred columns.

<i>Formulation</i>	<i>Grade</i>	<i>n</i>	$k_{d,n}$	<i>b</i>	V_{δ}	V_r	γ_{MI}
EC3 – curve “ <i>b</i> ”	Austenitic	244	3.128	1.217	0.080	0.116	1.182
	Duplex	244	3.128	1.230	0.158	0.171	1.404
EC3 – curve “ <i>b</i> ” <i>A_g</i>	Austenitic	244	3.128	1.198	0.026	0.088	1.084
	Duplex	244	3.128	1.194	0.087	0.121	1.224
EC3 – curve “ <i>a</i> ” <i>A_g</i>	Austenitic	244	3.128	1.155	0.039	0.076	1.080
	Duplex	244	3.128	1.132	0.075	0.100	1.208

9 FINAL CONSIDERATIONS

A numerical investigation was conducted using ANSYS 17.0 [29] to assess the structural behaviour and evaluate the ultimate strength of fixed-ended short-to-intermediate welded and bolted starred austenitic and duplex stainless steel columns, i.e., prone to failure by torsional buckling. From the preliminary structural analysis, three essential notes deserve to be highlighted: the welded and bolted starred section assembly procedure guarantees adequate cross-section behaviour (i.e., shear centre and centroid are coincident); consequently, short-to-intermediate column lengths fail by pure torsional buckling; and the columns' torsional post-buckling equilibrium paths are stable as the column lengths approach to the transition length in the signature curve ($L \leq L_{TFS}$), i.e., with no minor-axis flexural buckling global interaction mode.

Based on the results obtained in the parametric analyses, which covered non-dimensional torsional slenderness (λ_T) ranging from 0.26 up to 1.56 for welded starred columns and from 0.19 up to 1.60 for bolted starred columns, it was possible to assess the provisions established for torsional buckling in Eurocode 3: Part 1.4 [4] – specifically column buckling curve “b”. Based on this comparison, the following main conclusions can be mentioned:

- i) Considering different material mechanical properties from austenitic and duplex, columns with equivalent non-dimensional torsional slenderness (λ_T) values share similar behaviour and ultimate strengths regardless of material type. This characteristic reveal that a unique column buckling curve can effectively forecast the ultimate failure load of fixed-ended welded or bolted starred columns susceptible to torsional buckling for both austenitic and duplex stainless steel materials. Therefore, there is no need to change the methodology already used by the European code;
- ii) The analysis of fixed-ended stainless steel welded starred columns using Eurocode 3: Part 1.4 [4] revealed inappropriate cross-section classifications and high conservatism in buckling curve “b,” with predictions up to 59% higher than the ultimate resistance. To improve the design of welded starred columns, two modifications to Eurocode 3: Part 1.4 [4] are proposed: avoiding the classification of cross-sections as class 4, as local buckling does not occur in short-to-intermediate columns, and changing the column buckling curve from

“*b*” to “*a₀*”, reducing the imperfection factor and leading to more accurate resistance predictions;

- iii) Similarly, the provisions of Eurocode 3: Part 1.4 [4] for bolted starred columns also showed overly conservative results, reducing some columns’ strength by up to 48% due to improper cross-section classification and a high imperfection factor in the buckling curve. It is proposed to consistently classify the cross-section as class 3 ($A = A_g$) and to change the column buckling curve from “*b*” to “*a*,” reducing the imperfection factor from 0.34 to 0.21 to achieve more reliable design predictions for bolted starred columns. This results in a less conservative and more reliable design approach for fixed-ended bolted starred austenitic and duplex stainless steel columns susceptible to torsional buckling;
- iv) Finally, for short-to-intermediate austenitic stainless steel bolted starred columns, the derived partial safety factors (γ_{MI}) using the proposed approaches (EC3 curve “*a*” using A_g) slightly exceeded the target value of approximately 1.1 (current value used in Eurocode 3 – Part 1.4 [4]). While duplex stainless steel columns showed higher partial factors than austenitic ones, adopting the EC3 curve “*a*” design approach resulted in only a marginal difference of about 9%. The proposed alternative design approaches provide more consistent designs with actual structural behaviour, maintaining reliable safety factors of approximately 1.1 for each type of stainless steel.

REFERENCES

- [1] Badoo, N. R., Stainless steel in construction: A review of research, applications, challenges and opportunities. *Journal of Constructional Steel Research* 2008, 64:1199–1206.
- [2] SCI, Steel Construction Institute, Design Manual for Structural Stainless Steel 2017, 4th Edition, Ascot: SCI.
- [3] Afshan, S., Gardner, L., The continuous strength method for structural stainless steel design. *Thin-Walled Structures* 2013, 68:42–49.
- [4] EUROCODE 3, EN 1993-1-4: 2006. Design of steel structures: Part 1-4: General rules – Supplementary rules for stainless steels. CEN, European Committee for Standardization, Brussels.
- [5] EUROCODE 3, EN 1993-1-1: 2005. Design of steel structures: Part 1-1: General rules and rules for buildings. CEN, European Committee for Standardization, Brussels.
- [6] <https://hbtengyang.en.made-in-china.com/>
- [7] <https://www.conbit.eu/cases/structural-reinforcement-high-voltage-pylons>
- [8] Wagner, H. 25th Anniversary Publication, Technical Hochschule, Danzig, Poland, 1929.
- [9] Timoshenko, S. P. History of the Strength of Materials, McGraw-Hill Book Co., Inc., New York, N.Y., 1953.
- [10] Timoshenko, S., & Gere, G. M. Theory of elastic stability, 1963
- [11] Gaylord, E. H., and Gaylord, C. N. Torsional buckling of compression members, *Design of Steel Structures* 1972, 2nd edition, McGraw-Hill Book Co., Inc., New York, pp. 237-243.

- [12] Rasmussen, Kim J. Design of Angle Columns with Locally Unstable Legs. *Journal of Structural Engineering (ASCE)* 2005, 131(10), 1553–1560.
- [13] Rasmussen, Kim J. Design of Slender Angle Section Beam-columns by the Direct Strength Method. *Journal of Structural Engineering (ASCE)* 2006, 132(2), 204–211.
- [14] Chodraui, G.M.B., Shifferaw, Y., Malite, M., Schafer, B.W. On the stability of cold-formed steel angles under compression. *REM - Revista da Escola de Minas (Ouro Preto, Brazil)* 2007;60(2):355–63 (in Portuguese).
- [15] Bulson PB. The stability of flat plates. London: Chatto & Windus; 1970.
- [16] Schardt, R. Verallgemeinerte technische biegetheorie. Berlin (German): Springer; 1989.
- [17] Schardt, R. Generalised beam theory – an adequate method for couple stability problems. *Thin-Walled Structures* 1994;19(2–4):161–80.
- [18] Vlasov, B.Z. Thin-walled elastic bars. Moscow: Fizmatgiz; 1959 [in Russian—English translation: Israel Program for Scientific Translation, Jerusalem, 1961].
- [19] Davies, J. M., Leach, P. Some applications of generalized beam theory. 11th Int. Speciality Conf., University of Missouri Rolla, 1992.
- [20] Davies, J.M., Leach, P. First-order generalised beam theory. *Journal Construction of Steel Research* 1994;31(2–3):187–220.
- [21] Davies, J.M., Leach, P., Heinz, D. Second-order generalised beam theory. *Journal Construction of Steel Research* 1994; 31(2–3):221–41
- [22] Leach, P. The calculation of modal cross-section properties for use in the generalized beam theory. *Thin-Walled Structures* 1994;19(1), 61–79.

- [23] Davies, J.M. Generalised beam theory (GBT) for coupled instability problems. In: Rondal J, editor. Coupled instability in metal structures: theoretical and design aspects, CISM course no 379. Vienna: Springer; 1998. p. 151–223.
- [24] Davies, J.M. Recent research advances in cold-formed steel structures. *Journal Construction of Steel Research* 2000;55(1–3):267–88.
- [25] Silvestre, N., Camotim D. First-order generalised beam theory for arbitrary orthotropic materials. *Thin Walled Structures* 2002; 40(9):755–89.
- [26] Silvestre, N., Camotim D. Second-order generalised beam theory for arbitrary orthotropic materials. *Thin Walled Structures* 2002; 40(9):791–820.
- [27] Camotim, D., Silvestre, N., Gonçalves, R., Dinis, P. B. GBT-based Structural Analysis of Thin-walled members: Overview, Recent Progress and Future Developments. *Solid Mechanics and Its Applications* 2006, 187–204.
- [28] Concalves, R., Ritto-Correa M., Camotim D. A new approach to the calculation of cross-section deformation modes in the framework of generalised beam theory. *Computational Mechanics* 2010;46(5):759–81.
- [29] Ansys, Inc. Theory Reference (version 17.0), 2017.
- [30] Dinis, P. B., Camotim D., Silvestre N. On the local and global buckling behaviour of angle, T-section and cruciform thin-walled members. *Thin-Walled Structures* 2010, 48(10–11), 786–7
- [31] Dinis, P. B., Camotim, D., Silvestre, N. On the mechanics of thin-walled angle column instability. *Thin-Walled Structures* 2012, 52, 80–89.
- [32] Bebiano, R., Silvestre N., Camotim D. GBTUL 1.0b – code for buckling and vibration analysis of thin-walled members, 2008. Freely available at <http://www.civil.ist.utl.pt/gbt>
- [33] Simulia Inc., Abaqus Standard (vrs.6.7-5); 2008.

- [34] Dinis, P. B., Camotim, D., Silvestre, N. Buckling, post-buckling, strength and design of angle columns. Proc., USB Key Drive Structural Stability Research Council Annual Stability Conf., Structural Stability Research Council 2012, Rolla, MO.
- [35] Dinis, P. B., Camotim, D., Vieira L. DSM design approach for hot-rolled steel angle columns *ce/papers*, 1, 2017 2–3. (3781–90).
- [36] Dinis, P. B., Camotim, D. Buckling, post-buckling and strength of cruciform columns, in: Structural Stability Research Council Annual Stability Conference (SSRC), 2011, pp. 271–283.
- [37] Silvestre, N., Dinis, P.B., Camotim, D. Developments on the design of cold-formed steel angles, *J. Struct. Eng.* 139 (5) (2012) 680–694 ASCE.
- [38] Dinis, P.B., Camotim, D. A novel DSM-based approach for the rational design of fixed-ended and pin-ended short-to-intermediate thin-walled angle columns, *Thin-Walled Structures* 2015, 87, 158–182.
- [39] Schafer, BW. Review: the direct strength method of cold-formed steel member design. *Journal Construction Steel Research* 2008, 64(7-8):766–78.
- [40] Sirqueira, A., Vellasco, P., Lima, L., Sarquis, F., da Silva, A. Experimental and numerical assessments of hot-rolled carbon steel fixed-ended angles in compression. *Journal of Constructional Steel Research* 2020, 169-106069.
- [41] Reynolds, N. A. (2013). Behavior and Design of Concentrically Loaded Duplex Stainless Steel Single Equal-Leg Angle Struts. (August), 253.
- [42] Menezes, A., Vellasco, P., Lima, L., da Silva, A. Experimental and numerical investigation of austenitic stainless steel hot-rolled angles under compression. *Journal of Constructional Steel Research* 2018; 149:1–15.

- [43] Liang, Y., Jeyapragasam, V. V. K., Zhang L., Zhao O. Flexural torsional buckling behaviour of fixed-ended hot-rolled austenitic stainless steel equal-leg angle section columns. *Journal of Constructional Steel Research* 2018, 154, 43–54.
- [44] Sirqueira, A., Vellasco, P., Lima, L., Sarquis, F. Experimental assessment of stainless steel hot-rolled equal legs angles in compression. *Journal of Constructional Steel Research* 2020, 169-106069.
- [45] Sarquis, F., Lima, L., Vellasco, P., Rodrigues, M. Experimental and numerical investigation of hot-rolled stainless steel equal leg angles under compression. *Thin-Walled Structures* 2020, 151:106742.
- [46] Dobrić, J., Filipović, A., Marković Z., Baddoo, N. Structural response to axial testing of cold-formed stainless steel angle columns. *Thin-Walled Structures* 2020, 156:106986
- [47] Filipović, A., Dobrić, J., Baddoo, N., Može, P. Experimental response of hot-rolled stainless steel angle columns. *Thin-Walled Structures* 2021, 163:107659.
- [48] Filipović, A., Dobrić, J., Budevaca, D., Fric, N., Baddoo, N., Experimental study of laser-welded stainless steel angle columns. *Thin-Walled Structures* 2021, 164:107777.
- [49] Dobrić, J., Filipović, A., Baddoo N., Marković, Z., Budevaca, D., Design procedures for cold-formed stainless steel equal-leg angle columns. *Thin-Walled Structures* 2021, 159:107210.
- [50] Botelho, I., Kayser, A., Sarquis, F., Lima, L., Vellasco, P., Silva, A., Rodrigues, M., Diniz, M., Starred rolled stainless steel angle sections under compression: An experimental and numerical investigation. *Thin-Walled Structures* 2020, 158:107177.
- [51] EUROCODE 3, EN 1993-1-5: 2006. Design of steel structures: Part 1-5: General rules – plated structural elements. CEN, European Committee for Standardization, Brussels.
- [52] Winter, G., (1947). Strength of thin steel plates compression flanges. *Transactions of the American Society of Civil Engineers*, 112(1):527–554.

- [53] Stinfesco, D., (1970). Experimental basis for European column curves. *Construction Métallique*, vol. 7. no. 3, p. 5-12 (in French).
- [54] Jacquet, J., (1970). Column buckling tests and their statistical evaluation. *Construction Métallique*, vol. 7. no. 3 (in French).
- [55] Beer, H., Schulz, G. (1970). Theoretical basis for European column curves. *Construction Métallique*, vol. 7. no. 3, p. 35-57 (in French).
- [56] Rondal, J. e Maquoi, R. (1979). Airton-Perry formulation for metallic members buckling. *Construction Métallique*, no. 4, p. 41-53 (in French).
- [57] Schafer B. W. and Pekoz T. (1996), Geometrical Imperfections and Residual Stresses for Use in the Analytical Modeling of Cold-formed Steel Members, CCFSS Proceedings of International Specialty Conference on Cold-Formed Steel Structures (1971 - 2018). 4.
- [58] Stainless Steel Equal Leg Angle - A304 Catalogue - Elinox (2019) <https://www.elinox.com.br/produtos/cantoneiras/>. Last Access: 20/02/2024.
- [59] N. Trahair, Strength design of cruciform steel columns, *Engineering Structures*, vol. 35, pp. 307–313, 2011.
- [60] Može, Primož; Cajot, Luis-Guy; Sinur, Franc; Rejec, Klemen; Beg, Darko (2014). Residual stress distribution of large steel equal leg angles. *Engineering Structures*, 71(), 35–47.
- [61] EN. Eurocode – Basis of structural design. Brussels: European Committee for 583 Standardisation (CEN); 1990. p. 2002.
- [62] Afshan S, Francis P, Baddoo NR, Gardner L. Reliability analysis of structural stainless steel design provisions. *Journal of Constructional Steel Research*, 2015, 114:293–304.

APPENDIX A

This appendix aims to investigate and obtain the welded starred section properties using ANSYS software [29] based on finite beam elements. It is known that if the cross-section consists of thin elements which cross at a common point and if the rotation axis is assumed to pass through the shear centre, there is no primary warping constant ($I_w = 0$). However, the warping cross-section resistance comes exclusively from the secondary warping constant ($I_{ws} \neq 0$) – based on a secondary distribution of normal stress.

Therefore, the secondary warping constant (I_{ws}) is one of the crucial section properties for the torsional buckling behaviour of structural members. Initially, a usual plain cruciform cross-section illustrated in Figure A.1(a) – created through symmetrical rectangular plates – was used to validate the approach, i.e., acquire numerical results of an already learned section. According to the classical torsion theory, it is well-known that the rectangular cross-section secondary warping constant is given by $h^3t^3/144$. Likewise, the plain cruciform section secondary warping constant ($I_{ws,cru}$) is calculated using the warping stiffness sum of two rectangular sections – replacing the width h for $2b$ – according to Eq. (A.1). Additionally, the plain cruciform torsion constant ($I_{T,cru}$) is assessed by Eq. (A.2)

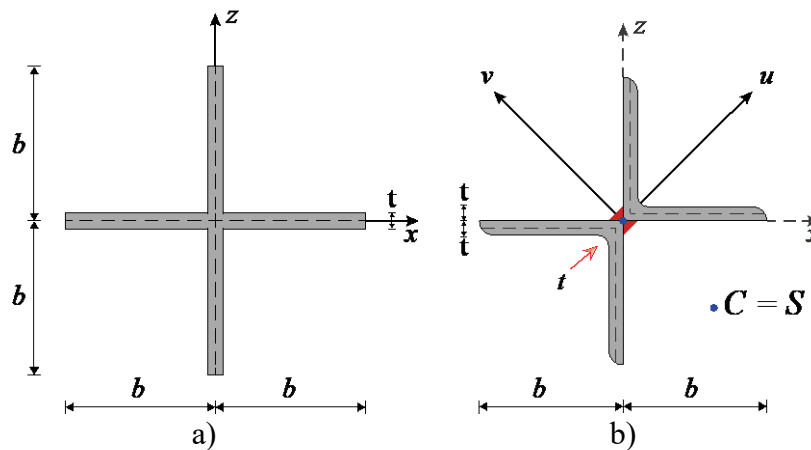


Figure A.1: a) Symmetrical plain cruciform cross-section and b) dual equal-leg angle welded cross-section.

$$I_{ws,cru} = \frac{b^3t^3}{9} \quad (A.1)$$

$$I_{T,cru} = \frac{4bt^3}{3} \quad (A.2)$$

The strategy to acquire the welded sections' properties – Figure A.1(b) – in Ansys software consists of the following steps: (i) create the cross-section geometry; (ii) generate areas enclosed by previously established lines; (iii) define a custom section using the command *SECWRITE* to create a file (“*.sect*”) containing user mesh section information through defined areas; (iv) hereafter, the *SECTYPE* command is employed to associate a beam section; (v) when the cross-section (mesh) is established, the software creates a numerical model using a nine-node cell on the areas to calculate the section properties; (vi) finally, the *SECREAD* command is used to obtain the section properties.

Figure A.2(a) shows a plot with a better-detailed view of the plain cruciform section properties assembled by rectangular plates with $b = 63.50$ mm and $t = 4.76$ mm, specifically the (secondary) warping constant and torsion constant – highlighted in red. Table A.1 compares quantitatively the values obtained from Ansys ($I_{ws,cruA}$ and $I_{T,cruA}$) and calculated according to Eqs. (A.1) and (A.2) for three distinct dimensions cruciform sections. These results show: (i) excellent accuracy – approximately 100% – when plain cruciform numerical section properties are compared to the results from classical torsion theory, (ii) revealing an ideal approach to calculate the welded starred section properties.

Similarly, Figure A.2(b) displays the plot of the welded starred section properties assembled by two equal-leg angles L63.5×4.76 mm with a fillet weld leg length equal to the thickness ($t = 4.76$ mm). The (secondary) warping ($I_{ws,sta}$) and torsion ($I_{T,sta}$) constants are also highlighted in red. Table A.2 compares the numerical properties of the welded starred and cruciform sections. The observation of this comparison leads to the following comments:

- i) The welded starred torsion constant ($I_{T,sta}$) presents a slight difference of only 8% when compared to the cruciform section ($I_{T,cru}$), revealing a good correlation;
- ii) However, the welded starred secondary warping ($I_{ws,sta}$) is about four times greater than the cruciform section ($I_{ws,cru}$). This value can be explained by the warping stiffness of the equal-leg angles that build the section – rounded corner neglected;
- iii) This difference in the welded starred secondary warping constant shows a significant improvement in warping resistance, i.e., despite the exact

dimensions, plain cruciform sections are more flexible in torsion than welded starred;

- iv) Therefore, to facilitate the design of structural elements with welded starred sections, a parametric study will be carried out in section 5.4, aiming for a simple manner of calculating this section's secondary warping constant (I_{ws}) and torsion constant (I_T).

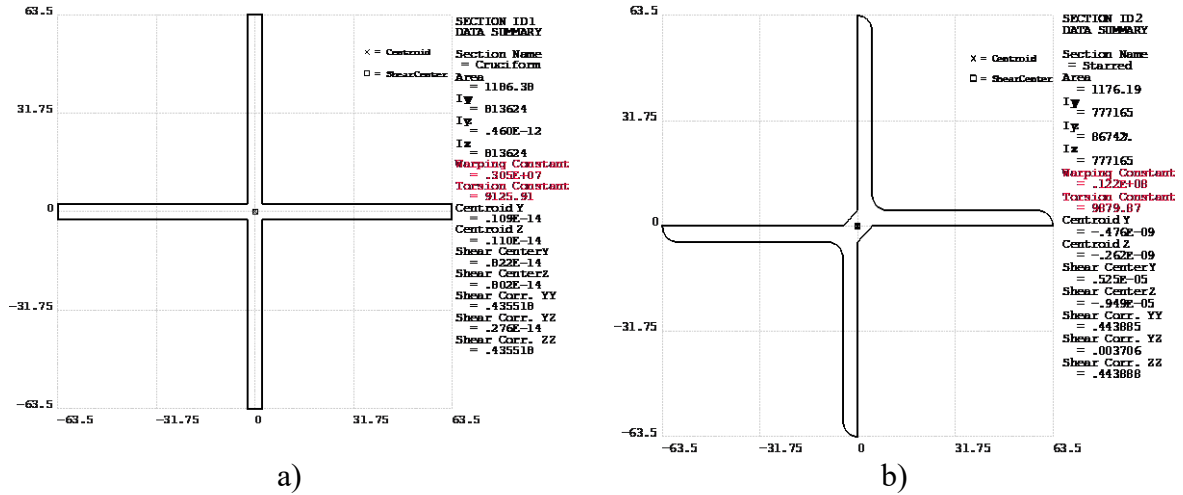


Figure A.2: Plot of a) plain cruciform and b) welded starred cross-sections in Ansys [29].

Table A.1: Secondary warping and torsion constant comparative numerical results ($I_{ws,cruA}$ and $I_{T,cruA}$) and equations provided ($I_{ws,cru}$ and $I_{T,cru}$) for the cruciform cross-section properties.

Rectangular		Ansys Results		Eqs. (A.1) and (A.2)		$\frac{I_{ws,cruA}}{I_{ws,cru}}$	$\frac{I_{T,cruA}}{I_{T,cru}}$
b	t	$I_{ws,cruA}$	$I_{T,cruA}$	$I_{ws,cru}$	$I_{T,cru}$		
(mm)	(mm)	(mm ⁶)	(mm ⁴)	(mm ⁶)	(mm ⁴)		
63.50	4.76	3047681.24	9125.91	3068312.04	9131.31	0.99	1.00
63.50	6.35	7196657.61	21553.88	7284501.58	21678.72	0.99	0.99
76.20	4.76	5277140.42	10920.34	5302043.21	10957.57	1.00	1.00

Table A.2: Secondary warping and torsion constant comparison welded starred and plain cruciform cross-sections.

Welded Starred Section		Cruciform Section		$\frac{I_{ws,sta}}{I_{ws,cru}}$	$\frac{I_{T,sta}}{I_{T,cru}}$
b	t	$I_{ws,sta}$	$I_{T,sta}$		
(mm)	(mm)	(mm ⁶)	(mm ⁴)		
63.50	4.76	12178563.20	9879.86	3.96	1.08